A METHOD FOR AIRCRAFT AFTERBURNER COMBUSTION WITHOUT FLAMEHOLDERS

A Dissertation
Presented to
The Academic Faculty

By

Shai Birmaher

In Partial Fulfillment
of the Requirements for the Degree
Doctor of Philosophy in Aerospace Engineering

Georgia Institute of Technology

May 2009

A METHOD FOR AIRCRAFT AFTERBURNER COMBUSTION WITHOUT FLAMEHOLDERS

Approved by:

Dr. Ben T. Zinn, Advisor
School of Aerospace Engineering
Georgia Institute of Technology

Dr. Rick Gaeta
School of Aerospace Engineering
Georgia Institute of Technology

Dr. Yedidia Neumeier
School of Aerospace Engineering
Georgia Institute of Technology

Dr. Jeff Jagoda
School of Aerospace Engineering
Georgia Institute of Technology

Dr. Thomas Fuller
School of Chemical and Biomolecular Engineering
Georgia Institute of Technology

Date Approved: February 27, 2009

ACKNOWLEDGEMENTS

I would like to first thank my advisor, Dr. Ben Zinn, for his valuable guidance and support throughout the course of this work. I wish to thank Dr. Yedidia Neumeier. This research would not have been possible without Yedidia, whose innovation and sense of humor enriched my experience at Georgia Tech. I would also like to thank the other members of my committee, Dr. Jeff Jagoda, Dr. Rick Gaeta, and Dr. Thomas Fuller, for their input and interest in this research.

I would like to thank the research engineers and Georgia Tech staff who contributed to this work. Thanks to Sasha Bibik and Dimitriy Shcherbik for their technical expertise and willingness to help at a moment's notice. Also, thanks to Scott Moseley and Scott Elliott for their friendly and skillful support at the machine shop.

I wish to thank all the graduate students at the Ben Zinn Combustion Lab for their help and encouragement. In particular, I would like to thank Philipp Zeller, who started this research effort and set a high standard for efficiency and dedication. Also, I would like to thank Petter Wirfalt, who provided valuable assistance and great company.

I am grateful to my family and friends for their encouragement throughout my graduate career. Above all, I am grateful to my fiancée, Claire, for her constant love, support and patience.

TABLE OF CONTENTS

LIST OF TABLES

LIST OF FIGURES

NOMENCLATURE

B_M	Spalding mass transfer number, [nondimensional] see Equation (4.6)
B_T	Spalding heat transfer number, [nondimensional] see Equation (4.16) to Equation (4.19)
C_{drag}	Droplet drag coefficient, [nondimensional] see Equation (4.12)
c_f	Liquid fuel specific heat [J/kg-K]
$\overline{c}_{p,F}$	Fuel vapor specific heat evaluated at $\overline{T}$ [J/kg-K]
d_{drop}	Droplet diameter [m or μm where specified]
D_M	Fuel-vapor/air binary mass diffusivity [m^2/s]
F_M	Correction factor, [nondimensional] see Equation (4.8)
F_T	Correction factor, [nondimensional] see Equation (4.19)
I	Chemical reaction progress variable [non-dimensional] or axial radiation intensity [a.u.] as specified
$\overline{k}$	Gas thermal conductivity evaluated at $\overline{T}$ [W/m-K]
L_{comb}	Combustion zone length [cm]
LHV	Lower heating value [MJ/kg or MJ/kmol where specified]
$\dot{m}$	Mass flow rate [kg/s or g/s where specified]
$\dot{m}_{air}$	Bulk air flow rate [kg/s or g/s where specified]
$\dot{m}_{drop}$	Droplet evaporation rate [kg/s]
$\dot{m}_{JetA}$	Jet-A flow rate [kg/s or g/s where specified]
MW	Molecular weight [g/mol]

Nu	Nusselt number [nondimensional]
Nu^*	Modified Nusselt number [nondimensional]
P	Pressure [Pa or psia where specified]
$P_{F,s}$	Fuel vapor saturated pressure [Pa]
$\overline{\Pr}$	Prandtl number defined using average 'film' properties, $\overline{\mu}\,\overline{c}_p \big/ \overline{k}$
PR_G	Global power ratio, [nondimensional] see Equation (7.3)
$PR_{G,H2}$	Global power ratio based on trigger gas H_2 content, [nondimensional] see Equation (7.4)
PR_L	Local power ratio, [nondimensional]
$\dot{Q}_l$	Heat transfer to the fuel droplet [J/s]
R	Universal gas constant, 8.314 J/mol-K
Re_{drag}	Reynolds number, see Equation (4.10)
$\overline{Sc}$	Schmidt number defined using average 'film' properties, $\overline{\mu} \big/ \overline{\rho}\overline{D}_M$ [nondimensional]
Sh	Sherwood number, [nondimensional]
Sh^*	Modified Sherwood number, [nondimensional]
SK	'Skewness' of the axial chemiluminescence intensity profile, [nondimensional], see Equation (8.4)
SMD	Airblast atomizer spray sauter mean diameter [m or μm where specified]
STD	'Standard deviation' of the axial chemiluminescence intensity profile [cm], see Equation (8.3)
T	Temperature [K]
$T_{\Delta m_i}$	Temperature of the fuel element created in the i^{th} time interval [K]
T_{boil}	Boiling temperature [K]

T_{SS}	Droplet steady-state temperature [K]
T_{tot}	Bulk flow total (stagnation) temperature [K]
t	time [sec or msec where specified]
t_{ign}	Ignition delay time [sec] defined as the time to maximum temperature gradient (or temperature inflection point)
$t_{ign,n.t.}$	Ignition delay time of fuel/oxidizer without addition of trigger gas [sec or msec as specified]
$t_{ign,trigger}$	Ignition delay time of trigger-gas/oxidizer [sec or msec as specified]
t^*	Normalized time, t/t_{ign} [nondimensional]
t^*_{nt}	Normalized time with respect to the no trigger ignition delay time, $t/t_{ign,n.t.}$ [nondimensional]
$t^*_{\Delta t,n.t.}$	$t_{ign,trigger}$ divided the difference between $t_{ign,n.t.}$ and the time at which trigger gas is added to the mixture, [nondimensional] see Equation (7.7)
u	Velocity [m/s]
u'	r.m.s turbulent velocity fluctuations –estimated as 5% of the local bulk flow velocity [m/sec]
$u_{air,inj}$	Discharge velocity of airblast atomizer air [m/sec]
u_{drop}	Droplet velocity [m/sec]
V_{drop}	Droplet volume [m^3]
x	Distance [m or cm where specified]
$X_{5\%}$	Location of 5% cumulative axial chemiluminescence intensity [cm]
$X_{95\%}$	Location of 95% cumulative axial chemiluminescence intensity [cm]
x_{inj}	Location of Jet-A injection [m or cm where specified]

X_M	'Mean location' of the axial chemiluminescence intensity [cm], see Equation (8.2)
X_{MAX}	Location of maximum axial chemiluminescence intensity [cm]
Y	Mass fraction, [nondimensional]
$Y_{F,bulk}$	Bulk flow fuel mass fraction, [nondimensional]
$Y_{F,s}$	Fuel mass fraction at the droplet surface, [nondimensional]

Greek Symbols

Δh_{vap}	Fuel heat of vaporization [J/kg]
Δm_i	Mass evaporated from fuel droplets in the i^{th} time increment. Also used as a symbol for the i^{th} fuel element.
$[\Delta T]^*_{n.t.}$	Scaled temperature increase – the temperature increase from combustion scaled by the temperature increase from complete combustion with no trigger, [nondimensional] see Equation (7.8)
ΔT_{TS}	Temperature drop across the TS [K]
Δt	Time increment [sec or msec as specified]
$[\Delta t]^*_{n.t.}$	Normalized amount of time left until autoignition - time from the addition of trigger gas to the ignition delay of the mixture divided by the time from the addition of trigger gas to the ignition delay with no trigger, [nondimensional] see Equation (7.6)
ϕ	Equivalence ratio, [nondimensional]
ϕ_1	Equivalence ratio of methane/air combustion in the PAC, [nondimensional]
ϕ_2	Equivalence ratio of propane/vitiated-air combustion in the PAC, [nondimensional]

$\phi_{[CO2]}$	Estimated equivalence ratio based on the measured CO_2 composition, [nondimensional]
$\phi_{[O2]}$	Estimated equivalence ratio based on the measured O_2 composition, [nondimensional]
μ	Viscosity [Pa-s]
μ_1	Statistical mean
ρ	Density [kg/m^3]
σ	Statistical standard deviation
σ_f	Fuel surface tension [N/m]
τ_{ign}	Chemical ignition delay of pre-mixed, pre-vaporized fuel/oxidizer based on experimental measurements at constant temperature and pressure, [sec or msec as specified]
χ	Mole fraction, [nondimensional]
$\chi_{F,bulk}$	Bulk flow fuel mole fraction, [nondimensional]
$\chi_{F,s}$	Fuel mole fraction at droplet surface, [nondimensional]

Subscripts

(ϕ)	The products of methane/air combustion at the equivalence ratio given within the parenthesis, e.g. (3.325) refers to methane/air combustion at $\phi = 3.325$
aft	Afterburner section of the AF
boil	Boiling point
bulk	Bulk flow
drop	Fuel droplet

dry	Excludes water vapor
F	Fuel vapor
f	Liquid fuel
final	Final (equilibrium) value
G	Global value
i	Denotes i^{th} time interval in the vaporization model; also, denotes a property of the i^{th} fuel in a mixture with several different fuels
initial	Initial value
inj	Pertaining to Jet-A airblast atomizer
n.t.	Denotes a case with no trigger; or, when accompanied by a * superscript, denotes a variable that is scaled by a quantity for a no trigger case
PL	Plenum
s	Droplet surface
SS	Steady-state
surr. fuel	Surrogate fuel
trigger	Trigger gas property
vit	Vitiation (pre-combustion) properties
wet	Includes water vapor

Superscripts and Overscore

–	Average (reference) value calculated using the average temperature and average composition, defined in Equation (4.4) and Equation (4.5)
*	Denotes a modified value in the evaporation sub-model; or, in all other contexts, denotes a scaled quantity

Abbreviations

AF	Afterburner Facility
CHBR	Closed Homogeneous Batch Reactor
PAC	Propane Autoignition Combustor
PAT	Prime and Trigger
POx	Partial Oxidation
TS	Turbine Simulator

SUMMARY

State of the art aircraft afterburners employ spray bars to inject fuel and flameholders to stabilize the combustion process. Such afterburner designs significantly increase the length (and thus weight), pressure losses, and observability of the engine. This thesis presents a feasibility study of a compact 'prime and trigger' (PAT) afterburner concept that eliminates the fuel spray bars and flameholders and, thus, eliminates the above-mentioned problems. In this concept, afterburner fuel is injected just upstream or in between the turbine stages. As the fuel travels through the turbine stages, it evaporates, mixes with the bulk flow, and undergoes some chemical reactions without any significant heat release, a process referred to as 'priming'. Downstream of the turbine stages, combustion could take place through autoignition. However, if fuel autoignition does not occur or if autoignition does not produce a combustion zone that is stable and highly efficient, then a low power pilot, or 'trigger', can be used to control the combustion process.

The envisioned trigger for the PAT concept is a jet of product gas from ultra-rich hydrocarbon/air combustion that is injected through the afterburner liner. The ultra-rich combustion process, referred to as partial oxidation (POx), can convert a hydrocarbon fuel, such as kerosene, to H_2, CO, CH_4, N_2, CO_2, H_2O, and smaller quantities of radicals and other light hydrocarbon molecules – a mixture referred to as POx gas. When injected into the high temperature afterburner flow, the POx gas, especially its H_2 component, rapidly produces radicals and heat that accelerate the autoignition of the primed mixture

and, thus, provide an anchor point for the afterburner combustion process. Conceptually, the POx gas would be generated by a small, onboard, auxiliary combustor that draws a small amount of core air flow and burns the same fuel as the main combustor.

The objective of this research was to demonstrate the feasibility of the PAT afterburner concept. This was accomplished through parallel experimental, theoretical and numerical efforts that showed that (1) combustion of fuel injected within or upstream of turbine stages can occur only downstream of the turbine stages, and (2) the combustion zone is compact, stable and efficient.

Two experimental facilities were developed under this program. The first facility is a model of the envisioned PAT concept in a turbojet engine with an afterburner, termed the Afterburner Facility (AF). The AF simulates the O_2 content and bulk flow profiles of the temperature and velocity through a turbojet combustor, turbine stage and afterburner. The prime stage was simulated by injecting liquid Jet-A into the AF at locations upstream of the section that models the turbine stage, termed the turbine simulator (TS). The trigger stage was simulated by a jet of H_2 injected normal to the flow just downstream of the TS. H_2 was used instead of POx gas, because a POx reactor was not available. The second facility, termed the Propane Autoignition Combustor (PAC), is a two-stage combustor that burns methane/air to generate vitiated-air and then mixes propane vapor with the vitiated-air for measurements of propane autoignition. As in the AF, H_2 can be injected to trigger the autoignition process. The PAC was used to study the effect of a H_2 trigger on autoignition without the influence of evaporation and variable bulk flow profiles, which are present in the AF. In addition, some of the PAC measurements

techniques were more detailed than in the AF and were thus used to help interpret the AF results.

A theoretical model of fuel priming and autoignition was developed to support the AF experiments. It was also used to study the feasibility of the PAT concept at pressures outside the AF operating range. The developed model simulated the physics of fuel priming and autoignition in the AF. Specifically, it estimated the bulk flow profiles of temperature, pressure and velocity along the facility and then used them to simulate the afterburner fuel transport, evaporation, mixing and chemistry. The model outputs included axial profiles of fuel droplet diameter and temperature, profiles of chemical progress variables, and the predicted autoignition location in the AF.

The numerical efforts consisted of Chemkin simulations of high temperature Jet-A/vitiated-air autoignition with the addition of H_2 and POx triggers. The purpose of the Chemkin study was to examine the effect of several POx gas compositions on the Jet-A/vitiated-air autoignition process; to compare the POx and H_2 triggers; and to explore several reasons for why POx gas and H_2 are suitable trigger mechanisms. Notably, it was the only available method in this research for studying the effect of the POx trigger. The Chemkin simulations were performed for varying quantities of each trigger gas, for varying Jet-A/vitiated-air equivalence ratios, and for two different vitiated-air compositions.

The experimental, theoretical, and numerical results obtained in this investigation indicated that the PAT concept provides a feasible approach to afterburner combustion. The experiments in the AF showed that the ignition delay of Jet-A is sufficiently long to allow fuel injection within turbine stages without significant heat release upstream of the

afterburner. In the AF experiments without the H_2 trigger, Jet-A combustion was achieved through autoignition; however, the autoignition combustion zone exhibited large axial fluctuations and low combustion efficiency. The H_2 trigger was able to shift the combustion zone upstream, make it more compact, reduce fluctuations in its axial position, and raise the combustion efficiency to nearly 100%. The PAC experiments also showed that a H_2 trigger can shift the combustion zone upstream, make it more compact, and increase the combustion efficiency. The PAC results were obtained with lower O_2 content and higher equivalence ratios than in the AF. Therefore, the combined AF and PAC results suggested that the PAT concept is feasible over a wide range of operating conditions. The developed model showed good agreement with the AF results. It also predicted that the PAT concept is feasible at realistic turbine engine pressures above the AF operating range. However, the model predicted that the large, rapid pressure drop across a turbine stage could cause fuel droplets passing through it to flash-boil, which would significantly reduce the overall ignition delay. Thus, flash-boiling must be considered as it could lead to unwanted heat release within the turbine stages. Finally, the Chemkin results predicted that H_2 and POx gas triggers can both significantly reduce the ignition delay time of primed Jet-A/vitiated air mixtures. The results showed that certain POx gas compositions can produce the same reduction in ignition delay time as H_2 when added at slightly higher amounts. This suggests that POx gas is a suitable trigger mechanism for the PAT concept.

INTRODUCTION

1.1 Background and Motivation

The aircraft engine afterburner is an extension to a turbine engine that provides the additional thrust needed for take-off from short runways, rapid acceleration, and supersonic flight. The afterburner increases thrust by burning additional fuel in the turbine exhaust stream. Figure 1 shows a basic schematic of a turbojet with an afterburner. In theory, the design is simple: attach a long duct downstream of the turbine stages; within the duct, add fuel spray bars and a bluff body flameholder to anchor the combustion process; and then expand the afterburner combustion products through a nozzle. In practice, however, afterburner operation is complex and challenging. Issues ranging from material constraints to combustion dynamics must be addressed in order to produce a working afterburner.

The image of the NK32-TU160 afterburner in Figure 2 shows the scale and complexity of the afterburner design. The image is taken from the afterburner outlet looking into the engine, thus the structure in the forefront of the image is the variable area exhaust nozzle. The structure far upstream and centered in the duct is the aft cone of the

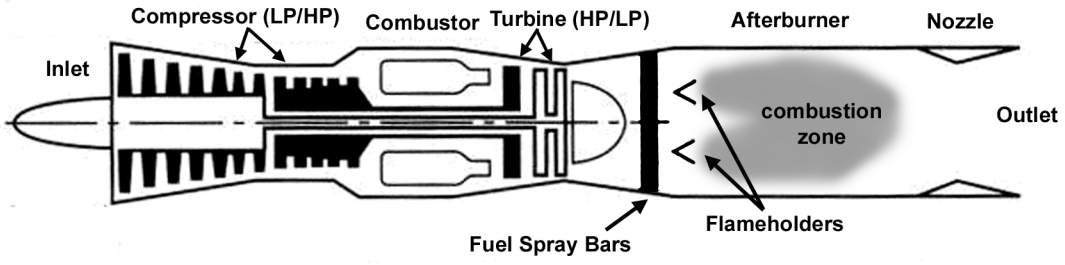

Figure 1. Schematic of a dual-spool turbojet afterburner based on an image taken from [1]

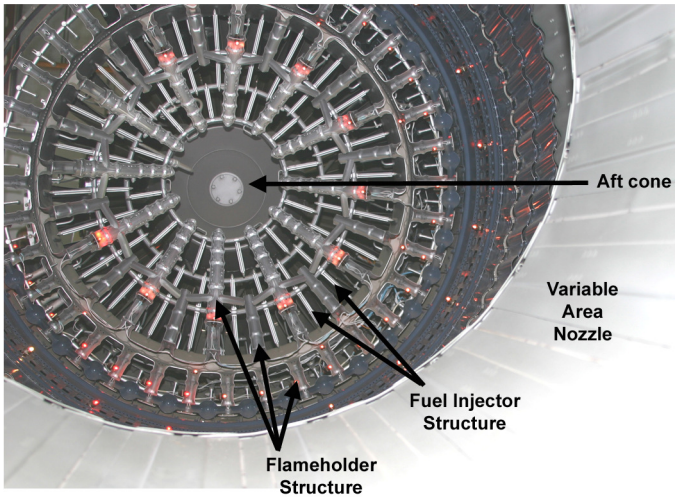

Figure 2. The afterburner of an NK32-TU160 engine.

turbine spool. The complex flameholder structure surrounds the aft cone. It is an air-cooled structure that consists of radial and ring-shaped elements. The thinner tubes visible just behind the flameholders are the fuel spray bars. Close inspection of the afterburner walls reveals corrugated air-cooling slots that protect the walls from the hot flow.

The afterburner significantly increases the length and weight of the overall aircraft engine, increases total pressure losses due to drag from the spray bars and flameholders, and increases observability due to the flameholder's thermal signature. Afterburner combustion is also notoriously susceptible to thermo-acoustic instabilities, which can cause high cycle fatigue and flame blowout. Moreover, maintaining stable afterburner combustion is becoming more problematic as improvements in combustors and turbines lead to higher afterburner inlet temperatures, which increase the flameholder cooling requirements, and higher inlet velocities, which make flame stabilization more difficult [1].

It is evident that the use of flameholders in an afterburner has many drawbacks. Therefore, an approach that would allow afterburner combustion without flameholders would be very beneficial. Such an approach is the subject of this research.

1.2 The Prime and Trigger Afterburner Concept

The proposed method for afterburner combustion without flameholders will be referred to as the 'prime and trigger' (PAT) concept. Figure 3 shows a schematic of the PAT concept applied to a turbojet engine with an afterburner. In the 'prime' stage of this concept, afterburner fuel is injected into the engine just upstream or within the turbine stages in a manner that allows the fuel to evaporate, mix with the flow, and exit the turbine stage without significant heat release from fuel autoignition. This is achieved by adjusting such parameters as the fuel injection location and spray characteristics to ensure that the travel time of the fuel through the turbine stages is shorter than its combined evaporation, mixing and chemical ignition delay times. The purpose of the prime stage is to produce a fully mixed fuel/vitiated-air[1] mixture at the afterburner inlet that is near the point of autoignition. The fuel in this 'primed mixture' no longer contains the original Jet-A blend of molecules; it has already progressed partly through its autoignition chemical mechanism, so it already consists of simpler hydrocarbon molecules and increasing concentrations of radicals and CO. This primed mixture could either autoignite in the afterburner, as depicted in the top half of Figure 3, or would be easier to ignite than a fresh fuel/vitiated-air mixture. If combustion occurs through autoignition, the onset and

[1] Vitiated-air is the high temperature, reduced-oxygen content product gas of lean fuel/air combustion. In the turbine engine, vitiated-air refers to the products of the main combustor.

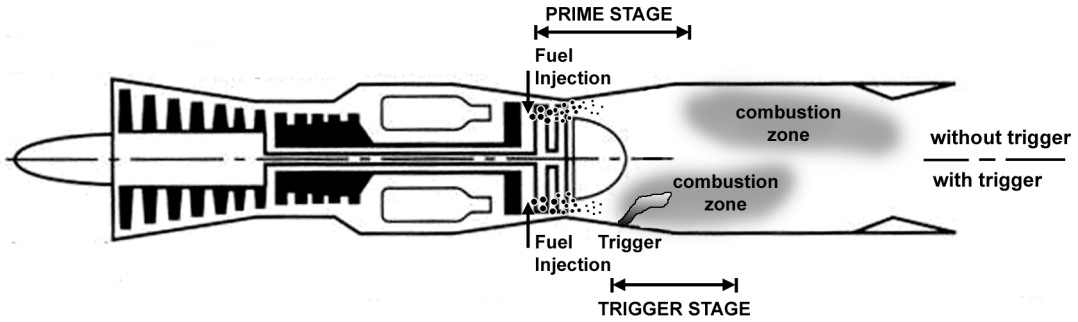

Figure 3. The PAT concept in a dual-spool turbojet afterburner. The top half of the afterburner duct depicts combustion through autoignition and the bottom half depicts combustion with a trigger mechanism.

completion of heat release depend entirely on the engine operating conditions and the afterburner fuel injection location and spray characteristics. However, if fuel autoignition does not occur or if autoignition does not produce a combustion zone that is stable and efficient, then a low power pilot, or 'trigger', can be implemented to control the combustion process.

The envisioned trigger for the PAT concept is a jet of product gas from ultra-rich hydrocarbon/air combustion that is injected through the afterburner liner. The ultra-rich combustion process, referred to as partial oxidation (POx), can convert a hydrocarbon fuel, such as kerosene, to H_2, CO, CH_4, N_2, CO_2, H_2O and smaller quantities of radicals and other light hydrocarbon molecules – a mixture referred to as POx gas. References [2-4] provide descriptions of POx reaction mechanisms and examples of POx reactors. When injected into the high temperature afterburner flow, the POx gas, especially its H_2 component, rapidly produces radicals and heat that accelerate the autoignition of the primed mixture and, thus, provide an anchor point for the afterburner combustion zone. The use of POx gas as a trigger for the PAT concept was inspired, in part, by its use in controlling the ignition delay in homogeneous charge compression ignition (HCCI) engines. An investigation by Eng. et al [5] suggested that POx gas promotes the

autoignition of isooctane for HCCI combustion, which is also the desired effect in this application. For the PAT concept, the POx gas would be produced on-board using the same aviation fuel that is used in the turbine engine. This would require the diversion of a small amount of air from the core flow into an auxiliary reactor, termed the POx reactor. Since the development of the POx reactor and its incorporation into an aircraft engine is the subject of a separate ongoing investigation, it is not discussed in this thesis.

1.3 Research Objective and Overview

The objective of this research was to demonstrate the feasibility of the PAT afterburner concept. The PAT afterburner is feasible if (1) combustion of fuel that is injected within or upstream of turbine stages occurs only downstream of the turbine stages and (2) the combustion zone is compact, stable and efficient. The feasibility of the PAT afterburner was investigated through parallel experimental, theoretical and numerical efforts that were divided into two phases. The first phase was the study of the prime stage, which addressed the following questions:

- Is the ignition delay time of liquid aviation fuel (Jet-A) long enough so that it can be injected upstream or within turbine stages and exit the turbine stages without producing significant heat release?
- Will the primed mixture that exits the turbine stages autoignite in the afterburner?
- How do changes in fuel injection location, spray characteristics and engine operating conditions affect the prime stage and autoignition of the fuel?

The experimental and theoretical efforts that addressed the above questions showed that the prime stage of the PAT concept is feasible. Therefore, the investigation continued

into the second phase – the study of the trigger stage. The second phase addressed the following questions:

- Can the proposed trigger mechanism control and enhance the combustion process in ways that are advantageous to afterburner operation - i.e., reduce sensitivity to changing operating conditions, decrease the combustion zone length, increase combustion efficiency and suppress combustion zone fluctuations?
- How much trigger gas is needed in order to produce the desired performance?
- What trigger gas properties determine its effect on the combustion process, i.e., how does it work?

Although POx gas is the intended trigger for the PAT concept, a combustor that can generate POx gas was not available for this investigation. Consequently, the POx gas trigger was studied numerically, and the experiments employed a H_2 trigger instead. H_2 is a POx gas constituent and, thus, has related effects on the primed mixture combustion process, as will be described. In fact, H_2 represents a 'best case' trigger and serves as a reference for judging the relative effectiveness of different POx gas compositions. The H_2 trigger was also studied numerically to provide preliminary comparisons with the POx gas results and with the H_2 trigger experiments.

This investigation centered on experiments in a developed afterburner facility (AF). The AF is a model of the envisioned PAT concept in a turbojet engine with an afterburner, which was illustrated in Figure 3. Specifically, the AF simulates the O_2 content and the bulk flow temperature and velocity profiles through a turbojet combustor, turbine stage and afterburner. The prime stage is simulated by injecting liquid Jet-A into the AF at locations upstream of the section that models a turbine stage, termed the turbine

simulator (TS). The trigger stage is simulated by a H_2 jet injected normal to the flow just downstream of the TS. The purpose of the AF experiments was to determine if Jet-A injection upstream of the TS produces an autoignition combustion zone only downstream of the TS; to examine the effect of varying injector location, Jet-A flow rate, and AF operating conditions; and to demonstrate the effect of the H_2 trigger on the combustion zone position, length, stability and efficiency.

In the first phase of this research program, the AF experiments were supported by results from a theoretical model. The developed model simulated the physics of fuel priming and autoignition in the AF and, thus, was used to help interpret the AF experimental results. The model was also used for prime stage studies that were not achievable with the AF because of cost and time constraints.

In the second phase of this research program, the AF results were supplemented by Chemkin simulations and measurements in a second experimental facility, termed the Propane Autoignition Combustor (PAC). Chemkin was used to simulate the POx gas and H_2 trigger mechanisms (it is the numerical effort mentioned above). This was achieved by adding H_2 or POx gas to a reacting Jet-A/vitiated-air mixture in a closed homogeneous batch reactor model. The purpose of the Chemkin study was to examine the effect of several POx gas compositions on the Jet-A/vitiated-air autoignition process; to compare the POx and H_2 triggers; and to explore several reasons for why POx gas and H_2 are suitable trigger mechanisms. The PAC was used for basic experimental studies of the H_2 trigger mechanism. It was essentially a scaled-down version of the AF with simplified prime and trigger stages. The purpose of the PAC experiments was to address certain deficiencies in the AF measurement techniques; to study the feasibility of the trigger

stage at gas compositions outside the AF operating range; and to demonstrate a combustion zone analysis procedure that was later applied to the AF results.

The remainder of this thesis consists of four Parts. Part 1 describes the design and development of the AF and PAC facilities. Part 2 describes the first phase of this research program - the investigation of the prime stage. It includes the description of the theoretical model; the results from the AF prime stage experiments and their comparison with theoretical predictions; and the theoretical evaluation of fuel priming and autoignition at high AF operating pressure. Part 3 describes the second phase of this research program - the investigation of the trigger stage. It includes the results from the Chemkin simulations, the PAC experiments, and the AF experiments with the H_2 trigger. Finally, Part 4 provides the review, conclusions, and future work recommendations.

PART 1

THE EXPERIMENTAL FACILITIES

CHAPTER 2 THE AFTERBURNER FACILITY

This chapter describes the design and development of the AF. The first section describes the initial AF design for the first part of this research program, the investigation of the prime stage, and the second section describes the modifications to the AF for the second part of this research program, the investigation of the trigger stage.

2.1 The Initial AF Design

The AF was designed to simulate the velocity, temperature and O_2 content of the flow through the primary combustor, turbine stage and afterburner of a turbojet engine. Turbine engine operating pressures were not simulated due to the added cost and complexity of constructing a high pressure facility. Figure 4 shows a picture of the developed facility and Figure 5 and Figure 6 show schematics of the side and top views of the facility, respectively. In the AF, air first enters the primary combustor where it reacts with methane to generate a vitiated-air stream of desired properties. Next, the vitiated-air passes through a plenum, where the cross-sectional area changes from circular to rectangular, and then through a converging section where the flow accelerates to high subsonic Mach numbers. Liquid Jet-A for afterburner combustion is injected in the plenum or the converging section using the coaxial airblast atomizer shown in Figure 7. The flow then passes through a turbine simulator (TS), which is discussed below. Finally, the flow passes through a diverging section, which is equipped with a quartz window for optical access, followed by a straight duct that simulates the afterburner. Autoignition of

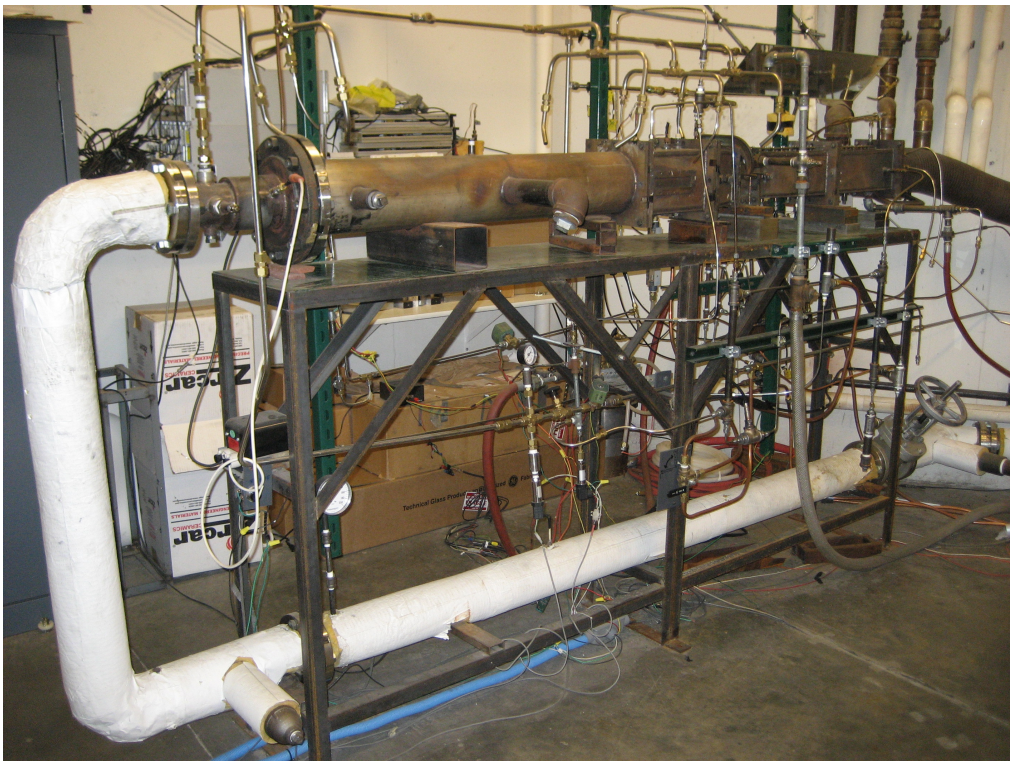

Figure 4. The Afterburner Facility

the afterburner fuel is intended to occur either in the diverging section or the constant-area afterburner section, depending on the injection location and operating conditions.

The TS was designed to simulate the temperature drop and velocity change through a turbine stage. Figure 8 shows a cross-section of the TS as well as a schematic of an actual turbine stage for comparison. In the turbine stage of an aircraft engine, the flow accelerates through the stator and decelerates through the rotor with a net increase in velocity. There are also sharp pressure and temperature drops due to the gas expansion and work extraction by the rotor. In the TS, the stator and rotor are simulated by a row of water-cooled, diamond-shaped blades. Between the blades, the flow passages converge and diverge with a net decrease in cross-sectional area in order to simulate the change in velocity across the stator and rotor. Since work extraction is not possible with the TS, a temperature drop is achieved by heat transfer from the hot flow to the water cooled

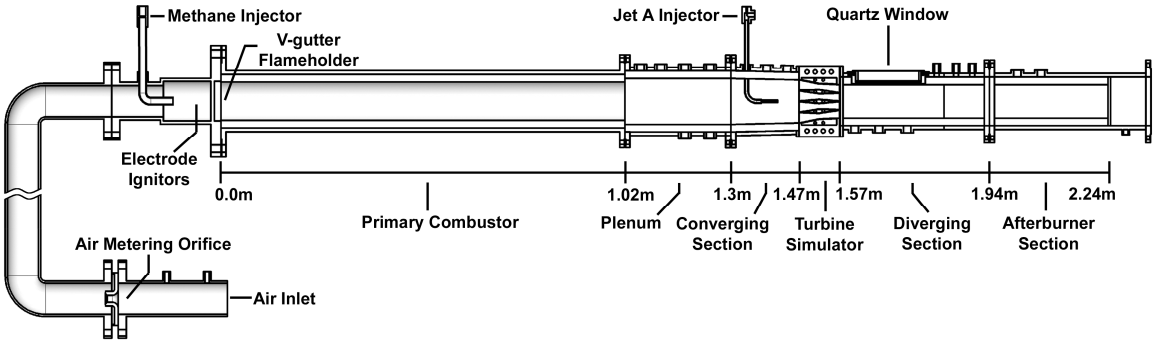

Figure 5. Schematic of the AF

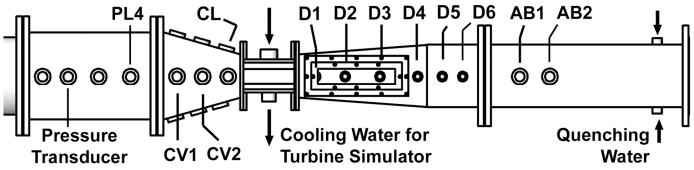

Figure 6. Top view of the sections downstream of the primary combustor. Ports are labeled according to section and downstream order. The section labels are: Plenum, PL; Converging Section, CL; diverging section, D; afterburner section, AB. "CL" is the port on the left side of the converging section

blades and also by a small amount of water injection into the bulk flow from holes on the leading edges of the blades. Other than lowering the bulk flow temperature, the presence of the additional water in the vitiated-air stream was assumed to have little effect on the chemical kinetics of the afterburner fuel, as suggested in [6].

With the exception of the TS, the inner walls of the facility are lined with insulation that consists of 1.59 cm (5/8 in.) thick alumina/silica ceramic and 0.318 cm (1/8 in.) thick quartz. Figure 9 shows the insulation and quartz in the interior of the primary combustor, plenum and converging section. The insulation was used to minimize heat losses and to protect the walls from the hot flow, thus eliminating the need for an extensive set of regenerative, air-cooled liners similar to those employed in real engines. The ceramic provides the majority of the insulation and the quartz prevents erosion of the

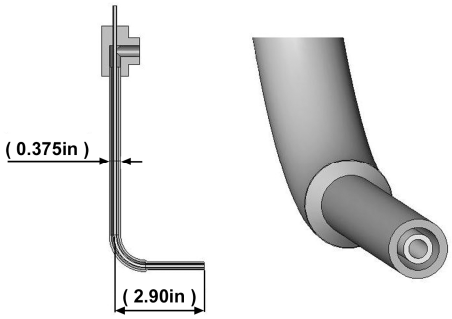

Figure 7. Coaxial airblast atomizer for Jet-A injection. Jet-A flows from the inner tube and air flows through the annulus. The ID and OD of the fuel tube are 0.08in. and 0.125in., respectively. At the discharge, the ID of the air tube is 0.18in.

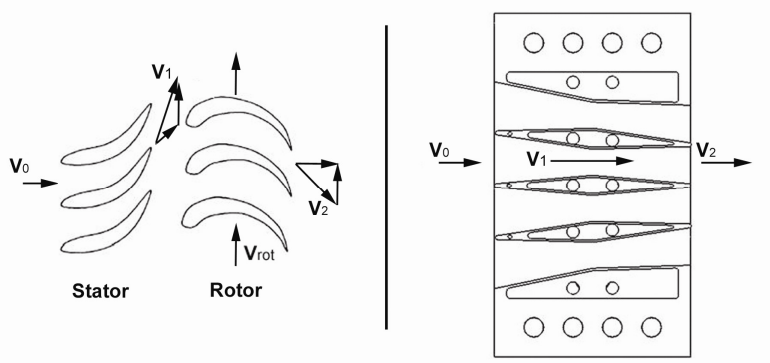

Figure 8. Vector diagram and schematic showing the relationship between the velocity vectors across a turbine stage and those across the turbine simulator.

ceramics. The insulation in the sections with square cross-section consists of interlocking plates of ceramic (Zircar Ceramics - SALI I, 80:20% alumina/silica) and quartz. The insulation in the primary combustor consists of three alumina ceramic casts (Cotronics Corp. - Rescor #780) that surround a long quartz tube. The casts are also wrapped with an alumina mat (Zircar Ceramics) for additional insulation.

The developed facility has capabilities for measuring temperature, pressure, fuel and air flow rates and chemiluminescence. These measurements were used during operation to bring the facility to turbine operating conditions and to detect the Jet-A/vitiated-air combustion process. The temperature of the bulk flow was measured using B-type thermocouples, which measure temperatures up to 1700^{o}C. The methane and air

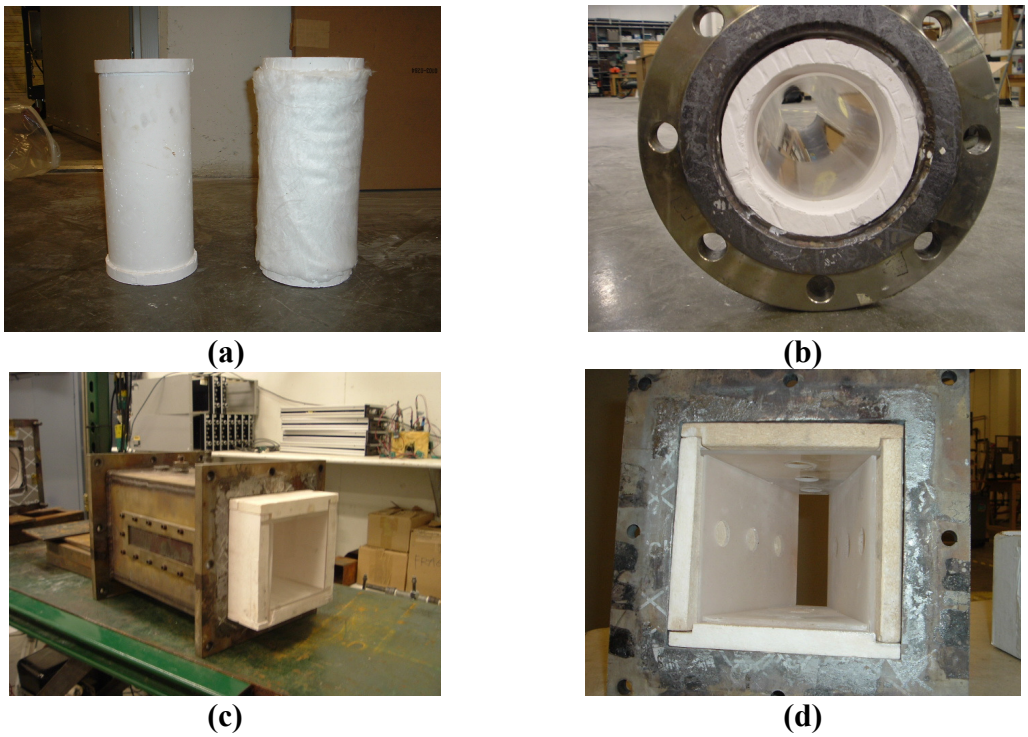

Figure 9. The insulation in the AF: (a) Alumina casts, the cast at right is surrounded by the alumina mat; (b) alumina casts, mat, and quartz tube installed in the primary combustor section; (c) interlocking alumina/silica ceramic and quartz panels pulled slightly out of the Plenum section; (d) alumina/silica and quartz panels in the converging section showing the holes for thermocouples and fuel injection.

flow rates were determined from pressures and temperatures measured upstream of choked metering orifices. Jet-A flow rates were measured using a rotameter and a flow meter with a range of 1-1250ml/min. CH* chemiluminescence was measured by a CCD video camera equipped with a filter (430 ± 5 nm) that was positioned over the quartz window in the diverging section.

The AF development was one of the most challenging aspects of this research. Originally, the facility could not be operated more than once without having to replace a significant portion of the insulation. The ceramics fractured often because of mechanical vibrations and thermal cycling, and they eroded due to the high gas velocities. This resulted in time-intensive and costly maintenance, as well as potentially hazardous conditions due to the presence of ceramic dust in the flow. To reduce erosion, the

ceramics were treated with a silica rigidizer and then lined with the quartz panels. Quartz was used because it can withstand thermal cycling and high temperature, although it introduced additional difficulties because it is fragile and difficult to machine. In a parallel effort, alternative insulating materials[2] were tested but were all found to be unsuitable for various reasons such as temperature restrictions, low tolerance to thermal shock, availability, machinability and carcinogenicity. As a result, the alumina/silica ceramic and quartz plate insulation system was deemed the best option for the sections with square cross-section. In the primary combustor section, the long alumina/silica cylinder that was used originally was replaced by the alumina casts shown in Figure 9(a). The advantage of using these alumina casts instead of the alumina/silica ceramics is their lower cost; their harder surface, which greatly reduces erosion; and, most importantly, the absence of amorphous silica in their composition, which can form carcinogenic crystalline silica after long term exposure to the high temperature oxidizing environments present in the AF.

Ultimately, the lifetime of the insulation was greatly improved by optimizing the primary combustor flameholder to reduce mechanical vibrations in the facility. The flameholder consists of two v-shaped gutters crossed at a 90^{o} angle. The blockage ratio of the flameholder and the distance between the methane injector and the flameholder were adjusted to minimize audible instabilities. In addition, the diameter of the section upstream of the primary combustor was increased to decrease the velocity of the flow

[2] Alumina boards with varying ratios of alumina oxide to silica oxide, graphite felt boards with and without abrasion resistant coating, alumina silicate plates, graphite plates with and without silicon carbide refractory coating, 99.5% alumina plates, mullite plates

impinging on the flameholder. This last step also greatly increased the stability of the primary combustion process.

2.2 Modifications to the AF

After using the AF for the first phase of this research program, it was modified to address the goals of the second phase, which was the investigation of the trigger stage. Figure 10 shows a top view image and schematic of the sections downstream of the TS, where the modifications were made. A port for H_2 injection was added approximately 4.5 cm downstream of the TS outlet. The H_2 was injected through a 0.318 cm (1/8in.) tube, whose outlet was flush with the inner wall of the diverging section insulation. Two additional quartz windows were added to the diverging and afterburner sections. These windows extended the optical access so that the entire Jet-A combustion zone could be observed (with the exception of the spaces between each window). An additional thermocouple port (B4) was added to measure the core flow temperature near the AF outlet. Finally, a gas sampling line was inserted near the outlet for measurement of the

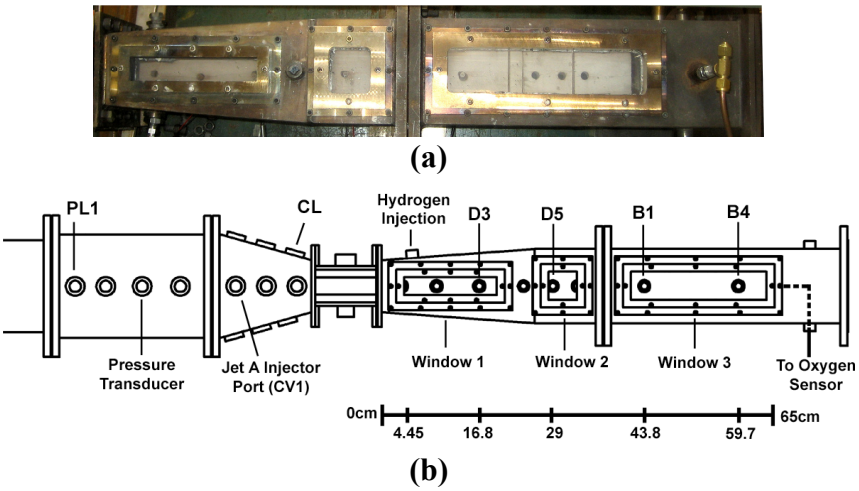

Figure 10. (a) Top-view image and (b) top-view schematic of the sections downstream of the primary combustor showing the modifications for the investigation of the trigger stage. The schematic includes a new axis that is used for the trigger stage investigation.

bulk flow dry O_2 content. The sampling line is an L-shaped stainless steel tube centered in the duct and pointed in the upstream direction, as depicted by the dashed line in Figure 10. It directs a small portion of the bulk flow through a water trap and into a chamber that houses a Lambda O_2 sensor. The flow is forced through the sampling line by the difference between the total pressure at its inlet and the negative pressure created by a gas ejector at its outlet.

For the trigger stage investigation, the CCD camera was replaced with a Redlake high-speed camera. The Redlake camera was operated at 60 frames per second with an exposure time of 1/60sec. A 430+/-5nm filter was placed in front of the lens to record the CH* chemiluminescence from the combustion zone. The camera was positioned sufficiently far away from the facility to view the full length of the diverging and afterburner sections with a resulting image resolution of approximately 1.3 mm per pixel.

CHAPTER 3 THE PROPANE AUTOIGNITION COMBUSTOR

The PAC was used to study propane autoignition in vitiated-air with and without a H_2 trigger. Figure 11 shows a picture and a schematic of the PAC and Figure 12 shows pictures of the primary combustor section. The inlet air flow is split into four lines that are tangentially inserted into the gap between the casing and liner of the primary combustor. The injected air swirls around the gap and passes over small bumps dotting

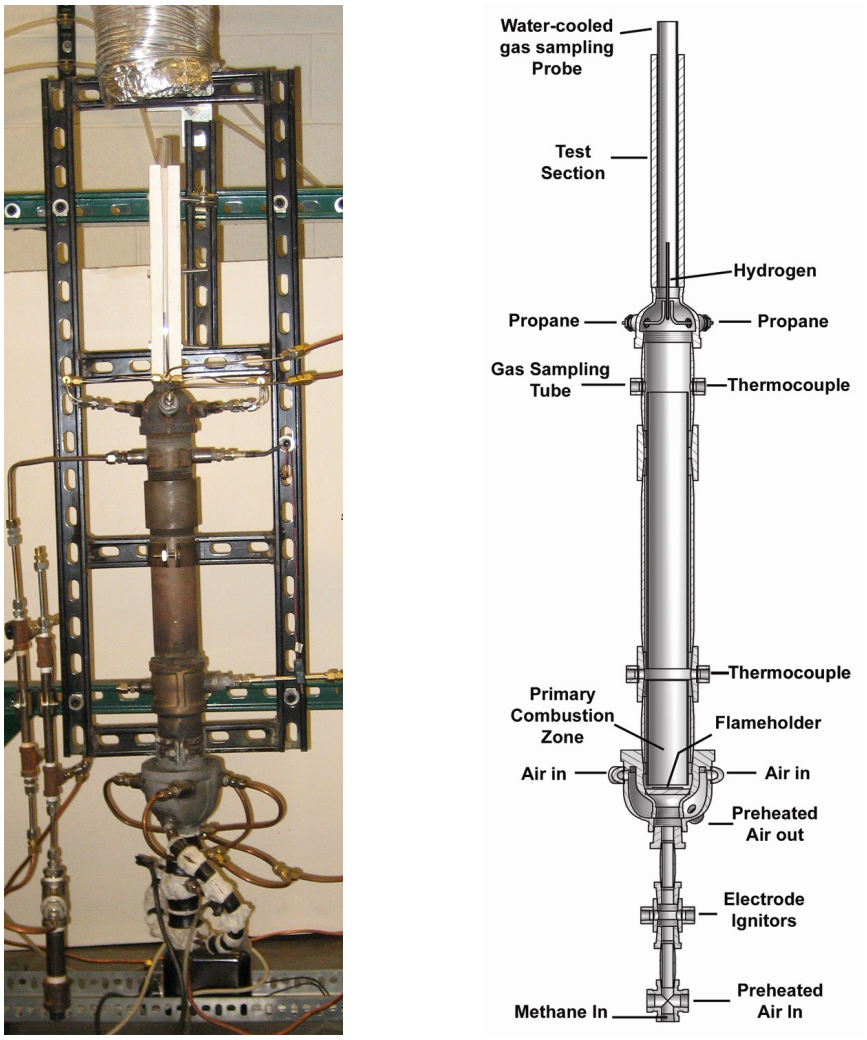

(a) **(b)**

Figure 11. (a) Picture and (b) schematic of the PAC

the surface of the liner that enhance heat transfer. The air exits the gap through two tubes that are insulated with an alumina blanket, as shown in Figure 12(a). These tubes guide the pre-heated air into an insulated pipe assembly where it mixes with methane, passes electrode igniters, and enters the primary combustion zone. The remainder of the PAC is essentially a scaled-down version of the AF without the TS. Combustion of methane and air in the primary zone is stabilized by a bluff-body flameholder. In this setup, the flameholder consists of a stainless-steel disc welded onto 0.635 cm (1/4 in.) diameter cylindrical crossbars. The generated combustion products (vitiated-air) then move through a pipe that is insulated from the flow by a quartz tube surrounded by a braided silica sleeve. The flow exits the pipe through a reducing coupling and enters the test section where propane autoignition takes place.

Figure 13(a) shows a picture of the autoignition test section during operation of the PAC and Figure 13(b) shows a schematic of the test section. Propane vapor is injected into the PAC via four tubes pointing in the downstream direction. The propane flow was split into four tubes to reduce its mixing time with the bulk flow. The resulting

(a) **(b)**

Figure 12. Pictures of the primary combustor section of the PAC: (a) as installed on the rest of the facility (b) un-installed with view of the flameholder.

propane/vitiated-air mixture then enters a 2 cm diameter by 25 cm long quartz tube, where autoignition takes place. To minimize heat loss, the quartz tube is surrounded by alumina/silica ceramic that has an axial slot on only the front side for optical access to the autoignition combustion zone. In contrast to the segmented AF windows, this long 'window' allows the measurement of continuous chemiluminescence intensity profiles. To simulate the PAT concept in the PAC, H_2 is injected into the test section 5.1 cm downstream of the propane tube outlets. As shown in Figure 13, it is injected through a metal tube that points in the downstream direction and is centered in the flow. By the time the propane/vitiated-air mixture reaches the H_2 tube outlet, it has already begun to react. Thus, the H_2 can 'trigger' or accelerate the autoignition of the 'primed' propane/vitiated-air mixture.

The PAC has capabilities for measuring air and fuel flow rates, temperature, pressure and gas composition. The air and fuel (methane, propane and H_2) flow rates were calculated using pressure measurements upstream of calibrated, choked-flow orifices. Temperature was measured by B-type thermocouples at the end of the primary combustor and near the inlet of the test section. A Horiba gas analyzer was used to measure dry O_2 and dry CO_2 mole fractions (%vol.). A water-cooled probe was positioned at the outlet of the test section to draw a gas sample, which then passed through a water trap and into the gas analyzer. Initially, gas samples were also drawn through the port opposite the upper thermocouple, see Figure 11(b), to check whether complete primary combustion occurred.

An optical spectrometer (Ocean Optics HR2000) was used to measure the spatial dependence of radiation intensity along the length of the test section. The spectrometer

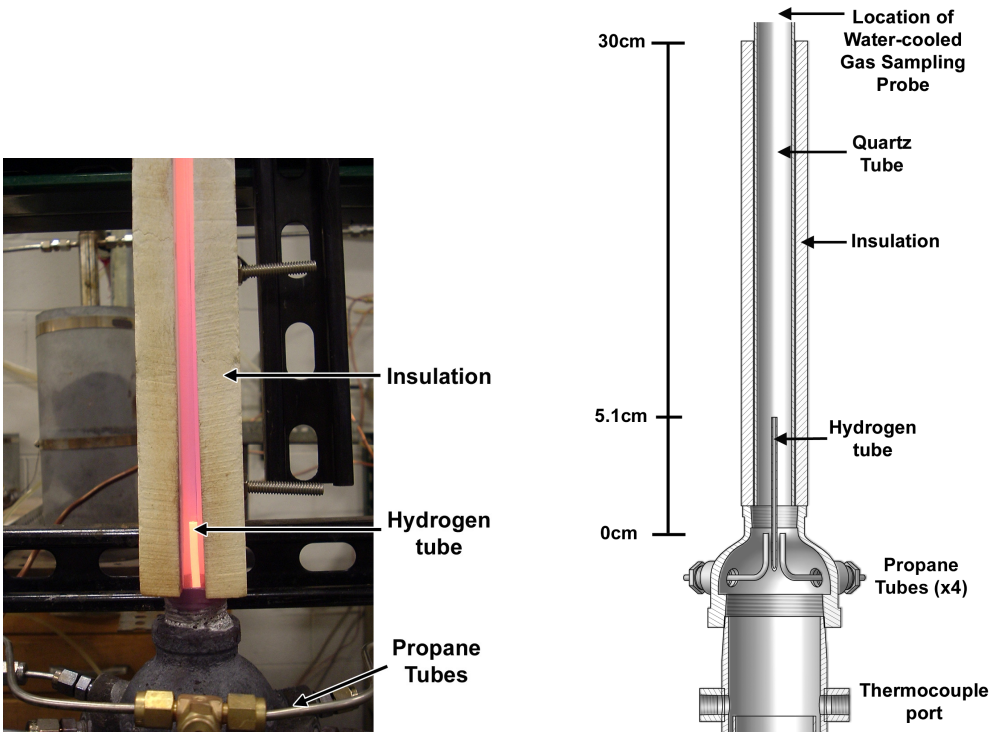

Figure 13. (a) Picture of test section during operation and (b) schematic of the test section.

was used instead of the 430+/-5nm filter that was used in the AF to allow the additional measurements of background radiation and OH* chemiluminescence intensity. The spectrometer measured radiation in the 200 to 650nm range with a resolution of about 0.5 nm/pixel in the center of the band. The optics consisted of two quartz UV lenses mounted on a vertical traverse that scanned the optics line of sight along the axial slot in the ceramic insulation. A quartz optical fiber guided the light from the lens to the spectrometer. In this application, the spectrometer captured a line-of-sight integral of radiation intensity that was 20mm in length and approximately 4mm in diameter. The spectrometer also captured the radiation from the quartz tube and from the ceramic insulation on the backside of the test section. Thus, the spectrometer measured radiation from the same sources viewed by the camera in the AF.

PART 2

THE INVESTIGATION OF THE PRIME STAGE

Part 2 describes the first phase of this research effort - the theoretical and experimental investigation of the prime stage. As stated previously, the objective of this phase was to answer the following questions:

- Is the ignition delay of liquid aviation fuel (Jet-A) long enough so that it can be injected upstream or within a turbine stage and exit the turbine stages without producing significant heat release?
- Will the primed mixture that exits the turbine stages autoignite in the afterburner and, if so, where?
- How do changes in fuel injection location, spray characteristics, and engine operating conditions affect the prime stage and the autoignition of the fuel?

Part 2 proceeds as follows: the first chapter describes the developed theoretical model; the second chapter describes the experimental results from the AF and their comparison with theoretical predictions; and the last chapter describes the theoretical evaluation of fuel priming and autoignition at realistic turbine engine pressures.

CHAPTER 4 THEORETICAL CONSIDERATIONS

A reduced-order theoretical model was developed to predict the autoignition location of the afterburner fuel in the AF as a function of the operating conditions, the Jet-A injection location, and the estimated Jet-A spray sauter mean diameter (SMD). The main purpose of the developed model was to help interpret the experimental results. However, it also served as a stand-alone tool for the evaluation of the PAT concept over a wider range of injection locations and operating conditions than can be achieved in the AF. The developed model is described below and is also illustrated in Figure 14 and Figure 15. It should be noted that it requires prior knowledge of the bulk flow temperature, pressure and velocity along the AF. These are estimated by solving the one-dimensional conservation equations of mass, momentum and energy with boundary conditions given by measured temperatures, pressures, and fuel and air flow rates, as described in Section 4.4.

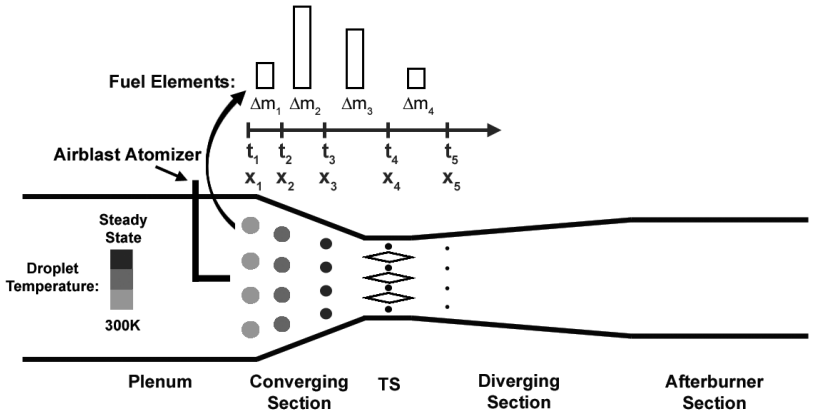

Figure 14. Illustration of droplet convection, heat-up, and evaporation in the developed model. The solid outline represents the AF and the hollow diamonds represent the TS blades. The scale above the AF depicts four time and space increments of the model, although with much courser resolution. Each group of four vertical circles within the AF outline represents the droplets moving along the AF. In each time step, the droplets move downstream, increase in temperature due to heat transfer from the bulk flow (see color bar), and decrease in diameter due to evaporation. The bars above the time/space scale represent the relative amount of mass that evaporates in each interval.

The autoignition of the afterburner fuel in the AF was assumed to be governed by three processes: evaporation, mixing and chemical reactions. As illustrated in Figure 14, the developed model follows a group of Jet-A droplets, which is produced by the airblast atomizer shown in Figure 7, as it is carried through the AF by the bulk flow. The vaporization rate of the droplets is computed in increments of time and space and the quantity of fuel that evaporates from the group of droplets in each increment is referred to as a 'fuel element'. As the group of droplets moves along the facility, it 'releases' fuel elements of varying mass depending on the vaporization rate. Each fuel element is then tracked independently, as illustrated in Figure 15. It is assumed that a fuel element 'acquires' the velocity of the local bulk flow as soon as it forms. As it travels along the facility, the fuel element approaches the temperature of the local bulk flow through a mixing process that is modeled using a characteristic mixing time, τ_{mix}. Concurrent with this mixing process, each fuel element undergoes chemical reactions that ultimately result

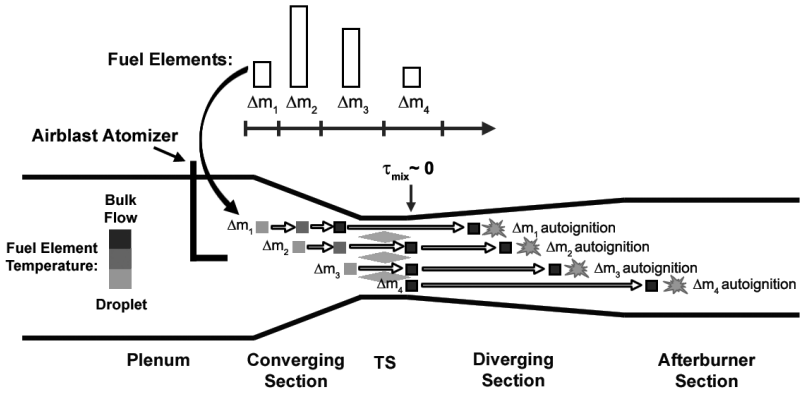

Figure 15. Illustration of fuel element convection, temperature change, and autoignition in the developed model. The solid outline represents the AF, and the solid, gray diamonds represent the TS blades. The scale above the AF depicts four time and space increments of the model, although with much courser resolution, and the bars above the scale indicate the relative mass of the fuel elements created in each interval. The solid squares within the AF outline represent each fuel element in the bulk flow, and the hollow arrows represent the path of each fuel element in time. As they travel along the facility, the fuel elements heat up to the local bulk flow temperature (see color bar) through a process that depends on a characteristic mixing time (τ_{mix}). Concurrently, each fuel element undergoes chemical reactions that result in its autoignition.

in its autoignition. These chemical reactions are modeled using a simple, zero-order model for chemical ignition delay that takes into account temporal variations of bulk flow temperature and pressure. By computing the ignition delay time (and, thus, the autoignition location) of all the fuel elements, the model determines the percent of fuel that has ignited at each position along the facility.

The following sections describe the developed evaporation, mixing and chemistry sub-models ending with an example of their use for the prediction of autoignition in the AF.

4.1 Evaporation Sub-Model

The vaporization sub-model uses a procedure developed by Abramzon et al [7] to calculate the vaporization rate, velocity and temperature of a group of Jet-A droplets. There are two types of assumptions: model and application specific. The model, as developed in [7], has the following assumptions:

- The gas phase heat and mass transfer are quasi-steady.
- The pressure drop in the gas is negligible.
- The gas thermo-physical properties are uniform about the droplet surface and are evaluated using a reference temperature and composition, see Equations (4.4) and (4.5).
- The droplet has uniform temperature, composition, and thermo-physical properties.

The application specific assumptions are:

- The atomization time is negligible.

- The droplet density is a constant $815 kg/m^3$.
- The initial fuel temperature is 300K.
- All the droplets have the same diameter and velocity.
- The initial diameter of the droplets is the SMD of the spray produced by the Jet-A airblast atomizer, see Figure 7.

The SMD was estimated using the following empirical expression developed by Jasuja [8] for coaxial airblast atomizers:

$$SMD = 0.19\left(\frac{\sigma_f}{\rho_f}\right)^{0.35}\left(u_{air,inj}\rho_{air,inj}^{0.35}\right)^{-1}\left(1+\frac{\dot{m}_{JetA}}{\dot{m}_{air,inj}}\right)^{0.25} +0.127\mu_f\left(\frac{D_{inj}}{\rho_f\sigma_f}\right)^{0.5}\left(1+\frac{\dot{m}_{JetA}}{\dot{m}_{air,inj}}\right) \tag{4.1}$$

where D_{inj} is the inner diameter of the fuel tube, see Figure 7, and $\dot{m}_{air,inj}$, $\rho_{air,inj}$ and $u_{air,inj}$ are the injector air flow rate, density, and velocity, respectively[3]. The fuel thermo-physical properties were obtained from Refs. [7,9-11]. Kerosene properties were used where available, otherwise Decane properties were used. Appendix A provides tables of the fuel thermo-physical properties used in this study and describes the procedure for computing fuel-vapor/vitiated-air mixture properties.

The vaporization of the group of fuel droplets was calculated over constant increments of time, $\Delta t = 10\mu\sec$, starting from $t = 0$ when the droplets are formed at the injector outlet. In the i[th] increment of time, from $t = t_i$ to t_{i+1}, the fuel that vaporizes from

[3] See the Nomenclature section for definitions of the various other quantities used in this analysis

the group of droplets is called the i[th] fuel element. The mass of this fuel element, denoted as Δm_i, is given by

$$\Delta m_i = N_{drops} \dot{m}_{drop,i} \Delta t \tag{4.2}$$

where $\dot{m}_{drop,i}$ and N_{drops} are the vaporization rate of the fuel droplets in the i[th] increment of time and the number of droplets in the group, respectively. N_{drops} is assumed to be constant throughout the vaporization process. However, the vaporization rate depends on the local bulk flow pressure, temperature, velocity and composition, as well as the diameter and temperature of the droplets, as described below.

Following the model developed in [7], the vaporization rate of a droplet is given by:

$$\dot{m}_{drop} = \pi d_{drop} \bar{\rho} \bar{D}_M Sh^* \ln(1 + B_M) \tag{4.3}$$

Note that for simplicity the subscript *i,* denoting the time increment, has been omitted. Unless stated otherwise, all the terms in the equations correspond to values at time t_i or, equivalently, to the values at the position of the droplets along their trajectory at time t_i. Gas properties with an overbar represent average or 'film' properties in the boundary layer near the droplet surface. These are estimated using the following average or 'film' temperature and fuel mole fraction:

$$\bar{T} = T_{drop} + \frac{1}{3}\left(T_{bulk} - T_{drop}\right) \tag{4.4}$$

$$\bar{\chi}_F = \chi_{F,s} + \frac{1}{3}\left(\chi_{F,bulk} - \chi_{F,s}\right) \tag{4.5}$$

For example, the average gas density, $\bar{\rho}$, is calculated using the ideal gas equation of state: $\bar{\rho} = P_{bulk} MW_{bulk} / R\bar{T}$, where MW_{bulk} is calculated using $\bar{\chi}_F$ and the known vitiated-air composition. $\chi_{F,s}$ is calculated using the ratio of decane fuel vapor pressure to the local ambient pressure and $\chi_{F,bulk}$ is calculated by assuming that all fuel previously vaporized has fully mixed with the bulk flow. The terms appearing in Equation (4.3) are defined as follows:

$$B_M = \frac{Y_{F,s} - Y_{F,bulk}}{1 - Y_{F,s}} \tag{4.6}$$

$$Sh^* = 2 + \frac{Sh - 2}{F_M} \tag{4.7}$$

$$F_M = (1 + B_M)^{0.7} \frac{\ln(1 + B_M)}{B_M} \tag{4.8}$$

$$Sh = 2\left(1 + Fö \,\mathrm{Re}_{drag}^{1/2} \overline{Sc}^{1/3}\right) \tag{4.9}$$

where $Fö$ is the Frössling coefficient, which has a value of 0.276 [12]. The Reynolds number, Re_{drag}, is given by

$$\mathrm{Re}_{drag} = \frac{\rho_{bulk} \left| u_{drop} - u_{bulk} \right| d_{drop}}{\bar{\mu}} \tag{4.10}$$

The droplet velocity after each time increment is computed using the following equation:

$$u_{drop,i+1} = u_{drop,i} + \frac{3C_{drag}}{d_{drop}} \frac{\rho_{bulk}}{\rho_f} \left| u_{bulk} - u_{drop,i} \right| \left(u_{bulk} - u_{drop,i} \right) \Delta t \tag{4.11}$$

where C_{drag} is given by:

$$C_{drag} = \frac{24}{\mathrm{Re}_{drag}}\left(1 + \frac{1}{6}\mathrm{Re}_{drag}^{\,2/3}\right) \tag{4.12}$$

The initial value of u_{drop} is approximated by the fuel flow rate divided by the fuel density and the injector fuel discharge area. u_{drop} is also used to track the position of the group of droplets in time. Having computed $\dot{m}_{drop}$ using Equations (4.3) - (4.12), the droplet diameter is then given by

$$d_{drop,i+1} = d_{drop,i} - \frac{2\dot{m}_{drop}}{\pi\rho_f d_{drop,i}^2}\Delta t \tag{4.13}$$

As indicated by Equation (4.4), the vaporization model also requires knowledge of droplet temperature. The droplet temperature after each time increment is given by

$$T_{drop,i+1} = T_{drop,i} + \frac{\dot{Q}_{l,i}}{\rho_f V_{drop} c_f}\Delta t \tag{4.14}$$

where $\dot{Q}_{l,i}$ is the heat transfer rate into the liquid phase during the ith time step, given by:

$$\dot{Q}_l = \dot{m}_{drop}\left(\frac{\overline{c}_{p,F}\left(T_{bulk} - T_{drop}\right)}{B_T} - \Delta h_{vap}\right) \tag{4.15}$$

where B_T is determined by simultaneously solving the following set of equations:

$$\dot{m}_{drop} = \pi d_{drop}\frac{\overline{k}}{\overline{c}_{p,F}}Nu^* \ln(1 + B_T) \tag{4.16}$$

$$Nu^* = 2 + \frac{Nu - 2}{F_T} \tag{4.17}$$

$$Nu = 2\left(1 + F\ddot{o}\,\mathrm{Re}_{drag}^{1/2}\,\overline{\mathrm{Pr}}^{1/3}\right) \tag{4.18}$$

$$F_T = (1 + B_T)^{0.7}\,\frac{\ln(1 + B_T)}{B_T} \tag{4.19}$$

The value for $\dot{m}_{drop}$ in Equation (4.16) is provided by the solution of Equation (4.3).

4.2 Mixing Sub-Model

The temperature of the fuel element is initially equal to the temperature of the droplet and increases as the fuel element mixes with the bulk flow. Denoting the temperature of the ith fuel element as $T_{\Delta m_i}$, this mixing process is modeled by the following first order rate equation:

$$\frac{dT_{\Delta m_i}}{dt} = \frac{1}{\tau_{mix}}\left(T_{bulk} - T_{\Delta m_i}\right) \tag{4.20}$$

where τ_{mix} is a characteristic mixing time. To estimate the characteristic mixing time, the bulk flow turbulence is assumed to be the dominant mechanism for mixing. Upstream of the diverging section, τ_{mix} is defined as the time it takes for a turbulent eddy to bring a fluid element from the bulk flow to the center of the Jet-A fuel jet, which is estimated as follows:

$$\tau_{mix} = \frac{R_{inj}}{u'} \tag{4.21}$$

where R_{inj} is the radius of the injector tube that carries the liquid fuel, equal to 0.159 cm (1/16in.), and u' is the rms turbulent velocity fluctuation of the bulk flow, which is assumed to be 5% of the local bulk flow velocity. It should be noted that the contribution

to the mixing process of the air used by the atomizer is neglected because it is a relatively small quantity. Downstream of the TS, it is assumed that there is intense turbulent mixing due to strong flow separation and turbulent wakes associated with the TS blades. Therefore, τ_{mix} is set to zero in this region, which corresponds to infinitely fast mixing. As a result, the temperature of a fuel element is discontinuously set to the temperature of the local bulk flow if it is downstream of the TS. This abrupt temperature change is illustrated by the color of the third and fourth fuel elements in Figure 15.

4.3 Chemistry Sub-Model

Concurrent with the mixing process, each fuel element undergoes chemical reactions with the bulk flow that ultimately result in its autoignition. The ignition delay of a fuel element is estimated using empirical correlations that were adapted for use in an environment with transient temperature and pressure.

Typically, experimentally measured ignition delay times are correlated with an inverse Arrhenius type expression of the form

$$\tau_{ign} = A\left[O_2\right]^n P^b \exp\left(\frac{E_a}{RT}\right) \tag{4.22}$$

where τ_{ign} is the measured ignition delay; A, E_a, n, and b are empirical coefficients; and $[O_2]$ is the initial oxygen concentration [13-19]. Equation (4.22) is only valid, however, when the bulk flow temperature and pressure are constant during the autoignition process. In this application, the fuel elements experience varying temperature and pressure as they heat up and travel along the facility. Consequently, the chemical ignition

delay of a fuel element was estimated using the following 'ignition integral', which was derived in [20][4] and used more recently in [21] and [22]:

$$I = \int_0^{t'} \frac{1}{\tau_{ign}(P_{bulk}, T_{\Delta m_i})} dt' \tag{4.23}$$

where P_{bulk} is the bulk flow pressure, t' is the time elapsed since formation of the fuel element under consideration, τ_{ign} is the above-discussed empirical expression for Jet-A chemical ignition delay at constant ambient temperature and pressure, and I is a progress variable, termed the ignition integral value. In this model, the autoignition location of a fuel element is determined by simultaneously solving Equations (4.22) and (4.23) as the fuel element travels along the facility. When $I = 1$, the fuel element is predicted to autoignite and the time in the upper limit of the ignition integral is the predicted ignition delay time of that fuel element.

The expression for τ_{ign} used in this investigation is based on results from the experimental investigation of Jet-A autoignition by Freeman and Lefebvre [14], which was performed at atmospheric pressure. The results from [14] were used to obtain

$$\tau_{ign} = 1.06 \times 10^{-10} \left[O_2\right]^{-0.65} \exp\left(\frac{20582}{T_{\Delta m_i}}\right) \tag{4.24}$$

Expressing the initial bulk flow oxygen concentration, $[O_2]\left(\frac{mol}{m^3}\right)$, in terms of mole fraction and atmospheric pressure and substituting the result into Equation (4.24) yields:

[4] To the knowledge of this author, Ref. [20] is the earliest published appearance of the 'ignition integral'. It has been independently derived, however, in several other publications since then.

$$\tau_{ign} = 1.06 \times 10^{-10} \left(\frac{\chi_{O_2} 101325}{R T_{\Delta m_i}} \right)^{-0.65} \exp\left(\frac{20582}{T_{\Delta m_i}} \right) \tag{4.25}$$

where χ_{O_2} is the O_2 mole fraction in the bulk flow before afterburner fuel injection and R is the universal gas constant. To accommodate changes in bulk flow pressure, the above equation was modified by including the inverse pressure term suggested in [17] and [19], giving

$$\tau_{ign} = 1.06 \times 10^{-10} \left(\frac{\chi_{O_2} 101325}{R T_{\Delta m_i}} \right)^{-0.65} \exp\left(\frac{20582}{T_{\Delta m_i}} \right) \bullet \left(\frac{101325}{P_{bulk}} \right) \tag{4.26}$$

4.4 Demonstration of the Developed Model

In this section, the theoretical model predictions for a typical AF operating point are obtained and post-processed. The purpose of this exercise is to show how the sub-models of mixing, evaporation and chemistry combine to predict the autoignition of the fuel and to identify the theoretical results that can be compared with the experimental results.

An AF operating point is described by the following experimentally measured set of parameters:

$$[P_{PL}(psia),\ T_{tot}(K),\ \Delta T_{TS}(K),\ \dot{m}_{air}(kg/s),\ \phi_{vit},\ \dot{m}_{JetA}(g/s)]$$

which are the plenum static pressure, total temperature upstream of the TS, total temperature drop across the TS, bulk air flow rate, primary combustor equivalence ratio, and Jet-A flow rate, respectively. The following typical AF operating point, denoted as Case A, will be used to demonstrate the developed model:

$$[P_{PL},\ T_{tot},\ \Delta T_{TS},\ \dot{m}_{air},\ \phi_{vit},\ \dot{m}_{JetA}] =$$

Case A: $[30\,psia, 1500K, 150K, 0.22\,{}^{kg}/_{s}, 0.42, 2.03\,{}^{g}/_{s}]$

The first step in the analysis of Case A is to use the operating point parameters to estimate the axial variation of the bulk flow temperature, pressure and velocity from the plenum to the outlet of the facility. As mentioned previously, these profiles are determined by solving one-dimensional conservation equations of mass, momentum and energy. These include terms accounting for friction and heat transfer through the walls of the facility. First, the primary combustor exhaust composition is computed using ϕ_{vit} assuming complete combustion with no dissociation. Next, the computed gas composition and the measured P_{PL}, T_{tot}, and $\dot{m}_{air}$ are set as the plenum inlet conditions, and the bulk flow profiles are computed by stepping along the facility and accounting for the effects of area change, friction and heat loss. Some constraints are imposed on the flow analysis through the TS. The static pressure at the TS throat is set to 1 atm to be consistent with measured data. In addition, the total temperature drop across the TS, which occurs due to heat transfer and water evaporation, is assumed to be linear and is computed using the measured value of ΔT_{TS}. With these constraints, the conservation equations are solved to determine the remaining TS bulk flow profiles.

Figure 16 shows the calculated axial bulk flow profiles of temperature, pressure and velocity along the AF for Case A. Figure 16(a) shows the total and static pressure profiles along the facility. The total pressure profile indicates that there is negligible total pressure loss due to friction outside of the TS. The total pressure drop across the TS is largely caused by the strong flow separation downstream of the TS midpoint, which is represented in the model by the aforementioned TS flow analysis constraints. Figure

16(b) shows the profiles of the bulk flow total and static temperature and the profile of wall temperature. The total temperature profile shows that excluding the TS the predicted total temperature loss between the plenum and the AF exhaust is only about 45K. This low temperature loss is made possible by the insulation along the interior of the facility. The inner wall temperatures are predicted to be within 100K of the bulk flow temperature except for in the TS, which is water cooled. Finally, Figure 16(c) shows the profiles of bulk flow velocity and Mach number. These represent typical values achieved in the AF.

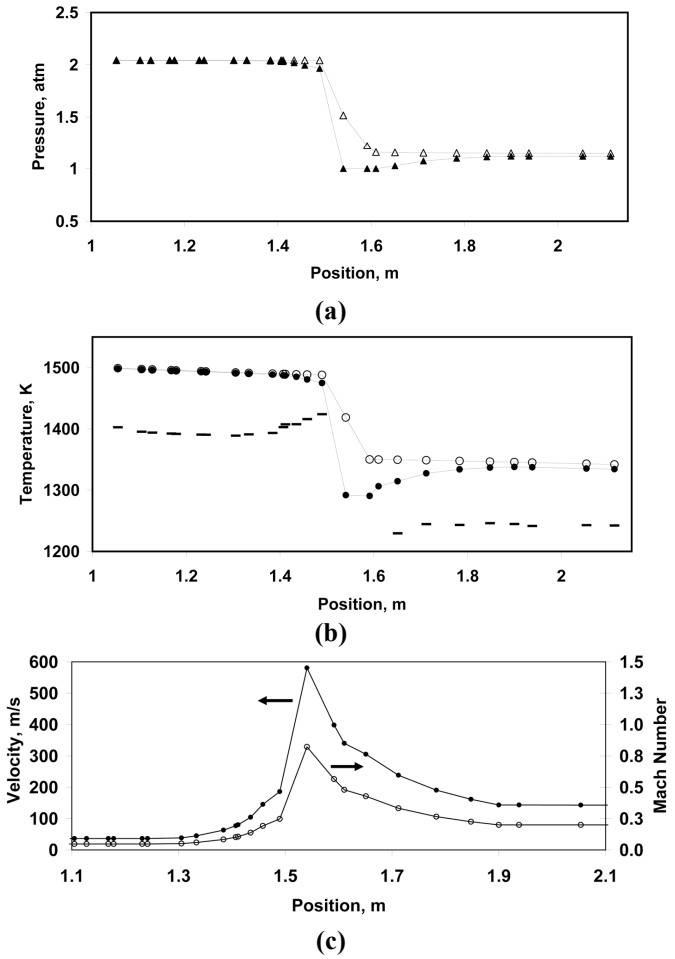

Figure 16. Flow analysis results for Case A: (a) Total pressure (open) and static pressure (closed); (b) total temperature (open), static temperature (closed), and wall temperature (dash); and (c) velocity and Mach number.

The velocity at the TS throat is 580 m/s, which corresponds to a Mach number of 0.82, and the velocity through the diverging and afterburner sections ranges from 340 m/s to 140 m/s, corresponding to Mach numbers of about 0.5 to 0.2, respectively.

The computed axial velocity profile can be used to estimate the flow travel time through the AF. This is shown in Figure 17 for various bulk flow starting positions. Note that since fuel elements travel with the bulk flow, each profile also represents the travel time of a fuel element that is created at the initial (zero travel time) location. The first (leftmost) profile begins in the plenum at about 1.2 m, where the velocity is the lowest because of the relatively large cross-sectional area. Following the first profile, as the gas travels into the converging section, the bulk flow velocity increases and, thus, the profile slope decreases. The slope increases again downstream of the TS midpoint, at about 1.54 m, and then reaches a constant value at about 1.8 m, where the facility becomes a straight duct. Extrapolation of this first profile to 2.24 m shows that for Case A the flow takes about 12 msec to travel from within the plenum to the outlet of the facility. In addition,

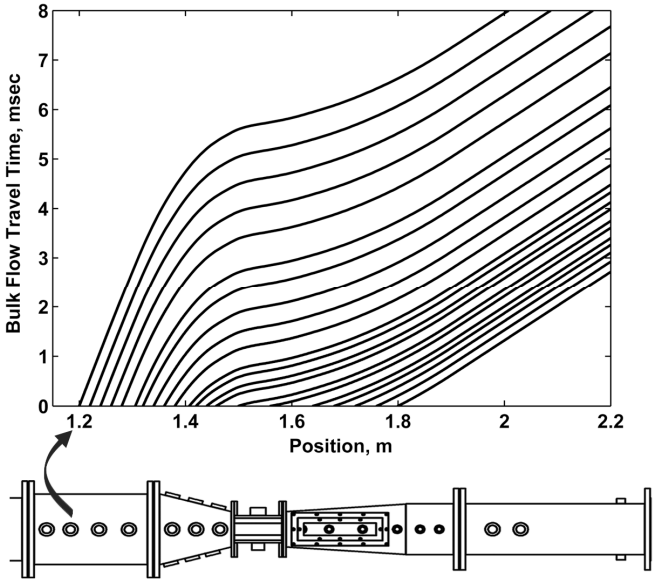

Figure 17. Gas-phase travel time starting from varying positions along the facility (profile intersection with horizontal axis) for the Case A operating point.

the flow travel time across the TS is predicted to be less than 0.5 msec.

Having estimated the bulk flow profiles, the developed model can now be used to evaluate the Jet-A evaporation, mixing and chemistry. For this example, the SMD is set to $35\mu m$ and the Jet-A injection location, x_{inj}, is set to 1.41 m, which corresponds to injection through port CV1 in Figure 6. The complete Case A operating point is then given by

$$[P_{PL},\ T_{tot},\ \Delta T_{TS},\ \dot{m}_{air},\ \phi_{vit},\ \dot{m}_{JetA},\ SMD, x_{inj\,(port)}] =$$
$$\text{Case A: } [30\,psia, 1500K, 150K, 0.22\,{}^{kg}\!/_{s}, 0.42, 2.03\,{}^{g}\!/_{s}, 35\mu m, 1.41(CV1)]$$

Figure 18 shows the predicted profile of droplet velocity for Case A together with the bulk flow velocity profile from Figure 16. The droplet velocity is initially 1.6 m/s and immediately increases due to the drag force exerted by the bulk flow on the droplet. The droplet velocity lags the bulk flow for nearly the entire droplet lifetime. This is due to the relatively large inertia of the droplets and the rapidly changing bulk flow velocity. Figure 18 shows that in the TS the droplet velocity lag can reach values upwards of 100 m/s, which causes locally high evaporation rates, as will be discussed shortly.

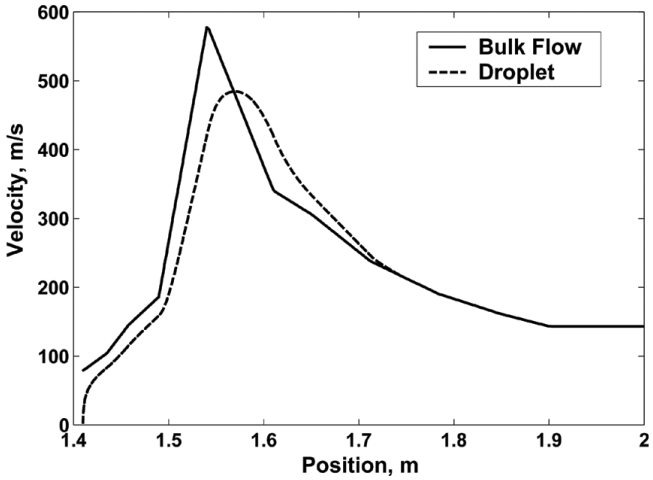

Figure 18. Predicted bulk flow velocity (solid) and predicted droplet velocity (dashed) for Case A. The injection location is 1.41m.

Figure 19 depicts the results of the Case A vaporization, mixing and chemistry analysis. The dash-dot line is the axial profile of d_{drop}^2 scaled by its initial value. It shows that, for Case A, droplet evaporation completed at about 1.76m. The variations in the d_{drop}^2 profile slope reflect the significant influence of the axial variations of bulk flow velocity and temperature on the droplet vaporization rate[5]. The set of dotted lines are the profiles of the ignition integral value, I, for every 10th fuel element (to reduce clutter). According to the definition of I in Equation (4.23), a fuel element is predicted to autoignite at the location where the corresponding ignition integral line reaches a value of one. Note that since each fuel element travels at the bulk flow velocity, the general shape of the ignition integral lines is similar to the shape of the profiles given in Figure 17. The

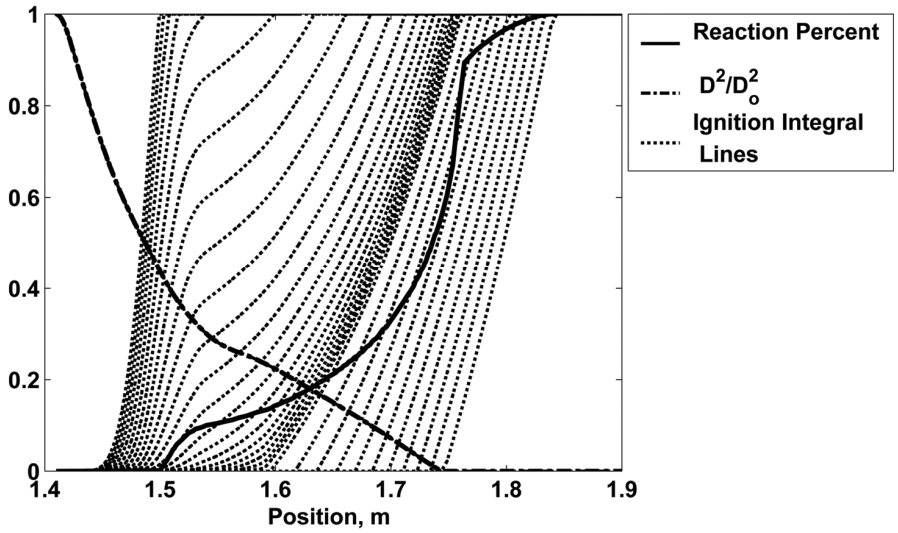

Figure 19. Case A priming process indicators: Reaction Percent Line; Normalized Droplet Diameter Squared; and Ignition Integral lines for every 10th fuel element. Fuel injection location is 1.41m.

[5] If the bulk flow temperature and pressure were constant, the d_{drop}^2 profile slope would also be constant, see the "D^2 law" description in [10].

ignition integral lines that originate just upstream of the TS outlet (1.5-1.59m) have nearly zero slopes due to the low initial temperature of those fuel elements, the mixing delay that slows the fuel element heat-up, and the locally high bulk flow velocity. As discussed in Section 4.2, τ_{mix} is discontinuously set to zero at the TS outlet (1.59 m), which sets the temperature of each fuel element equal to the bulk flow temperature. Consequently, the ignition integral lines that still have nearly zero slopes at the TS outlet will all increase sharply at the TS outlet. This results in the dense 'front' of lines observed in Figure 19. The solid line is the 'reaction percent line', which describes the percent by mass of fuel that has reached autoignition at a given location along the facility. This is computed by summing the masses of all the fuel elements that have already autoignited upstream of a given location and dividing by the total mass of fuel originally in the group of droplets. The reaction percent line begins to increase at about 1.5m. This indicates that for Case A some of the fuel elements are predicted to autoignite within the TS, located between 1.49m and 1.59m. The reaction percent line continues to increase rapidly to a value of about 0.15 when it levels off until about 1.7m. This decrease in slope is caused by the drop in temperature and increase in velocity across the TS. Between 1.7 m to 1.76 m the reaction percent line increases sharply to about 0.9, which indicates that most of the fuel is predicted to autoignite by 1.76 m. The discontinuous change in the slope of the reaction percent line at about 1.76 m is a result of the discontinuous change in τ_{mix} at the TS outlet.

The reaction percent line consolidates all of the physical processes involved in priming and autoignition. Therefore, it can be used to describe the autoignition of the fuel without the need for the d_{drop}^2 profile or the set of ignition integral profiles. Next, the

reaction percent line alone is used to compare the autoignition of fuel at varying injection locations. This will reveal trends and optimal injection locations for the PAT concept in the AF at the Case A operating point.

Figure 20 shows the reaction percent lines for Case A with different injection locations. From left to right, each reaction percent line corresponds to a downstream shift of the injection location starting from the plenum and ending at the outlet of the diverging section. The bold lines labeled I, II, III and IV categorize four different classes of reaction percent lines. The numerals at the bottom of the figure point to the injection locations of the respective reaction percent lines and the numerals at the top of the figure point to the predicted locations of complete autoignition. Line I corresponds to fuel injection in the plenum where complete autoignition occurs upstream of the TS. The line is relatively

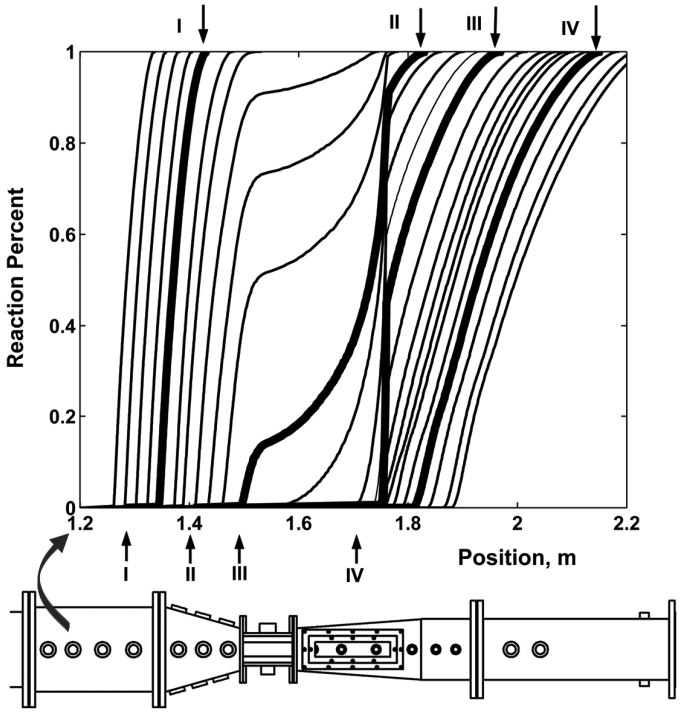

Figure 20. Reaction percent lines for Case A at various injection locations. The lines labeled I, II, III, IV represent four different classes or shapes of reaction percent lines. The top view schematic of the AF is shown with approximately the same scale as the horizontal axis.

straight because the fuel autoignites before experiencing any significant variations in the bulk flow properties. Line II, which is the same reaction percent line shown in Figure 19, is an example of an injection location where fuel autoignition begins within the TS and is completed downstream of the TS. As described above, the sharp corner in Line II at about 1.76 m is due to the discontinuous change in τ_{mix}. Line III corresponds to fuel injection upstream of the TS, at about 1.5m, and fuel autoignition only downstream of the TS. For this injection location, nearly half of the fuel evaporates before the TS outlet. However, due to the mixing delay and short fuel travel time, the fuel elements generated during that time do not autoignite until about 1.76m, where Line III jumps to about 0.5. Finally, Line IV corresponds to fuel injection and autoignition downstream of the TS. Like Line I, Line IV is relatively straight because it does not experience any significant changes in bulk flow properties.

Next, the reaction percent lines themselves are "summarized" by plotting the position of 0.05, 0.25 and 0.95 on each reaction percent line versus the corresponding injection location, yielding an 'injection/ignition' map. The injection/ignition map contains the same information as the set of reaction percent lines in Figure 20, but presents it in a more concise manner for a continuous change in injection locations.

Figure 21 shows the injection/ignition map for Case A. The reaction percent lines from Figure 20 have been mapped into points on the 5% (circle), 25% (plus), and 95% (x-mark) reaction lines. Also shown on the map are pairs of vertical and horizontal lines, which delineate the location of the TS, and a 'zero delay' line, which represents the instant ignition of all the fuel upon injection. To aid in the interpretation of the map, the injection locations have been divided into four regions. Each region demarcates injection

locations with reaction percent lines similar to Lines I, II, III, and IV in Figure 20. The first is Region I, where fuel injection and autoignition occur upstream of the TS. Here, the 5%, 25% and 95% lines are parallel because of the nearly constant bulk temperature, pressure and velocity experienced by the fuel. Next is Region II, which contains the injection locations for which some fuel elements autoignite within the TS. The slopes of the 25% and 95% lines in Region II increase significantly because of the decrease in the bulk flow temperature and pressure and the increase in the bulk flow velocity across the TS, which all increase the ignition delay time and the distance traveled by the fuel before autoignition. Next is Region III, which encompasses the injection locations upstream of the TS that result in autoignition only downstream of the TS. In the transition from

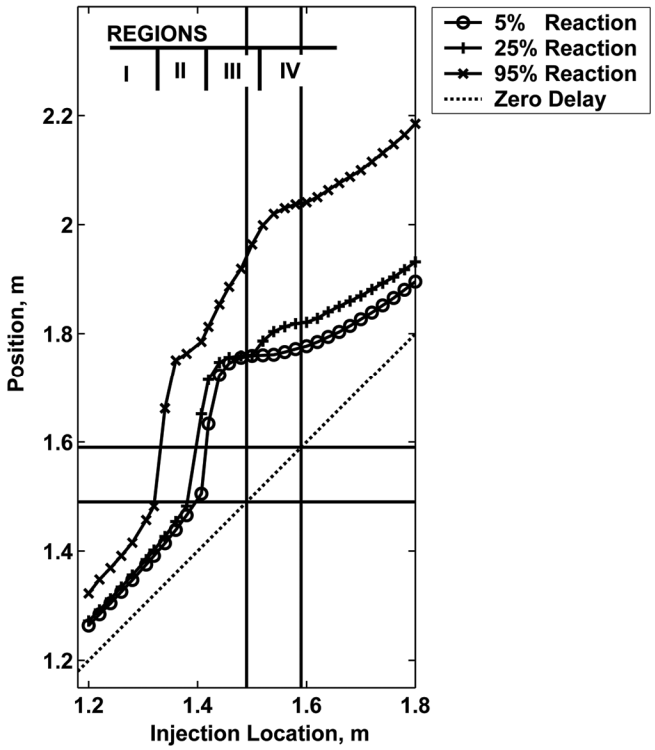

Figure 21. Injection/ignition map for Case A. The pairs of vertical and horizontal lines delineate the location of the TS. Four regions of injection locations are identified that characterize different autoignition behaviors.

Region II to Region III, the 5% line jumps to a distance of about 0.15m downstream of the TS, and then the 5% and 25% lines become nearly horizontal and close to one another for reasons discussed below. This suggests that injection anywhere within Region III will result in autoignition within a compact zone that is at a safe distance downstream of the TS and that is relatively insensitive to small changes in injection location. Therefore, injection within Region III is ideal for the PAT concept. Notably, this prediction indicates that the region just upstream of a turbine stage provides the best injection location for achieving autoignition in the afterburner. The last range of injection locations is denoted as Region IV. As in Region I, the fuel experiences nearly constant pressure, temperature and velocity. However, the 5%, 25% and 95% lines are farther apart because the velocity is higher and the temperature and pressure are lower.

Figure 22 shows the dependence of evaporation time on injection location. It clearly indicates that in Region III the evaporation time is the shortest and least sensitive to small changes in injection location. This is due to the proximity of Region III to the

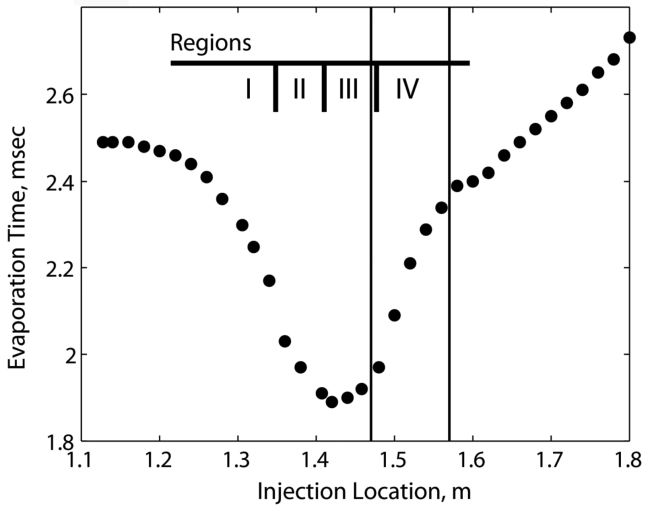

Figure 22. Droplet evaporation time for Case A operating conditions with varying injection locations. Vertical lines delineate location of the TS.

TS, where the large velocity lag between the droplets and the bulk flow leads to locally high vaporization rates. Consequently, for injection locations within Region III the fuel elements originating in the TS contain a large percent by mass of the fuel from the group of droplets. These 'neighboring' fuel elements have nearly overlapping axial ignition integral profiles and, therefore, autoignite at approximately the same location. As a result, the 5% and 25% lines in Region III of the injection/ignition map are close together and nearly horizontal.

CHAPTER 5 EXPERIMENTAL RESULTS AND COMPARISON WITH THEORETICAL PREDICTIONS

This Chapter describes the results of fuel autoignition experiments in the AF and their comparison with the developed model predictions. Note that these experiments were conducted before the AF modifications described in Section 2.2. This Chapter proceeds as follows: first, temperature and pressure measurements of autoignition are presented for two operating points of the facility; then, chemiluminescence images of autoignition taken through the quartz window are presented for three different operating points of the system.

5.1 Temperature and Pressure Measurements

For the temperature measurements, the opening for the quartz window was blocked with ceramic plates to reduce radiative losses and, thus, approximate a nearly adiabatic flow downstream of the TS. The first set of temperature measurements was obtained for the following operating point, which is referred to as Case 1 and is described using the notation introduced in the previous chapter:

$$[P_{PL},\ T_{tot},\ \Delta T_{TS},\ \dot{m}_{air},\ \phi_{vit},\ \dot{m}_{JetA},\ SMD, x_{inj}(port)] =$$

$$\text{Case 1: } [25\,psia, 1400K, 175K, 0.194\,{}^{kg}\!/_{s},\ 0.44,\ 2.26\,{}^{g}\!/_{s},\ 32\mu m, 1.46m(CV2)]$$

where CV2 refers to the port where the injector is installed, see Figure 6.

Figure 23 shows the time history of the thermocouple and plenum pressure measurements for Case 1. The traces in Figure 23 exhibit low frequency oscillations, which were caused by pressure variations in the methane supply system. Injection of the afterburner fuel takes place at approximately 1270 sec. Prior to this instant, there is an

approximately 175K temperature difference between the CL thermocouple and the thermocouples downstream of the TS. This temperature drop is caused by the blade cooling and water injection in the TS. Subsequent to the afterburner fuel injection, the measured temperatures downstream of the TS increase monotonically due to the fuel autoignition until the system reaches thermal equilibrium. Figure 23 shows that the CL thermocouple and the plenum pressure are not affected by the fuel injection, indicating that little or no heat release takes place upstream of the TS throat. Downstream of the TS, the first thermocouple, D3, reaches an average temperature of 1263K and the last thermocouple, AB2, reaches an average temperature of 1468K. The thermocouples between D3 and AB2 measure successively higher temperatures. The data in Figure 23

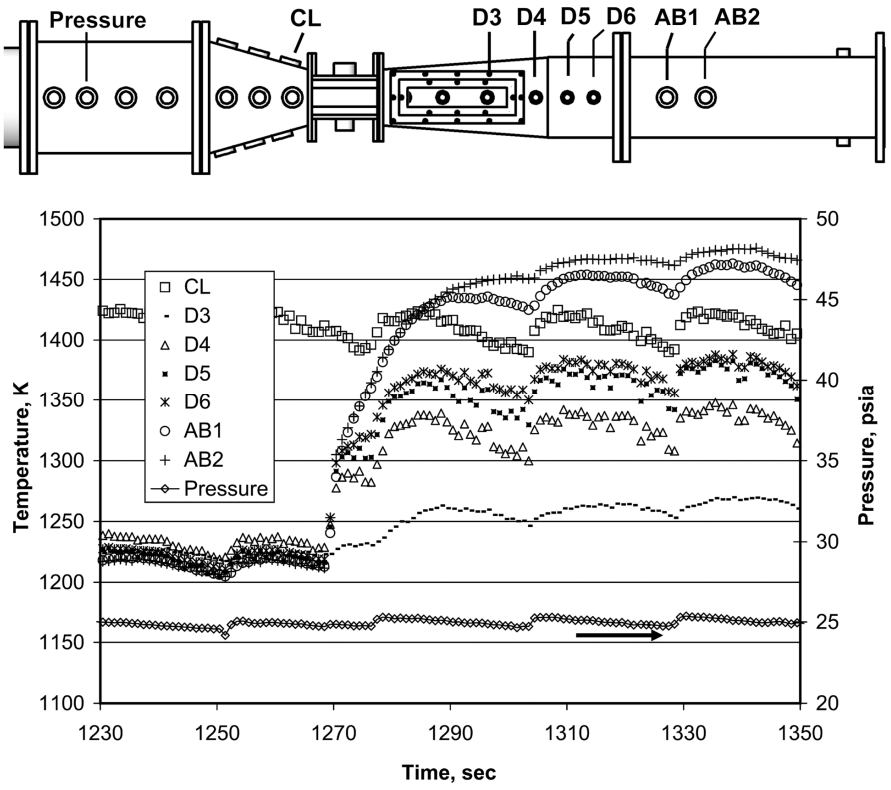

Figure 23. Thermocouple and pressure transducer data for Case 1.

demonstrate that Jet-A can autoignite and continue burning without a bluff-body flameholder or a trigger mechanism. Moreover, the ignition delay time is sufficiently long to allow fuel injected upstream of the TS to autoignite only downstream of the TS, which is an essential part of the PAT concept.

To correlate the temperature measurements with the developed model predictions, the measured temperature increase was normalized by the expected temperature increase due to complete combustion of the fuel. In the discussed case, complete combustion would result in a temperature increase of 354K. The results of this normalization are shown in Figure 24. The temperature measured by the last thermocouple, AB2, equals about 72% of the expected maximum temperature rise. It is not known if additional heat release occurred downstream of AB2. The normalized temperature can be compared to the reaction percent line predicted by the model, which is also shown in Figure 24. Although, by definition, the reaction percent line does not exactly correspond to the normalized temperature increase from the autoignition process, it is assumed to give a

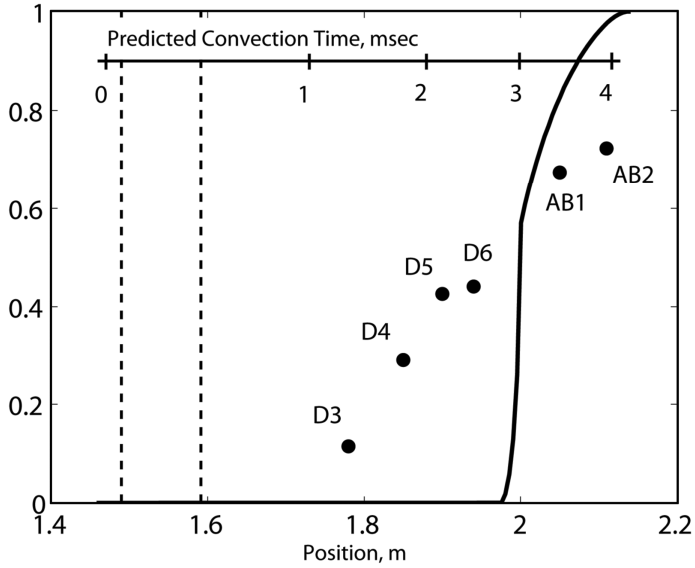

Figure 24. Case 1 normalized temperature increase (circles) and theoretical reaction percent line (solid). Dashed vertical lines delineate the TS.

good approximation, especially at the onset of combustion. The comparison of the reaction percent line with the normalized temperature measurements shows that the predicted autoignition location lies within the region of measured temperature increase. The model predicts, however, that autoignition abruptly occurs at about 2 m, whereas the thermocouple measurements show a gradual temperature increase that begins at approximately 1.75 m. Figure 24 also shows a scale of the predicted bulk flow travel time from the injector discharge. It indicates that the location of the first and last downstream thermocouples, D3 and AB2, correspond to convection times of about 1.3 msec and 3.9 msec, respectively. Taking D3 as the location of autoignition, the model over-predicts the ignition delay time by about 1.5 msec.

Figure 25 shows the predicted injection/ignition map for the operating conditions of Case 1 with varying injection locations. In addition to the reaction percent lines discussed in the previous section, Figure 25 also includes a line marking the predicted location of complete droplet evaporation (solid, diamond). The actual injection location for Case 1 is represented by the bold vertical line. Figure 25 indicates that the injection location for Case 1 lies within the injection range that yields a relatively compact combustion zone downstream of the TS. This range of injection locations corresponds to Region III in Figure 21, which was identified as the optimal region for the PAT concept. The map also shows that the injector could have been moved upstream to a location of about 1.4 m while still keeping the afterburner fuel combustion downstream of the TS. The line representing the droplet lifetime shows that the predicted location of complete droplet evaporation for Case 1 occurs at about 1.81 m, which is just slightly downstream of the D3 thermocouple. Referring to Figure 24, this indicates that the predicted location

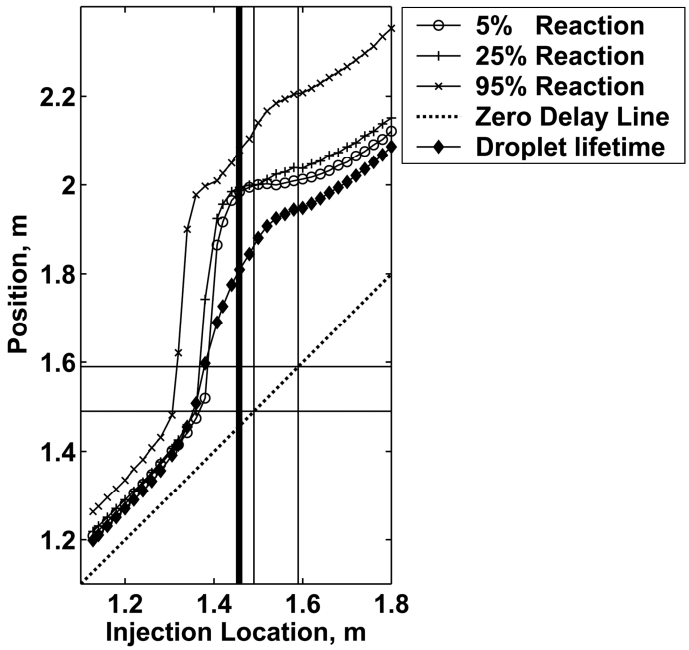

Figure 25. Injection/ignition map for Case 1. Thick vertical line extends from the fuel injection location at 1.46m.

of complete droplet evaporation occurs upstream of both the predicted and measured position of significant heat release.

Next, another operating point was analyzed in which the primary combustion (methane/air) is slightly richer and the afterburner fuel is injected farther upstream. This operating point, referred to as Case 2, is given by the following parameters:

$$[P_{PL},\ T_{tot},\ \Delta T_{TS},\ \dot{m}_{air},\ \phi_{vit},\ \dot{m}_{JetA},\ SMD, x_{inj}(port)] =$$
$$\text{Case 2: } [28 psia, 1425K, 200K, 0.197\,{}^{kg}\!/_{s},\ 0.475,\ 2.26\,{}^{g}\!/_{s},\ 38\mu m, 1.3m(PL4)]$$

Figure 26 shows the time history of the thermocouple measurements for Case 2. During this test, thermocouples D2 and AB2 developed a bias that is evident prior to 440 sec by the shift with respect to the other downstream thermocouples. The data from the D2 and AB2 thermocouples were used after subtracting this bias. Jet-A for afterburner combustion was injected at approximately 440 sec. In marked contrast with Case 1, the

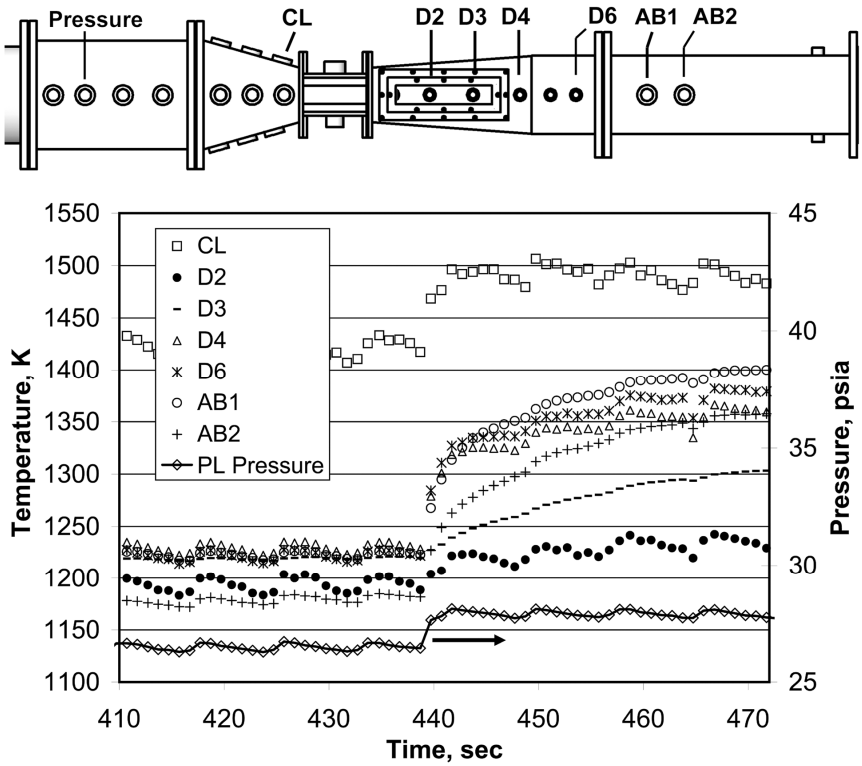

Figure 26. Thermocouple and pressure transducer measurements for Case 2.

autoignition of the fuel was accompanied by an increase in both the CL thermocouple temperature and the plenum pressure. This indicates that significant heat release from fuel autoignition occurred upstream of the TS throat. Also, temperatures measured downstream of the TS continued to increase, reaching approximately 1400K at AB1. The data in Figure 26 demonstrate a case that does not fulfill the PAT concept requirements, because significant heat release occurred upstream of the TS. In other words, the injection location was too far upstream of the TS for Case 2 operating conditions.

Figure 27 shows the normalized temperature increase for Case 2 together with the predicted reaction percent line and convection time. Also shown is the reaction percent line for an injection location of 1.38 m, which is slightly downstream of the nominal injection location. As expected, the PL3 thermocouple, which is upstream of the injection

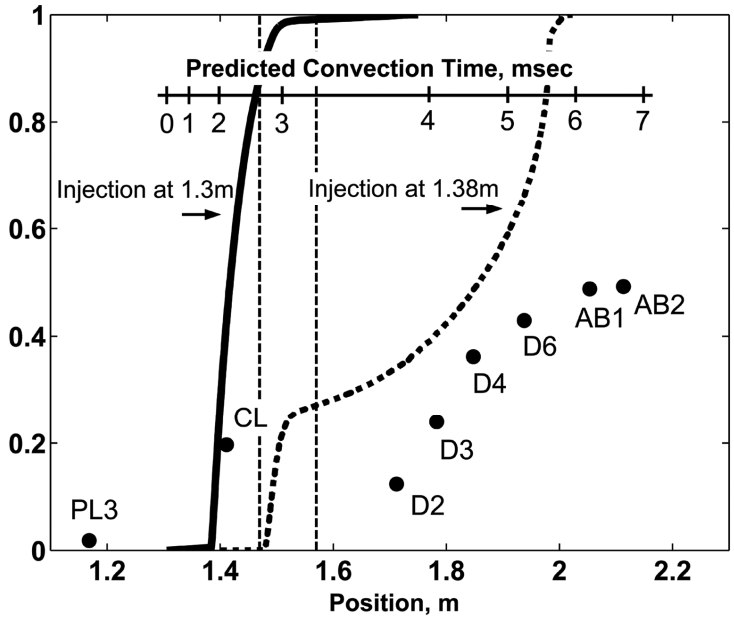

Figure 27. Case 2 normalized temperature increase (circles), reaction percent line for injection at 1.3m (bold, solid line), and reaction percent line for injection at 1.38m (bold, dashed line). Dashed vertical lines delineate the TS.

location, does not measure a temperature increase. In contrast, the CL thermocouple, which is upstream of the TS but downstream of the injection location, measures a 20% normalized temperature increase. This heat addition between the injector and the CL thermocouple is responsible for the pressure increase measured in the plenum. The normalized temperature increase approximately levels off between the CL and D3 thermocouples and then continues to increase up to 49% at the AB2 thermocouple. This trend is not predicted by the model for the nominal injection location at 1.3m, as indicated by the corresponding reaction percent line. Although the model predicts that combustion will begin in the converging section, as indeed occurred, the model also predicts that combustion is completed upstream of the TS outlet, which is obviously not the case. This discrepancy may be resolved by examining the injection/ignition map for Case 2 operating conditions, given in Figure 28. The map shows that the vertical bold

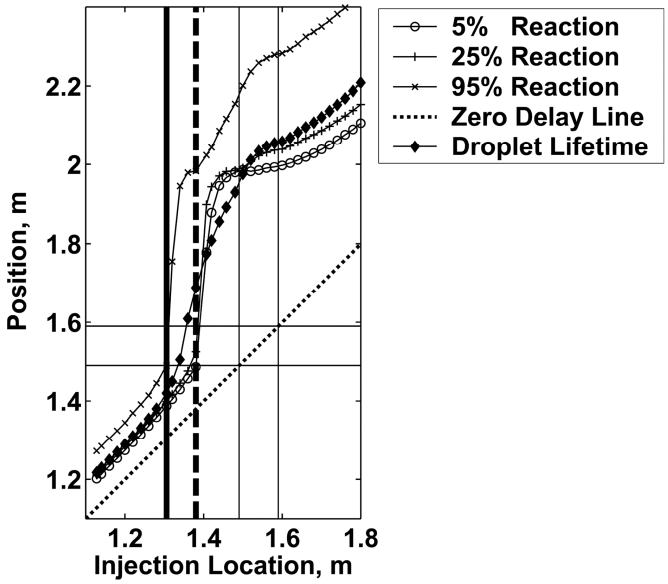

Figure 28. Injection/Ignition map for Case 2. Thick vertical lines extend from injection locations at 1.3m (solid) and 1.38m (dashed).

line for the nominal injection location is in close vicinity to the steep portion of the reaction percent lines where autoignition occurs both upstream and downstream of the TS (Region II in Figure 21). The model predictions in this injection location range are in better agreement with the thermocouple measurements. To illustrate this, the reaction percent line for an injection location of 1.38m, indicated by the vertical dashed line, was plotted in Figure 27. It shows that the 1.38 m profile does exhibit the trends of the thermocouple measurements including the leveling off between the CL and D3 thermocouples. Thus, for Case 2, small changes in the operating point parameters can result in a reaction percent line that is in much closer agreement with the measurements.

5.2 Chemiluminescence Measurements

Chemiluminescence images were recorded through the quartz window in the diverging section, which had been blocked during the temperature measurements. The

following three cases, listed in order of increasing primary combustor equivalence ratio, were studied:

$$[P_{PL},\ T_{tot},\ \Delta T_{TS},\ \dot{m}_{air},\ \phi_{vit},\ \dot{m}_{JetA},\ SMD, x_{inj}(port)] =$$

Case 3: $[37.5\,psia, 1315K, 115K, 0.275\,{}^{kg}/_{s}, 0.40, 2.03\,{}^{g}/_{s}, 45\mu m, 1.41m(CV1)]$

Case 4: $[38.3\,psia, 1350K, 130K, 0.273\,{}^{kg}/_{s}, 0.43, 2.03\,{}^{g}/_{s}, 45\mu m, 1.41m(CV1)]$

Case 5: $[38.5\,psia, 1475K, 155K, 0.260\,{}^{kg}/_{s}, 0.51, 2.03\,{}^{g}/_{s}, 44\mu m, 1.41m(CV1)]$

These tests had higher flow rates than the previously discussed cases, resulting in higher plenum pressures and choked flow at the throat between the TS blades.

Figure 29 presents the recorded chemiluminescence images, intensity plots, and predicted injection/ignition maps for Cases 3-5. The chemiluminescence images recorded by the CCD camera have been converted to grayscale and further processed to enhance their quality. Intensity plots are shown below each chemiluminescence image. They were obtained by taking averages of the grayscale image intensities - 0 (black) to 255 (white)- across the span of the diverging section window (top to bottom in Figure 6).

The chemiluminescence images in Figure 29 clearly indicate that autoignition of the fuel shifts upstream from Case 3 to Case 5. Specifically, the intensity plots show that chemiluminescence starts at approximately 1.750 m, 1.715 m and 1.655 m for Cases 3, 4 and 5, respectively. This is expected in view of the increasing bulk flow temperature between these cases. The intensity profiles level-off or decrease toward the end of the window. If this is a real effect, it would imply that the reactions begin to weaken toward the end of the window. However, it is more likely that this is an artifact of the image processing.

Figure 29 also includes the predicted injection/ignition maps for each case. On each map, the thick vertical line represents the 1.41 m injection location and the large

circles are reference points that correspond to the large circles on the intensity profiles. Note that the reference point locations were chosen simply to help locate the measured intensity profile on the map. In Figure 29(a), the reference point on the injection/ignition map is well below the 5% reaction line. This indicates that the model over-predicts the autoignition location for Case 3, because the corresponding point on the intensity profile is at a location where the measured chemiluminescence intensity was greater than zero. Following the same procedure with Figure 29(b), it is observed that the model also over-predicts the ignition location for Case 4, although to a lesser extent. In contrast, Figure 29(c) shows that for Case 5 there is good agreement between the model and the measurements. This comparison between the injection/ignition maps and the chemiluminescence measurements reaffirms that the model is able to predict the shift in the autoignition location due to changing operating conditions and suggests that the accuracy of the current model increases as the actual ignition delay decreases.

5.3 Summary of AF Prime Stage Experiments

The results of the AF experiments described in this Chapter confirmed that the prime stage is feasible. Specifically, the results showed that fuel can be injected upstream of the TS and mostly react downstream of the TS. This is possible as long as the Jet-A injection location and spray characteristics are within certain ranges that depend on the operating point of the facility. It should be noted that the experiments also confirmed that the autoignition process is sustained and repeatable. That is, the autoignition combustion zone did not extinguish until the fuel valve was shut and then could be re-established at the same location when the Jet-A valve was opened again.

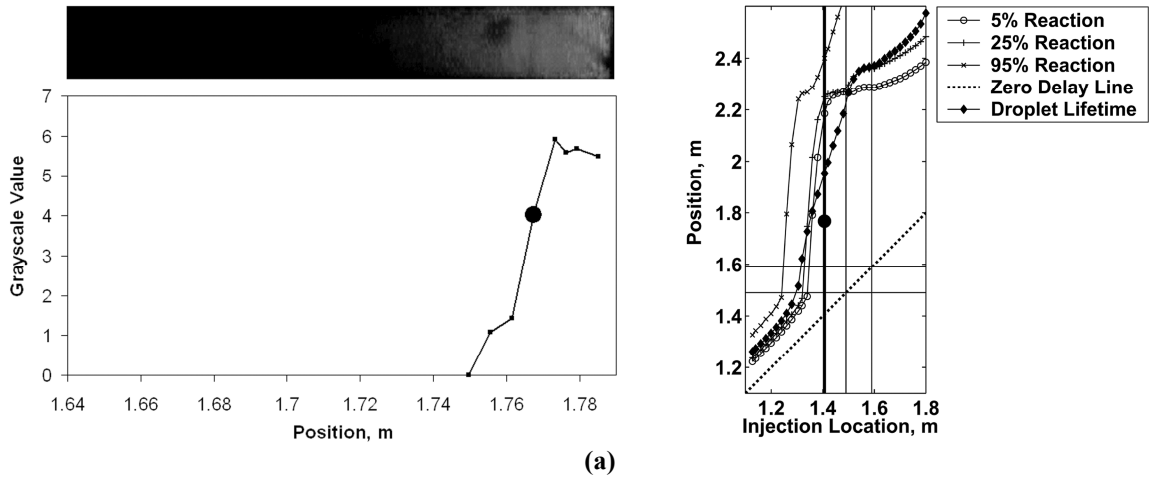

(a)

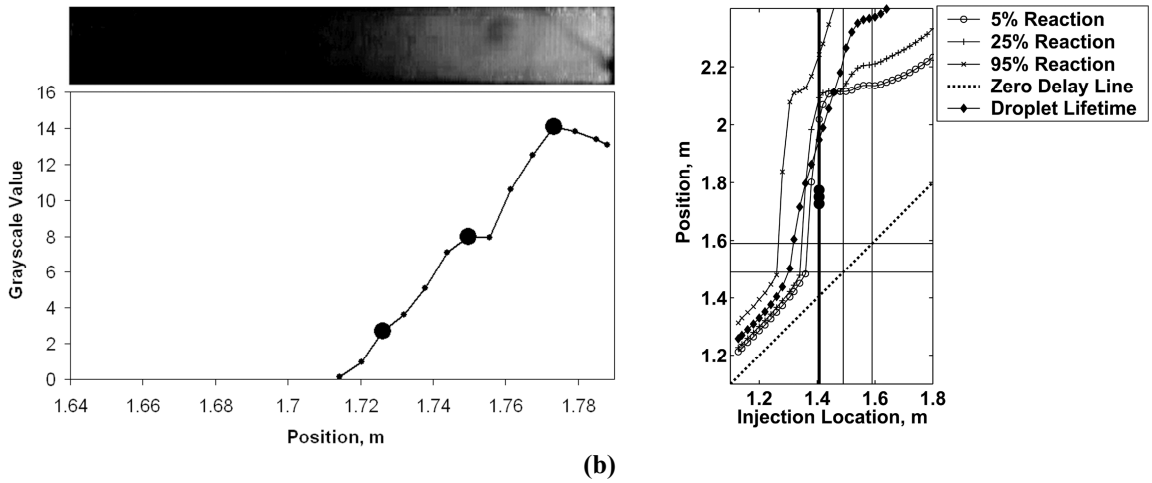

(b)

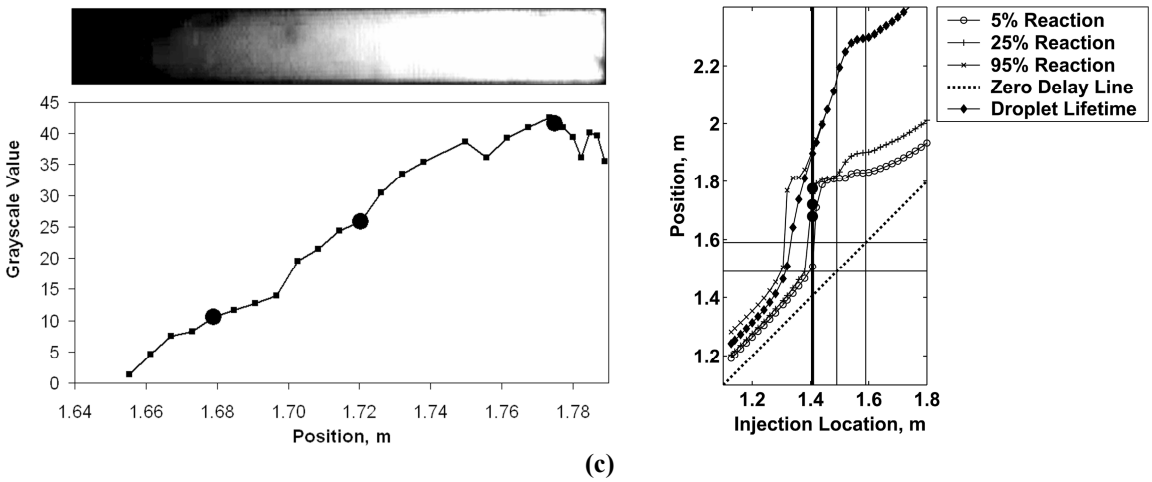

(c)

Figure 29. Chemiluminescence images, intensity profiles, and predicted injection/ignition maps for (a) Case 3, (b) Case 4, and (c) Case 5.

CHAPTER 6 FUEL PRIMING AND AUTOIGNITION AT HIGH OPERATING PRESSURE

Turbine engines can operate at pressures upwards of about 30 atm in the primary combustor and 6 atm in the afterburner [1]; however, the AF is limited to near atmospheric operating pressures. Therefore, this study investigated the feasibility of the PAT concept at higher turbine pressures using only the developed theoretical model. This effort consisted of two steps: first, the pressure dependence of the evaporation sub-model was studied using several single-droplet evaporation scenarios; and second, the developed model was applied to several hypothetical, elevated pressure AF operating points.

The evaporation sub-model pressure dependence was studied to help interpret the results from the developed model when applied to a high pressure AF operating point. The mixing and chemistry sub-models were not studied individually, because their pressure dependence is clearly indicated. The mixing sub-model does not directly depend on pressure and the chemistry sub-model has a simple inverse pressure dependence defined in Equation (4.26). The evaporation sub-model, on the other hand, has a more subtle pressure dependence, because it includes several pressure-dependent terms.

6.1 Pressure Dependence of the Evaporation Sub-Model

The pressure dependence of the evaporation sub-model was studied by applying it to a single Jet-A droplet in high-temperature vitiated-air. First, an analysis was conducted at constant high and low bulk pressures to reveal the general pressure dependence. Then, an analysis was conducted with a transient decrease in bulk pressure during the droplet

lifetime. This simulates the pressure drop that droplets would experience when they pass through the turbine stages of an engine.

6.2 Evaporation at Constant Pressure

The evaporation sub-model was applied to a single Jet-A droplet in high temperature, vitiated-air with constant bulk pressures of 1 atm and 20 atm. The vitiated-air consisted of the products of methane/air combustion at $\phi = 0.45$ and had the following composition:

$$\left[\chi_{O_2},\ \chi_{N_2},\ \chi_{H_2O},\ \chi_{CO_2}\right] = \left[0.11,\ 0.75,\ 0.09, 0.05\right]$$

The vitiated-air temperature was set to 1200K, the initial droplet diameter was $50\mu m$, and the velocity lag was zero.

Figure 30 shows the time dependence of the droplet diameter squared and the heat transfer to the liquid phase scaled by their original values. Figure 31 shows the time

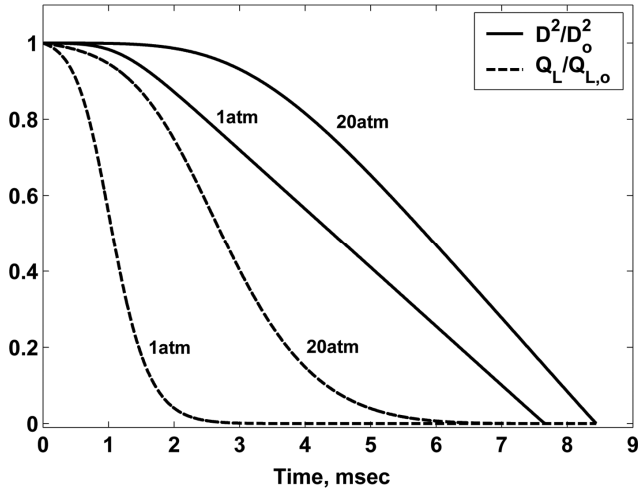

Figure 30. Scaled droplet diameter squared (solid) and scaled heat transfer to the liquid phase (dash) for a 50µm diameter droplet in stagnant vitiated air. Ambient temperature is 1200K. Ambient pressure is 1atm and 20atm, as indicated.

dependence of T_{drop} and the boiling temperature, T_{boil}, which was calculated using the expression for $P_{F,s}$ (see Appendix A) by setting $P_{F,s}$ equal to P_{bulk} and solving for temperature. The expression for T_{boil} is as follows:

$$T_{boil} = \frac{5141.36}{11.495 - \ln\left(P_{bulk}/101325\right)} \tag{6.1}$$

Figure 30 shows that the droplet evaporates in 7.66 msec when $P = 1$ atm and 8.45 msec when $P = 20$ atm. This relatively small change in evaporation time for the 20x pressure increase indicates that the evaporation time has a weak pressure dependence at the considered ambient temperature and composition. At both pressures, the slope of the D^2/D_o^2 profile is initially zero and starts to decrease only after $Q_L/\dot{Q}_{L,o}$ drops nearly to zero. The time elapsed until $Q_L/\dot{Q}_{L,o}$ drops to zero is termed the heat-up time (HUT). During the HUT, little evaporation takes place because most of the energy transferred to the droplet is used to heat it up. This is described by the T_{drop} profiles in Figure 31. Note that T_{drop} for the 1 and 20 atm cases reach steady state temperatures, T_{SS}, of 412K and

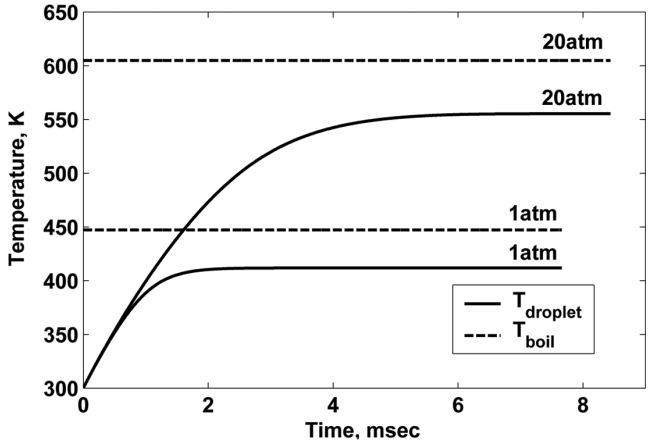

Figure 31. Droplet temperature (solid) and fuel boiling point (dashed) for a 50µm diameter droplet in an bulk medium of vitiated air at 1200K. Ambient pressures are 1atm and 20atm, as indicated.

555K, respectively, when $Q_L/\dot{Q}_{L,o}$ profiles drop nearly to zero. If HUT is defined as the time at which $Q_L/\dot{Q}_{L,o}$ decreases to 10%, which approximately corresponds to the time when T_{drop} reaches T_{SS} for either pressure, then the HUT is 1.8 msec for the 1 atm case and 4.5 msec for the 20 atm case. This indicates that the HUT has a much stronger pressure dependence than the total evaporation time.

Figure 32 describes the dependence of T_{boil} and T_{SS} on P_{bulk} and T_{bulk}. The profiles of T_{SS} are shown for T_{bulk} of 1000K, 1200K, 1400K and 1600K. They show that T_{SS} increases slightly with T_{bulk} and that its dependence on T_{bulk} is weak compared to its dependence on P_{bulk}. The margin (temperature difference) between T_{boil} and T_{SS} decreases slightly with a decrease in P_{bulk} and an increase in T_{bulk}. As discussed in the next section, this margin has an important role when P_{bulk} decreases during the lifetime of the droplet.

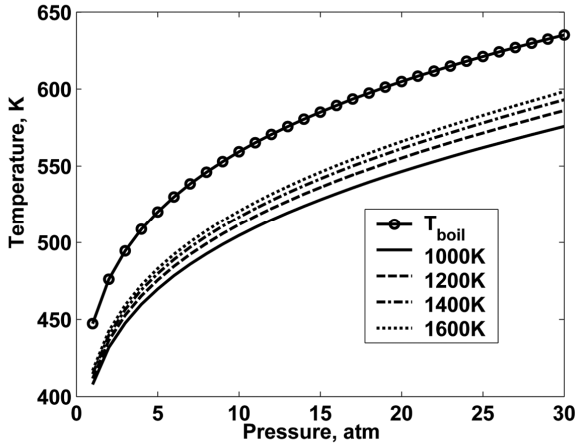

Figure 32. Pressure dependence of fuel boiling point and steady state temperature. Four profiles of steady state temperature are shown for various bulk temperatures.

It is important to identify the physical mechanisms responsible for the P_{bulk} and T_{bulk} dependence of HUT, T_{SS} and the total evaporation time. This will help to understand the effects of transient pressure discussed in the next section. Figure 33 illustrates the major physical processes involved in the evaporation sub-model. The large, hollow arrows indicate the flow of energy and the gray squares identify the T_{drop}-dependent terms. Energy from the high temperature ambient environment is transferred to the droplet through conduction (or convection, if there is a velocity lag between the droplet and the bulk flow) at a rate that is proportional to $(T_{bulk} - T_{drop})$. The energy transferred to the droplet could be used to raise T_{drop} or to vaporize the fuel by providing the necessary heat of vaporization, Δh_{vap}. Fuel that vaporizes from the droplet is transported away by diffusion, which is driven by the radial gradient of fuel mole fraction at the droplet surface, $\nabla_r \chi_{F,s}$. Importantly, $\nabla_r \chi_{F,s}$ and $\chi_{F,s}$ are a function of both T_{drop}

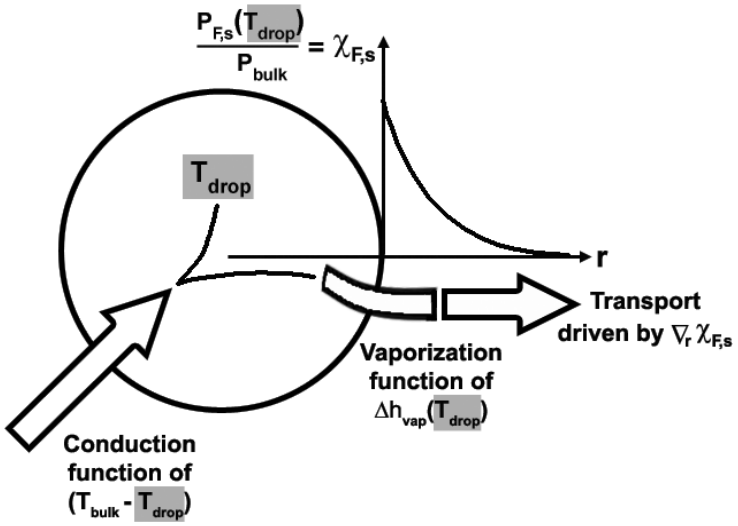

Figure 33. The major physical processes involved in the evaporation sub-model. Conduction transfers heat into the droplet. Some of the heat is used to raise the droplet temperature and some is used to vaporize fuel. The vaporized fuel diffuses away from the droplet, thus transporting energy back into the bulk environment. The axis represents the radial (r) profile of the fuel vapor mole fraction.

and P_{bulk}, whereas $P_{F,s}$ is only a function of T_{drop}.

The developed model assumes that the initial droplet temperature is 300K. At this low temperature, $P_{F,s}$, $\chi_{F,s}$ and $\nabla_r \chi_{F,s}$ are very low and, as a result, there is initially no avenue by which energy can leave the droplet. Thus, the energy transferred to the droplet is used almost exclusively to heat-up it up. As T_{drop} increases, fuel vaporizes from the droplet to establish the quasi-equilibrium value of $P_{F,s} = P_{F,s}(T_{drop})$. This produces a positive $\nabla_r \chi_{F,s}$ that initiates diffusion of fuel vapor away from the droplet. At this point, some of the energy transferred to the droplet heats it up and some vaporizes fuel and is transported back into the ambient environment. As the droplet continues to heat-up, Δh_{vap} decreases, $\nabla_r \chi_{F,s}$ increases (via $P_{F,s}$) and, thus, an increasing fraction of energy transferred to the droplet is used to vaporize fuel. Eventually, T_{drop} reaches a value where Δh_{vap} is low enough and $\nabla_r \chi_{F,s}$ is high enough so that all the energy transferred to the droplet is used to vaporize fuel. This is the droplet steady-state temperature, T_{SS}.

To explain the pressure and temperature dependences of HUT, T_{SS} and evaporation time, consider the reaction of a droplet at T_{SS} to small changes in T_{bulk} or P_{bulk}. First, if T_{bulk} is increased, then conduction of energy into the droplet increases. When this happens, $P_{F,s}$ is initially unchanged, resulting in an imbalance between the rates of energy transport into and out of the droplet, thus setting the droplet into a non-equilibrium state. The higher energy input raises T_{drop} and, thus, increases the rate at which energy can leave the droplet (via the resulting increase in $P_{F,s}$, $\chi_{F,s}$ and $\nabla_r \chi_{F,s}$).

Eventually, equilibrium is re-established at a higher T_{SS}. For this application, an increase in T_{bulk} has a relatively small effect on $(T_{bulk} - T_{drop})$, because T_{bulk} is already so much higher than T_{drop}. This is why T_{SS} has a relatively weak T_{bulk} dependence, see Figure 32. Next, if P_{bulk} increases, $\chi_{F,s}$ and $\nabla_r \chi_{F,s}$ immediately decrease in response, thus reducing the rate at which energy can leave the droplet. This, in turn, increases T_{drop} until equilibrium is reached at a higher T_{SS}. Conversely, if P_{bulk} decreases, $\nabla_r \chi_{F,s}$ increases and so does the rate at which energy can leave the droplet. In this case, the droplet cools and equilibrium is re-established at a lower T_{SS}.

For the case where P_{bulk} increases, the resulting increase in T_{SS} also results in a higher $\dot{m}_{drop}$. Figure 30 shows that the HUT is longer in the 20 atm case because T_{SS} is higher. Once the droplets reach their respective values of T_{SS}, $\dot{m}_{drop}$ is higher for the 20 atm case, as indicated by the steeper slope of the 20 atm D^2/D_o^2 profile. The higher $\dot{m}_{drop}$ at 20 atm somewhat compensates for the longer HUT so that, ultimately, there is only a small difference between the 1 atm and 20 atm total evaporation times.

6.3 Evaporation with a Large, Rapid Drop in Pressure

In the PAT concept, the afterburner fuel droplets will experience a pressure drop as they pass through the turbine stages. The magnitude and duration of this pressure drop will depend on the injection location and the operating point of the engine but would be quite large, on the scale of several atmospheres per millisecond. To examine the effect of this rapid pressure drop, consider again the droplet that has reached T_{SS} and then

experiences a decrease in P_{bulk}. As P_{bulk} decreases, $\chi_{F,s}$ increases and so does $\dot{m}_{drop}$. The higher $\dot{m}_{drop}$ transports more energy away from the droplet than is conducted into the droplet, so the droplet cools. This decrease in T_{drop} occurs at a finite rate dictated by its thermal inertia. For instance, T_{drop} of a smaller droplet will decrease in response to the decrease in P_{bulk} more rapidly than T_{drop} of a larger droplet. Because of the finite response time of T_{drop}, a significantly large and rapid pressure drop could cause P_{bulk} to decrease below $P_{F,s} = P_{F,s}(T_{drop})$. Since T_{boil} is the temperature at which $P_{bulk} = P_{F,s}$, an equivalent statement is that T_{boil} could decrease below T_{drop}. At this condition, bubble nucleation and growth occur inside the droplet and ultimately cause it to break-up into many smaller droplets and vapor – a process referred to as flash boiling [23].

A provision for flash-boiling was added to the evaporation sub-model. It was assumed that flash boiling occurs instantaneously and that the resulting droplets are so small that they evaporate instantaneously. Specifically, if P_{bulk} drops below $P_{F,s}$ or, equivalently, if T_{boil} drops below T_{drop}, the evaporation sub-model sets the droplet diameter to zero and assigns its mass to a single, newly-created fuel element.

The effect of transient pressure on droplet evaporation was demonstrated using the evaporation sub-model with imposed bulk pressure gradients. For this analysis, the initial diameter and temperature of the Jet-A droplet was $100\mu m$ and $300K$, respectively. The ambient environment was vitiated-air (products of methane/air at ϕ=0.45) at a temperature of 1200K and an initial pressure of 20 atm. Again, the relative velocity between the droplet and the vitiated air was zero. Pressure gradients of -1, -2

and $-3\,{}^{atm}\!/_{m\sec}$ were imposed when the droplet diameter reduced to 0.95 of its original value. This gave the droplet some time to heat up to a temperature closer to T_{boil} before the pressure gradient was imposed. Note that the pressure gradient was expressed in units of atmospheres per millisecond to emphasize the order of magnitude of the pressure drop and the time scales over which it occurred.

Figure 34 shows the time dependence of T_{drop} and T_{boil} for various pressure gradients. The droplet is initially at 300K and heats up at constant pressure until about 13 msec, when $D = 0.95D_o$. For the trivial case of a zero pressure gradient, the droplet continues to heat up until it reaches T_{SS} and T_{boil} remains constant. For this trivial case, the simulation shows that the droplet fully evaporates after approximately 34 msec. For the $-1\,{}^{atm}\!/_{m\sec}$ pressure gradient, the droplet cools rapidly enough in response to the pressure gradient so that it evaporates before T_{boil} falls below T_{drop}. It should be noted that, in this case, the droplet lifetime is slightly shorter than the zero pressure gradient

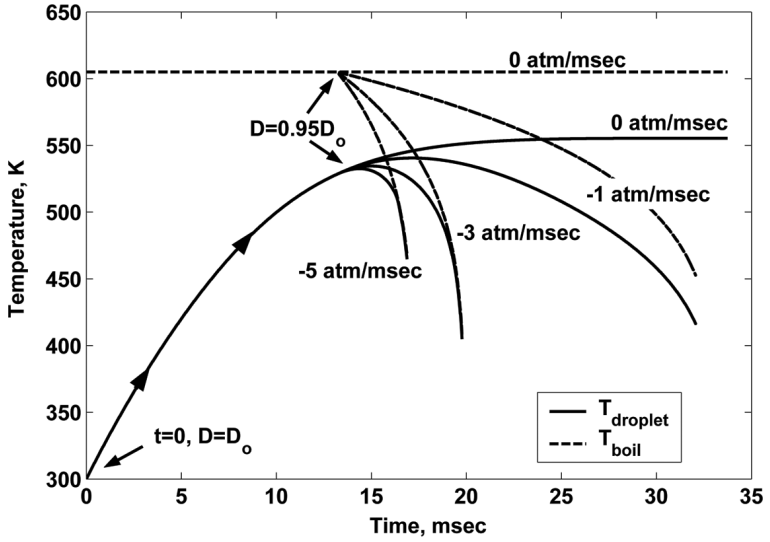

Figure 34. Profiles of boiling temperature and droplet temperature for a 100µm diameter droplet in 1200K vitiated air. Various bulk pressure gradients are imposed when the droplet diameter reduces to 0.95 of its original diameter.

case. As noted above, the decrease in pressure is accompanied by a momentary increase in $\dot{m}_{drop}$ that causes the droplet to cool to the new T_{SS}, i.e., the droplet is momentarily in a non-equilibrium state. In the $-1\,{}^{atm}/_{m\sec}$ case, the pressure gradient maintains the droplet in the non-equilibrium state. As a result, $\dot{m}_{drop}$ remains slightly higher than in the $0\,{}^{atm}/_{m\sec}$ case and the total evaporation time is shorter. For the $-2\,{}^{atm}/_{m\sec}$, and $-3\,{}^{atm}/_{m\sec}$ cases, the profiles of T_{boil} intersects with T_{drop}, and the droplet experiences flash boiling.

Figure 35 shows the state trajectories of the droplet on a temperature-pressure diagram. This alternate depiction of the information in Figure 34 provides a thermodynamic perspective of droplet evaporation with a transient pressure gradient. The T_{SS} profile is the same as in Figure 32 for the case of $T_{bulk} = 1200K$. The solid lines are state trajectories of the droplet experiencing various pressure gradients. During the initial heat up at constant pressure, all trajectories increase up to the point when $D = 0.95D_o$. For the trivial zero pressure gradient, the line continues to increase until it reaches the T_{SS}

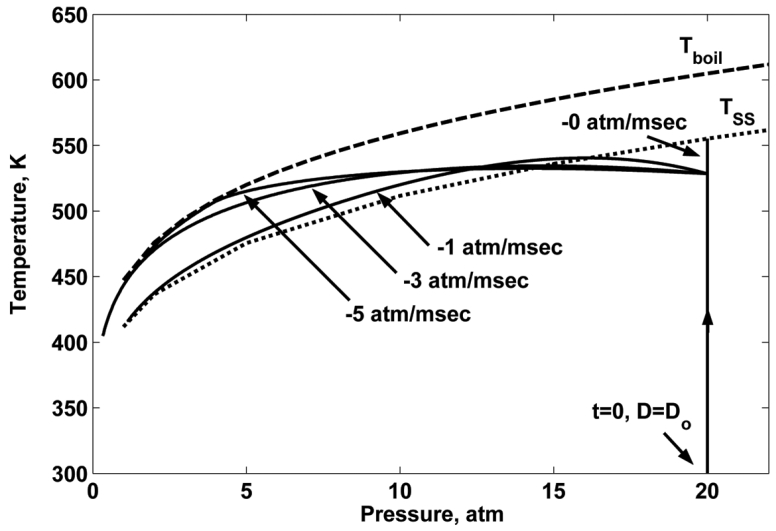

Figure 35. State trajectories of a 100μm diameter droplet in 1200K vitiated air. Various bulk pressure gradients are imposed when the droplet diameter reaches 0.95 of its original diameter.

profile. In the presence of pressure gradients, the droplet state lines move sharply to the left as pressure decreases and develop a downward slope as the droplet cools. Flash boiling occurs if the droplet state trajectories intersect the T_{boil} curve. As previously discussed, for the $-1\,{}^{atm}/_{m\sec}$ pressure gradient the droplet response is fast enough (or the pressure gradient low enough) to prevent intersection of the droplet trajectory with the T_{boil} curve. The two profiles remains very close but the droplet trajectory is always slightly higher than T_{SS}, which indicates that the droplet is always slightly out of equilibrium. For the $-3\,{}^{atm}/_{m\sec}$ and $-5\,{}^{atm}/_{m\sec}$ cases, the droplet state line intersects with the T_{boil} profile, so flash boiling occurs. An important observation from Figure 35 is that the margin between T_{boil} and T_{SS} gives the droplet some time to react to the change in pressure before it encounters the flash-boiling condition.

6.4 Application of the Theoretical Model to High Pressure Operating Conditions

Having identified the effects of high and transient pressure and added a provision for flash boiling into the theoretical model, the next step was to apply the developed model to a hypothetical high pressure AF operating point and to compare the results with those from a low pressure operating point. The operating points for the low and high operating conditions were as follows:

$$[P_{PL},\ T_{tot},\ \Delta T_{TS},\ \dot{m}_{air},\ \phi_{vit},\ \dot{m}_{JetA},\ SMD] =$$

Low Pressure: $[25\,psia, 1400K, 175K,\ 0.2\,kg/s,\ 0.45,\ 2.26\,g/s,\ 32\mu m]$

High Pressure: $[295\,psia, 1400K, 175K,\ 2.85\,kg/s,\ 0.45,\ 33.2\,g/s,\ 32\mu m]$

The injection location is excluded from the operating points because results are discussed for the full injection range. In the high pressure case, the pressures upstream and

downstream of the TS were set to 295 psia (20 atm) and 103 psia (7 atm), respectively. The upstream pressure of 20 atm is in the middle of the range of turbine engine main combustor pressures listed in [1] and the pressure downstream of the TS is slightly higher than the maximum listed in [1] for afterburners. The air and fuel flow rates were scaled by the ratio of the two P_{PL} values in order to keep velocities upstream of TS approximately the same. Note that the low pressure case is approximately the same as Case 1 in Section 5.1.

Figure 36 shows the injection/ignition maps for the low and high pressure cases. A fourth curve representing the location of complete droplet evaporation (solid, diamond) was added to the maps. Comparing the two cases reveals that for the high pressure case the autoignition of the fuel is predicted to shift upstream for all injection locations. However, the injection locations upstream of the TS that result in autoignition only downstream of the TS (Region III) are the same. This suggests that fuel priming and

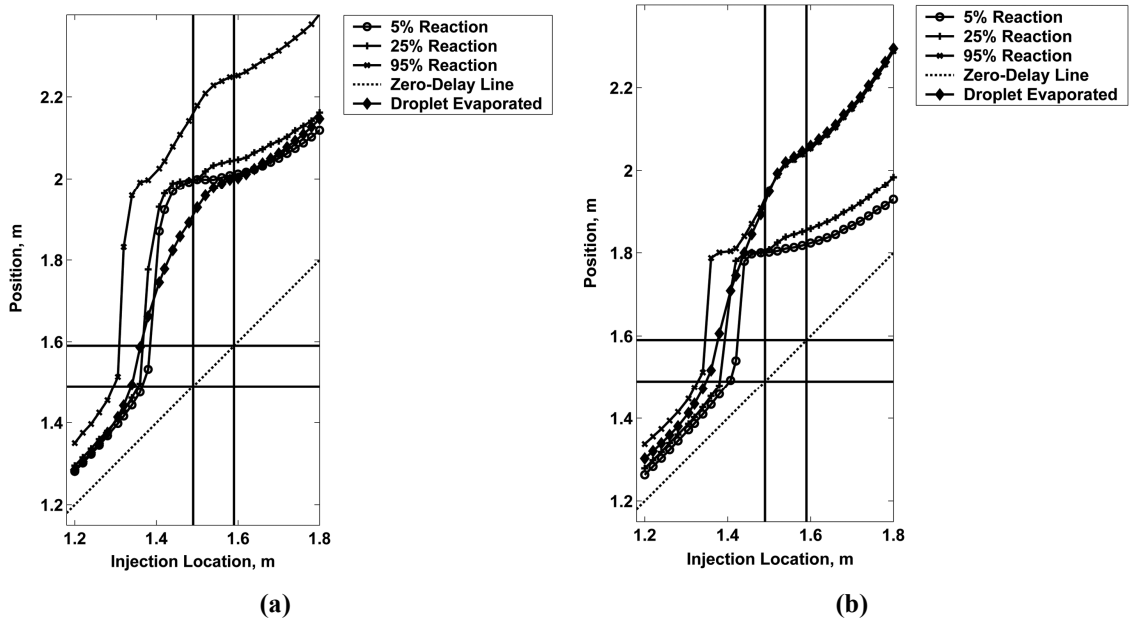

Figure 36. Injection/Ignition maps including the line for location of complete droplet evaporation for (a) the low pressure case and (b) the high pressure case

autoignition is still feasible with higher axial bulk flow pressures and, in addition, can be achieved more compactly.

Next, the high pressure case was slightly modified to produce flash boiling by increasing the values of T_{tot} and SMD. T_{tot} was increased to 1500K to reduce the droplet HUT and increase its T_{SS}, which decreases the 'safety margin' between T_{drop} and T_{boil}. The SMD was increased to $90\mu m$ to increase the droplet thermal response time. The operating point for this case is given by:

$$[P_{PL},\ T_{tot},\ \Delta T_{TS},\ \dot{m}_{air},\ \phi_{vit},\ \dot{m}_{JetA},\ SMD] =$$
$$\text{Flash Boiling: } [295\,psia, 1500K, 175K, 2.85\,kg/s, .44, 33.2\,g/s, 90\mu m]$$

where, again, the injection location is omitted because results are shown for the full injection range.

Figure 37 and Figure 38 show the results from the analysis of the flash boiling case. Figure 37 shows the injection/ignition map. The scale of this map is stretched to fit the 95% reaction and droplet evaporation lines, which are far above the 5% and 25%

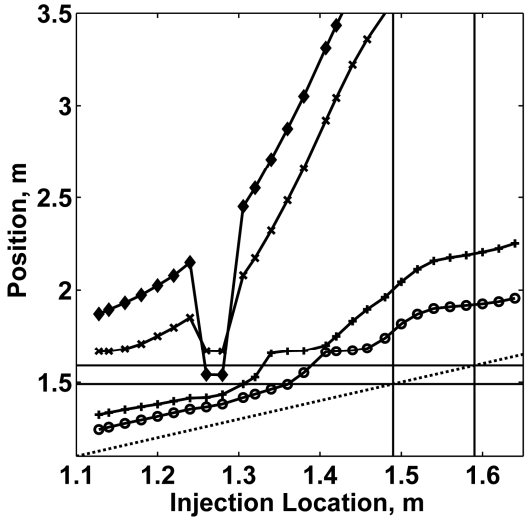

Figure 37. Injection/Ignition map for the flash boiling case including the line for location of complete droplet evaporation.

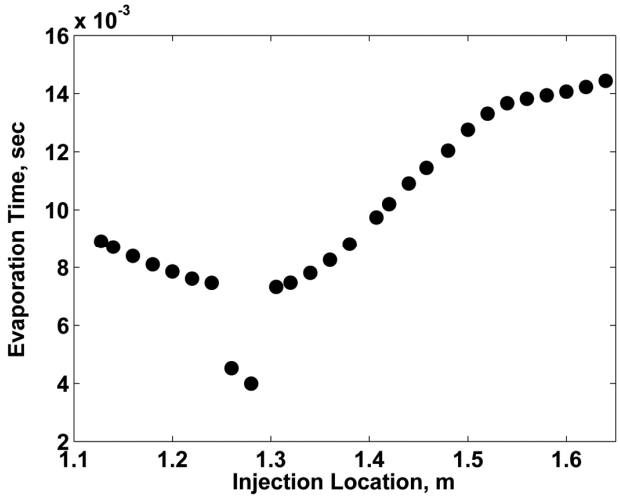

Figure 38. Droplet evaporation time for the flash boiling case.

reaction lines because of the large SMD. Figure 37 shows that flash boiling occurs between 1.26m and 1.28m, as indicated by the sharp upstream shift in the 95% reaction line and the droplet evaporation line. Flash boiling is also clearly indicated in Figure 38 by the approximately 50% drop in evaporation time between 1.26 m and 1.28 m.

To further investigate the factors that affect droplet flash-boiling in the AF, the developed model was applied at a fixed 1.26 m injection location using the above bulk flow operating conditions with varying SMD values. Figure 39 shows the predicted axial profiles of T_{boil} and T_{drop}. It shows that the two smallest droplets, $30\mu m$ and $50\mu m$, quickly reach T_{SS} and evaporate upstream of the TS, thereby avoiding the pressure gradient altogether. The $70\mu m$ droplet has a longer lifetime and passes through the TS. Although it experiences the large drop in pressure, it cools rapidly enough to avoid flash boiling. On the other hand, the $90\mu m$ and $110\mu m$ droplets cannot cool rapidly enough and therefore experience flash boiling. This can be attributed to their larger size, which increases their thermal inertia and thus decreases their response time. Interestingly, the

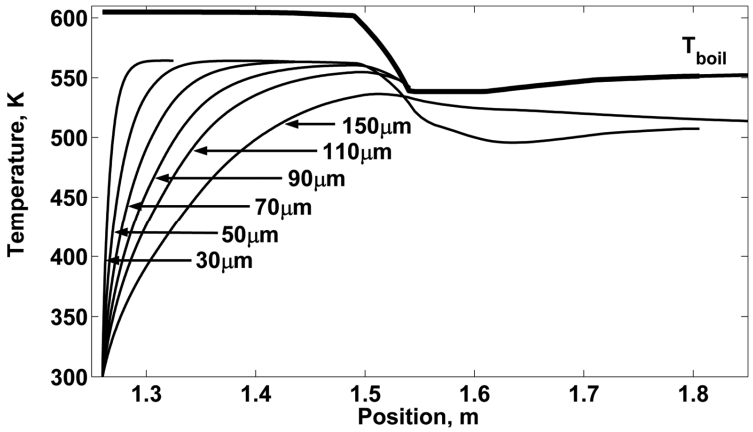

Figure 39. Predicted profiles of boiling temperature and droplet temperature along the AF for the flash boiling case with an injection location of 1.26m and varying initial droplet diameter.

$150\mu m$ droplet does not experience flash boiling. Although it has the slowest thermal response time, the HUT of this droplet is so long that it prevents it from reaching an elevated temperature in the vicinity of the pressure gradient. In other words, as it enters the TS the $150\mu m$ droplet has a large margin between T_{drop} and T_{boil}, which allows it to pass through the TS without flash-boiling.

Figure 40 depicts the data from Figure 39 on a temperature-pressure diagram. Only the $70\mu m$ and $90\mu m$ droplet state trajectories are shown to avoid over-crowding the plot. The T_{SS} profile is approximated at $T_{bulk} = T_{tot}$. Note, however, that T_{SS} actually varies slightly along the AF because of changes in T_{bulk} (see Figure 32). Figure 40 shows that both droplets heat up to T_{SS} before experiencing the TS pressure drop. Upon entering the TS, the state trajectories curve sharply to the left as pressure decreases and slope downward as the droplet temperature decreases. The $90\mu m$ droplet cannot respond rapidly enough and intersects with the T_{boil} profile. On the other hand, the $70\mu m$ droplet responds more rapidly, sloping faster downward toward the T_{SS} profile and thus avoiding an intersection with the T_{boil} profile. Then, the $70\mu m$ droplet trajectory curls around as

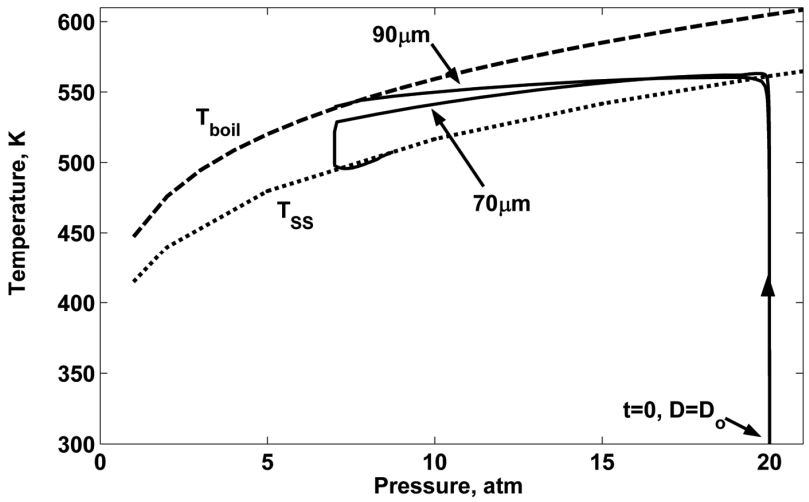

Figure 40. Droplet state trajectories for the flash boiling case at an injection location of 1.26m and with two different initial droplet diameters.

the droplet travels through the TS midpoint and into the diverging section, where there is an increase in P_{bulk} due to the slight diffusion of the flow.

In summary, the theoretical model predicted that Jet-A priming and autoignition is still feasible at high bulk flow pressures. For the most part, the higher operating pressures will accelerate chemical reactions without greatly affecting the overall droplet evaporation time. Consequently, some injection locations are predicted to achieve priming and autoignition more compactly at higher operating pressures while still maintaining a safe distance between the TS and the combustion zone. The model also predicted that the large pressure gradient across the turbine stages could lead to droplet flash-boiling. The occurrence of flash-boiling depends on the magnitude of the pressure gradient and the size and state of the droplets when they experience the pressure gradient. Finally, the general features of the injection/ignition maps are largely unaffected by pressure with the exception of operating conditions that lead to flash boiling, which produces a new region on the map.

PART 3

THE INVESTIGATION OF THE TRIGGER STAGE

Two important conclusions from the prime stage investigation were (1) that fuel can be injected upstream of the TS to establish combustion at a safe distance downstream of the TS and (2) that combustion can occur through autoignition in a repeatable manner. Having thus determined that the prime stage is feasible, the next step - and the subject of Part 3 - was the investigation of the trigger stage. As stated in Section 1.3, the purpose of the trigger stage investigation was to answer the following questions:

- Can the proposed trigger mechanism control and enhance the combustion process in ways that are advantageous to afterburner combustion - i.e. reduce sensitivity to changing operating conditions, decrease the combustion zone length, increase combustion efficiency, and suppress fluctuations?
- How much trigger gas is needed in order to produce the desired performance?
- What trigger gas properties determine its effect on the combustion process, i.e., how does it work?

Part 3 proceeds as follows: Chapter 7 describes Chemkin simulations of autoignition with a trigger; Chapter 8 describes the experiments in the PAC; and Chapter 9 describes experiments in the AF using a H_2 trigger.

CHAPTER 7 CHEMKIN SIMULATIONS OF AUTOIGNITION WITH A TRIGGER

This Chapter describes the Chemkin simulations of Jet-A/vitiated-air autoignition with the addition of H_2 and POx gas triggers. The primary motivation for using Chemkin was to study the POx trigger, which was not available for the AF and PAC experiments. In the process, Chemkin was also used to compare the POx trigger to the H_2 trigger; to evaluate the effects of vitiated-air composition, trigger gas quantity, and Jet-A equivalence ratio on the performance of each trigger; and, finally, to study several aspects of H_2 and POx gas combustion that help explain their performance.

This chapter proceeds as follows: the first section describes the setup for the Chemkin model; the second section describes baseline results for autoignition without a trigger; the third section describes results for autoignition with H_2 and POx triggers; and the last section describes selected trigger gas properties that correlate with their performance. Many of the results presented in this Chapter are expressed in terms of scaled quantities. For example, time is often scaled with the ignition delay time, as defined in Section 7.2. This allowed results with widely ranging magnitudes to be presented on the same chart. Moreover, the applied scaling often generalized the results or emphasized that the results were valid only for certain conditions. To help keep track of the scaled parameters, refer to the Nomenclature section and to Appendix B, which provides illustrations that define and relate each of them. Note that Appendix B also provides tables of the Chemkin results prior to scaling.

7.1 Chemkin Setup

This section describes the setup for the Chemkin simulations. It includes descriptions of the Chemkin reactor model; the Jet-A surrogate fuel composition and chemical mechanism; the POx gas composition, and the operating range for the Chemkin simulations.

Reactor Model

Chemkin simulations were performed in a closed homogeneous batch reactor (CHBR) model held at constant pressure. The CHBR is simply a perfectly-mixed, closed container with a time-varying volume to satisfy the constant pressure constraint. The model requires the following inputs: the initial mixture composition, temperature, and pressure; the initial reactor volume; the chemical mechanism; and the end-time for the simulations. With these inputs, Chemkin steps through time computing the mixture temperature, volume, and species mole fractions at each step until the specified end time is reached.

The constant pressure constraint was imposed in the CHBR model to simulate combustion in an afterburner duct. With this constraint, the CHBR conserves enthalpy instead of internal energy. Note that the CHBR and afterburner still differ, because conservation of enthalpy in an afterburner involves a kinetic energy term. However, the Mach number in an afterburner is below 0.5, so kinetic energy has only a small

contribution to total enthalpy[6]. Thus, the CHBR simulated afterburner combustion without the need for the additional Mach number (or velocity) input parameter.

Jet-A Chemical Mechanism and Surrogate Fuel Composition

The chemical mechanism and Jet-A surrogate fuel composition were chosen based on a Jet-A autoignition investigation by Vasu et. al [24]. In [24], Chemkin autoignition simulations were performed using various chemical mechanisms and surrogate fuel compositions and the results were compared to experimental measurements. The closest match between the Chemkin simulations and experimental data was obtained using the Violi #3 surrogate fuel composition [25] and the Ranzi chemical mechanism [26]. Therefore, this investigation used the Violi #3 surrogate fuel and, to reduce computational time, used the high-temperature subset of the Ranzi mechanism, see [26]. The properties of the Violi #3 surrogate fuel are listed in Table 1.

Trigger Gas Composition

Three trigger gases were used in the Chemkin simulations: H_2 and two compositions of POx gas. Their composition, molecular weight and LHV are listed in Table 2. The H_2 trigger was simulated in Chemkin because it was used in the AF and PAC experiments as a stand-in for the unavailable POx gas. The H_2 trigger also serves as

[6] The total enthalpy of the flow is given by $h(1+\frac{1}{2}(\gamma-1)M^2)$, where h is the static enthalpy, γ is the ratio of specific heats, and M is the Mach number. Thus, the contribution of kinetic energy term, $\frac{1}{2}(\gamma-1)M^2$, to the total enthalpy is given by $\frac{1}{2}(\gamma-1)M^2/[1+\frac{1}{2}(\gamma-1)M^2]$. Assuming a value of $\gamma=1.3$ for the high temperature primary combustor products and a higher end value of 0.5 for the afterburner Mach number, the kinetic energy term amounts to only about 3.6% of the total enthalpy.

Table 1. Violi #3 surrogate fuel composition and the LHV for each constituent. The surrogate fuel molecular weight and LHV are 151g/mol and 43.87 MJ/kg, respectively.

Species	%, Vol	LHV (MJ/kg)
Methylcyclohexane	10 %	43.38
Toluene	10%	40.589
Benzene	1%	40.17
Iso-octane	5.5%	44.427
n-Dodecane	73.5%	44.147

a reference or "gold standard" for judging the performance of other trigger gases. The POx gases used in Chemkin are equilibrium products of methane/air combustion at two rich equivalence ratios (ϕ_{POx}). GasEq was used to generate the methane/air products, and then minor species, such as propane and acetylene, were removed to simplify the POx gas definitions. Figure 41 shows profiles of the species chosen for the POx gases over a wide range of ϕ_{POx}. N_2 is not shown, but is also a POx gas constituent. The two vertical lines mark the values of ϕ_{POx} used in this study. The POx gas at $\phi_{POx} = 3.325$, termed $POx_{(3.325)}$, corresponds to the maximum H_2 content. As such, it was expected to have an

Table 2. Trigger gas properties: species composition (%Vol), molecular weight (g/mol) and LHV (MJ/kmol).

Composition, MW and LHV	POx(3.325)	POx(1.45)	H2
H_2	32.9	7.2	100
CO	15.6	7.9	0
CH_4	1.6	0	0
CO_2	2.4	4.3	0
H_2O	3.1	17.2	0
N_2	44.3	63.4	0
MW	25.1	19.3	2
LHV	135.8	39.8	240.2

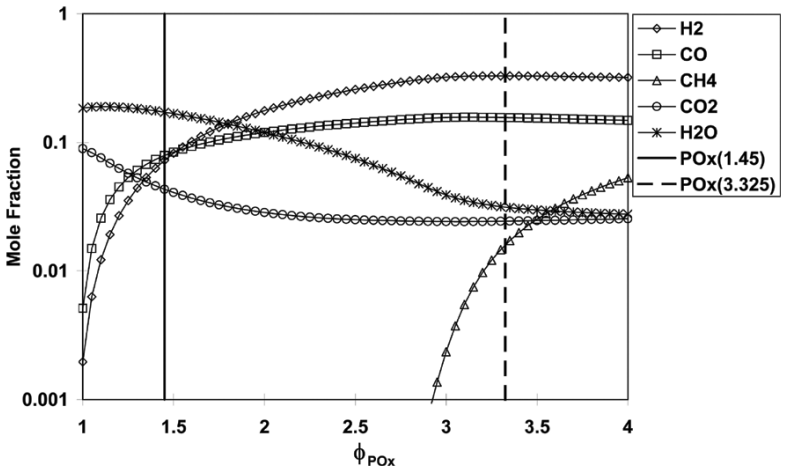

Figure 41. GasEq product composition for rich methane/air combustion with initial temperature and pressure of 300K and 1atm, respectively. All the POx gas constituents are shown expect for N_2.

effect closest to that of the H_2 trigger. The POx gas at $\phi_{POx} = 1.45$, termed $POx_{(1.45)}$, was chosen because 1.45 is the rich blowout limit of the POx reactor currently under development. It also provides an example of a sub-optimal POx trigger, since a larger fraction of the reactant methane is converted to diluents (CO_2 and H_2O) instead of H_2 and CO.

Operating Conditions

The Chemkin simulations were run with an initial temperature and pressure of 1200K and 1atm, respectively. The vitiated-air composition, surrogate-fuel/vitiated-air equivalence ratio ($\phi_{surr.fuel}$), and trigger gas quantity were varied to determine their effect on the trigger performance. Two vitiated-air compositions were used. They consisted of methane/air products at $\phi = 0.4$ and at $\phi = 0.75$, termed vitiated-$air_{(0.4)}$ and vitiated-$air_{(0.75)}$, respectively. Their compositions are listed in Table 3. $\phi_{surr.fuel}$ was assigned values of 0.35 and 0.75 to represent lean and nearly stoichiometric surrogate-fuel/vitiated-air autoignition. Several simulations were also run at $\phi_{surr.fuel}$ of 0.15. Note

Table 3. Composition (%Vol) of the vitiated-air used in the Chemkin simulations

Species	vitiated-air(0.4)	vitiated-air(0.75)
O_2	0.12	0.05
N_2	0.76	0.73
CO_2	0.04	0.07
H_2O	0.08	0.15

that the vitiated-air$_{(0.75)}$ cases are all similar to the PAC operating conditions, and the vitiated-air$_{(0.4)}$ cases with $\phi_{surr.fuel}$ of 0.15 and 0.35 are similar to the AF operating conditions.

7.2 Autoignition without a Trigger

The Chemkin simulations were first run with no trigger to provide baseline results. This section describes the temporal profiles of temperature and species mole fraction from these baselines cases.

Figure 42 shows the temperature profiles for autoignition without a trigger. The results are shown for both vitiated-air compositions, each with $\phi_{surr.fuel}$ of 0.15, 0.35 and 0.75. All the profiles follow a similar trend: the temperature initially decreases very slightly (hard to discern on plot), then remains relatively constant for a period of time, and finally increases rapidly to the adiabatic combustion temperature. The initial temperature decrease occurs as the heavy hydrocarbon molecules break-down endothermically. The ensuing constant temperature period consists of many intermediate reactions that produce nearly zero net heat release. This complex series of reactions builds up the concentration of CO, H_2, and such radicals as O, H, OH, HO_2 and H_2O_2. Eventually, this radical pool reaches a critical concentration that initiates the rapid,

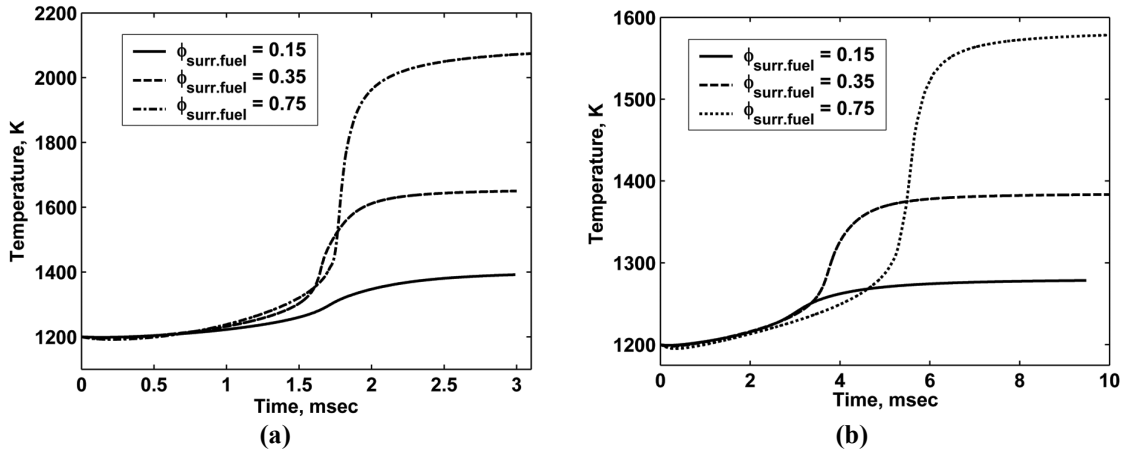

Figure 42. Temperature profiles from surrogate fuel autoignition in (a) vitiated-air$_{(0.4)}$ and (b) vitiated-air$_{(0.75)}$.

exothermic oxidation of the CO to CO_2. This produces the final sharp increases in the temperature profiles.

For this analysis, the ignition delay time of the mixture, t_{ign}, was defined as the time to the maximum temperature gradient (or temperature inflection point). Accordingly, Figure 42(a) shows that t_{ign} of the surrogate-fuel/vitiated-air$_{(0.4)}$ mixture is 1.72 msec, 1.66 msec, and 1.78 msec for $\phi_{surr.fuel}$ of 0.15, 0.35 and 0.75, respectively. This small, non-monotonic variation in t_{ign} suggests that it is not dependent on $\phi_{surr.fuel}$. On the other hand, Figure 42 (b) shows that t_{ign} with vitiated-air$_{(0.75)}$ is 3.02 msec, 3.75 msec, and 5.5 msec for $\phi_{surr.fuel}$ of 0.15, 0.35 and 0.75, respectively, showing that t_{ign} in vitiated-air$_{(0.75)}$ is relatively longer and clearly increases with $\phi_{surr.fuel}$ - a trend that was also observed in the PAC experiments, as will be discussed in Section 8.4.

Figure 43 shows the Chemkin temperature predictions in terms of the following 'scaled time', $t^*_{n.t.}$, and 'scaled temperature increase', $[\Delta T]^*_{n.t.}$:

$$t^*_{n.t.} = \frac{t}{t_{ign,n.t.}} \tag{7.1}$$

where $t_{ign,n.t.}$ is the ignition delay time with no trigger (equal to t_{ign} for these cases).

$$[\Delta T]^*_{n.t.} = \frac{T - T_{initial}}{(T_{final} - T_{initial})_{n.t.}} \tag{7.2}$$

where the quantity in the denominator is the temperature increase from complete combustion with no trigger. The scaled profiles in Figure 43 nearly collapse onto a single profile, especially for $\phi_{surr.fuel}$ greater than 0.15, which reveals somewhat of a 'self-similarity' in the autoignition process. This apparent 'self-similarity' suggests that $t^*_{n.t.}$ is an approximate progress variable for the autoignition process – a property that will be referenced in the next section when defining the method for trigger addition into the CHBR.

Figure 44 shows the time dependence of O_2, CO_2, CO and H_2 mole fractions during autoignition in vitiated-air$_{(0.4)}$. The corresponding profiles are not shown for autoignition in vitiated-air$_{(0.75)}$ because the trends are nearly the same. Figure 44(a) shows

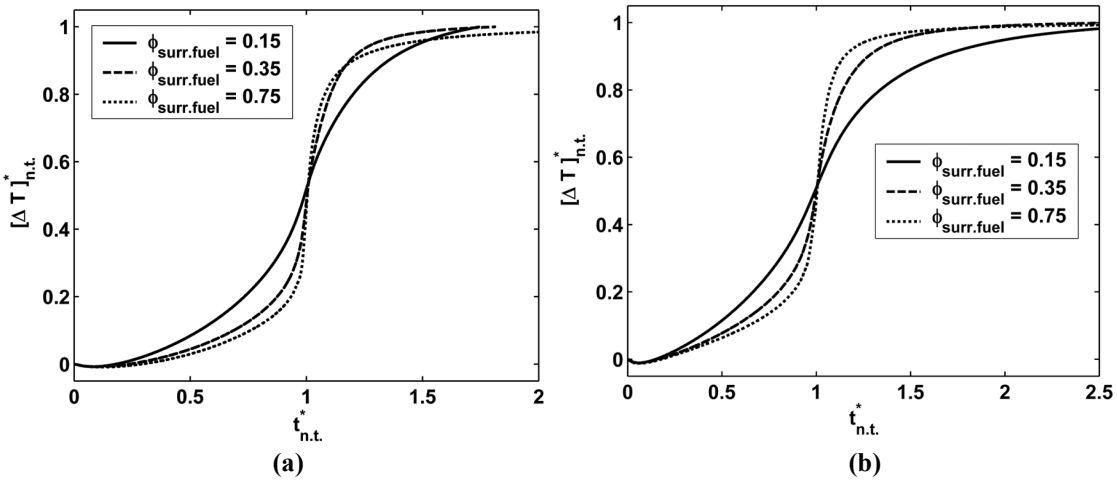

Figure 43 Scaled temperature profiles from surrogate fuel autoignition in (a) vitiated-air$_{(0.4)}$ and (b) vitiated-air$_{(0.75)}$.

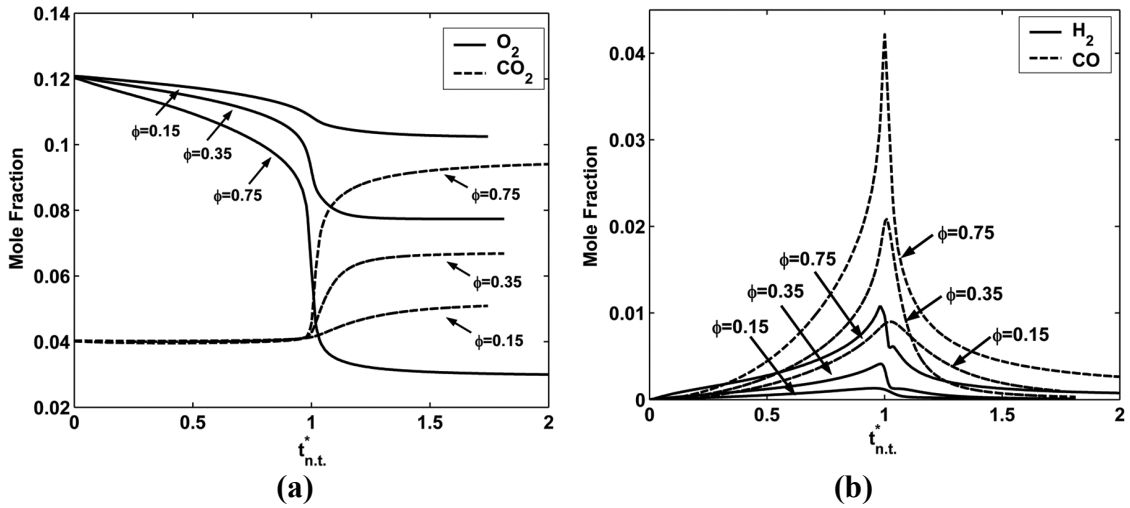

Figure 44. Species mole fractions for combustion in vitiated-air$_{(0.4)}$ with $\phi_{surr.fuel}$ of 0.15, 0.35 and 0.75: (a) O_2 and CO_2, and (b) H_2 and CO

that O_2 is consumed throughout the entire autoignition process. On the other hand, CO_2 production occurs sharply at $t^*_{n.t.} = 1$. Figure 44(b) shows the H_2 and CO profiles. Both species peak at $t^*_{n.t.} = 1$ and their mole fractions increase with $\phi_{surr.fuel}$, as expected. Figure 44(b) suggests that in order to reduce t_{ign} of a primed surrogate-fuel/vitiated-air mixture the H_2 and CO provided by the trigger gas would have to produce effects above and beyond those of the H_2 and CO that are naturally formed during the autoignition process. These 'above and beyond' effects are described in Section 7.4.

7.3 Autoignition with POx and Hydrogen Triggers

This section describes the Chemkin simulations of autoignition with H_2 and POx triggers. First, the method for trigger gas addition is described, and then the Chemkin results are presented.

Method for Trigger Gas Addition in Chemkin

The POx and H_2 triggers were added to the CHBR mixture in a manner that represented the basic PAT concept. They were added after the surrogate-fuel/vitiated-air mixture had begun to react. In this way, the H_2 or POx gas could 'trigger' the autoignition of a partially reacted, or 'primed', mixture. The trigger gas was added at a time referred to as $t_{trigger}$ using the following procedure:

1. The CHBR simulations were run at the desired initial conditions (T=1200K, P=1 atm, vitiated-air$_{(0.4)}$ or vitiated-air$_{(0.75)}$, and varying $\phi_{surr.fuel}$ values) without the trigger, and the values of $t_{ign,n.t.}$ were computed from the results.
2. $t_{trigger}$ was calculated using the $t_{ign,n.t.}$ values (see discussion below)
3. The mixture composition at $t = t_{trigger}$ was extracted from the Chemkin results for the case with no trigger.
4. The desired number of trigger gas moles was added to that composition, keeping temperature and pressure constant.
5. The CHBR model was re-initialized and run using the new mixture composition at the same temperature and pressure as the no trigger case at $t_{trigger}$.

The time for trigger gas addition, $t_{trigger}$, was defined as $0.4t_{ign,n.t.}$. In other words, the trigger gas was added to the mixture at the fixed scaled time $t^*_{n.t.,trigger} = 0.4$. Since $t^*_{n.t.}$ is an approximate progress variable for the autoignition process, the use of a fixed scaled time results in trigger gas addition into 'primed' mixtures with similar composition and temperature regardless of the initial mixture conditions. The value of $t^*_{n.t.,trigger} = 0.4$ was

chosen somewhat arbitrarily to represent the 'middle' of the autoignition process. Note that for all considered operating conditions $t^*_{n.t.} = 0.4$ is after the endothermic (pyrolysis) portion of the autoignition process and before the rapid rise in temperature and CO and H_2 mole fractions, see Figure 43 and Figure 44. $t^*_{n.t.,trigger} = 0.4$ was the only value considered in this study; however, the effect of the trigger gas on the autoignition process depends on the value of $t^*_{n.t.,trigger}$. Therefore, it should be varied in future investigations.

The amount of trigger gas added to the CHBR mixture was quantified using the global power ratio (PR_G) of the trigger gas to the surrogate fuel, which is expressed as follows:

$$PR_G = \frac{\dot{m}_{trigger} LHV_{trigger}}{\dot{m}_{surr.fuel} LHV_{surr.fuel}} \tag{7.3}$$

where LHV is the mass specific lower heat value. PR_G relates the energy added to the flow by the POx trigger to the energy added by the surrogate-fuel (or 'afterburner' fuel in relation to the PAT concept). Note that in a PAT afterburner, a practical trigger should operate at a minimal PR_G so that it does not significantly increase fuel consumption or require more than a very small diversion of the engine core flow to a POx reactor. The amount of trigger gas was also expressed using the H_2 global power ratio, $PR_{G,H2}$, which is defined as follows:

$$PR_{G,H_2} = \frac{\dot{m}_{trigger} Y_{H_2,trigger} LHV_{H_2}}{\dot{m}_{surr.fuel} LHV_{surr.fuel}} \tag{7.4}$$

where $Y_{H_2,trigger}$ is the mass fraction of H_2 in the trigger gas. $PR_{G,H2}$ was used to test an a priori assumption that the trigger gas H_2 content largely dictates its effect on the primed mixture autoignition process. Note that $PR_G = PR_{G,H2}$ for the H_2 trigger.

As described above, the trigger gas was instantaneously and isothermally mixed with the primed mixture in the CHBR. Clearly, this is an idealized scenario. In a PAT afterburner, the trigger gas jet would most likely be at a different temperature than the bulk flow[7], and mixing of the trigger gas jet and the primed mixture would occur at a finite rate. Figure 45 illustrates a trigger gas jet mixing with the bulk flow in an afterburner duct. The schematic neglects afterburner combustion, so only the fluid dynamic processes of mixing and convection are shown. The gray region represents the core of the trigger gas jet. The lines around the core represent iso-contours of local trigger gas power ratio, PR_L, which is defined as

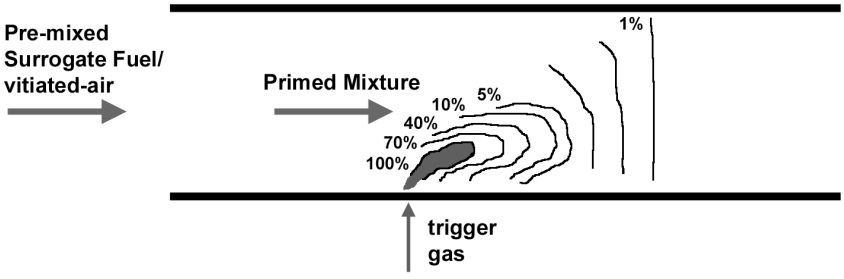

Figure 45. Schematic of trigger gas injection into a primed surrogate-fuel/vitiated-air mixture flowing through a duct.

[7] The temperature of the POx gas depends on the fuel used to generate it, the value of ϕ_{POx}, the initial temperature and pressure of mixture, the losses through the POx reactor and the trigger gas delivery system, and changes in temperature from expansion of the trigger gas to a high velocity jet.

$$PR_L = \frac{\rho_{trigger} LHV_{trigger}}{\rho_{surr/vit} LHV_{surr.fuel}} \tag{7.5}$$

where $\rho_{trigger}$ is the local density of unreacted trigger gas and $\rho_{surr/vit}$ is the density of surrogate fuel in the unreacted, premixed surrogate-fuel/vitiated-air mixture. Note that $PR_L = PR_G$ when the unreacted trigger gas is fully mixed with the bulk flow. In Figure 45, the 100% PR_L iso-contour represents zero mixing of the trigger gas with the bulk flow. The subsequent PR_L iso-contours and assigned numerical values represent the progressive dilution of the trigger gas. The rightmost contour with $PR_L = PR_G = 1\%$ (chosen arbitrarily, but intentionally low) corresponds to a uniform mixture of the trigger gas and bulk flow. In Chemkin, the more realistic scenario of finite trigger gas mixing was simulated by varying the trigger gas PR_G from zero to its maximum value, which corresponds to stoichiometric trigger-gas/surrogate-fuel/ vitiated-air combustion. Thus, the Chemkin values of PR_G may be interpreted as values of PR_L in the vicinity of the PAT afterburner trigger gas jet.

Chemkin Results: Autoignition with H_2 and POx triggers

Chemkin simulations with trigger gas addition were performed in both vitiated-air compositions with $\phi_{surr.fuel}$ of 0.35 and 0.75. The H_2, $POx_{(1.45)}$ and $POx_{(3.325)}$ triggers were added over their full PR_G range for each combination of vitiated-air and $\phi_{surr.fuel}$. Simulations were also performed using the surrogate fuel as a trigger gas. This was done to verify that H_2 and POx gas have unique effects on the primed mixture autoignition process. With so many different cases, the simulations generated a large amount of data.

Thus, $[\Delta T]^*_{n.t.}$ profiles are shown only for a single case to demonstrate typical results. The full set of results is summarized by presenting only the values of t_{ign} for each case. To generalize the results, the values of t_{ign} were presented using the 'scaled time to ignition delay', $[\Delta t]^*_{n.t.}$, which is expressed as follows:

$$[\Delta t]^*_{n.t.} = \frac{t_{ign} - t_{trigger}}{t_{ign,n.t.} - t_{trigger}} = \frac{t_{ign} / t_{ign,n.t.} - t^*_{n.t.,trigger}}{1 - t^*_{n.t.,trigger}} \tag{7.6}$$

Although there are many ways to scale t_{ign}, the above expression for $[\Delta t]^*_{n.t.}$ was used in order to include a dependence on $t_{trigger}$ (or $t^*_{n.t.,trigger}$). This emphasizes that the trigger gas performance depends on $t_{trigger}$ and that the results of this analysis are valid for $t_{trigger} = 0.4 t_{ign,n.t.}$ (or $t^*_{n.t.,trigger} = 0.4$) only.

Figure 46 shows typical results from the simulations of autoignition with a trigger. The results correspond to autoignition in vitiated-air$_{(0.4)}$ with $\phi_{surr.fuel}$ of 0.35. Figure 46(a) shows the $[\Delta T]^*_{n.t.}$ profiles for the H_2 trigger. As expected, the H_2 trigger accelerates the surrogate-fuel autoignition process, and, thus, causes the earlier rise in the $[\Delta T]^*_{n.t.}$ profiles. t^*_{nt} is 0.86 and 0.74 for the 10% and 25% PR_G cases, respectively. In other words, the 10% and 25% PR_G H_2 triggers reduce t_{ign} by 14% and 26%, respectively. The peak $[\Delta T]^*_{n.t.}$ values are 1.096 and 1.236 for the 10% and 25% PR_G cases, respectively. Note that these peak values are greater than unity because $[\Delta T]^*_{n.t.}$ scales the temperature increase with the case with no trigger.

Figure 46(b) and (c) show $[\Delta T]^*_{n.t.}$ profiles for the $POx_{(3.325)}$ and $POx_{(1.45)}$ triggers, respectively. The POx triggers were each added at $PR_{G,H2}$ of 10% and 25%, which are the same values used for the H_2 trigger. These $PR_{G,H2}$ values corresponded to $POx_{(3.325)}$ PR_G values of 17.2% and 43%, and $POx_{(1.45)}$ PR_G values of 23% and 57%, respectively. The $[\Delta T]^*_{n.t.}$ profiles show that the $POx_{(3.325)}$ trigger reduces t_{ign} by 12% and 23% and the $POx_{(1.45)}$ trigger reduces t_{ign} by 11% and 20% for $PR_{G,H2}$ of 10% and 25%, respectively. Thus, at a fixed $PR_{G,H2}$, the *reduction* in t_{ign} decreases slightly from H_2 to $POx_{(3.325)}$ and then again to $POx_{(1.45)}$. This is an interesting result because at a given $PR_{G,H2}$ the values of PR_G, which represent the energy added to the flow, increase from H_2 to $POx_{(3.325)}$ and again to $POx_{(1.45)}$. Thus, the results suggest that the reduction in t_{ign} is more closely correlated to H_2 content than to the energy added to the flow. Moreover, the results show that $POx_{(1.45)}$ is wasteful relative to $POx_{(3.325)}$ because its use requires more trigger gas

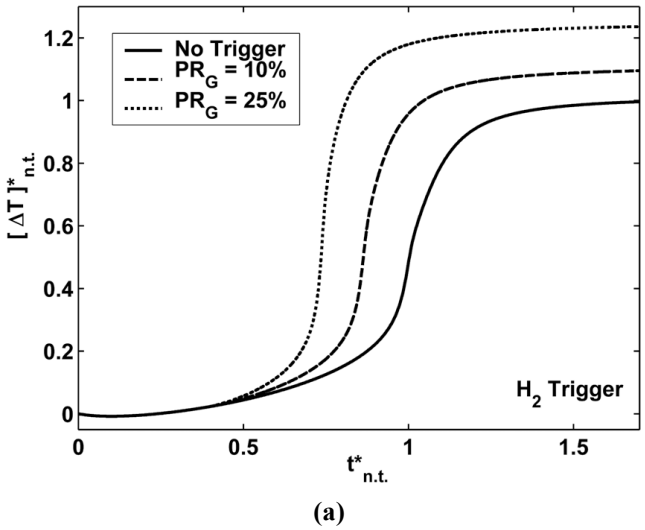

(a)

Figure 46. Scaled temperature profiles from combustion in vitiated-air$_{(0.4)}$ with $\phi_{surr.fuel}$ of 0.35: (a) H_2 trigger; (b) $POx_{(3.325)}$ trigger; and (c) $POx_{(1.45)}$ trigger.

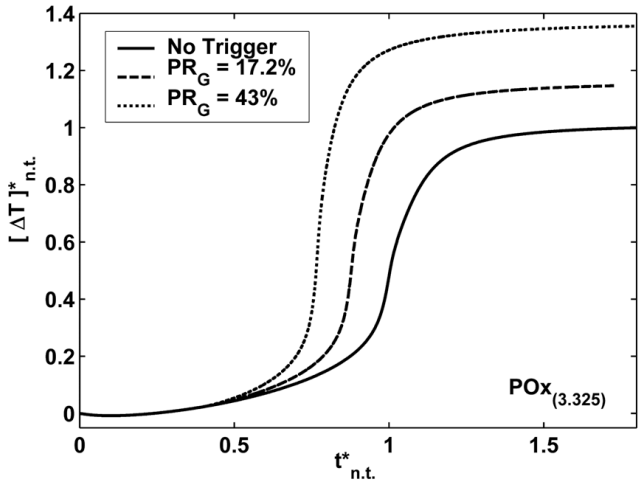

(b)

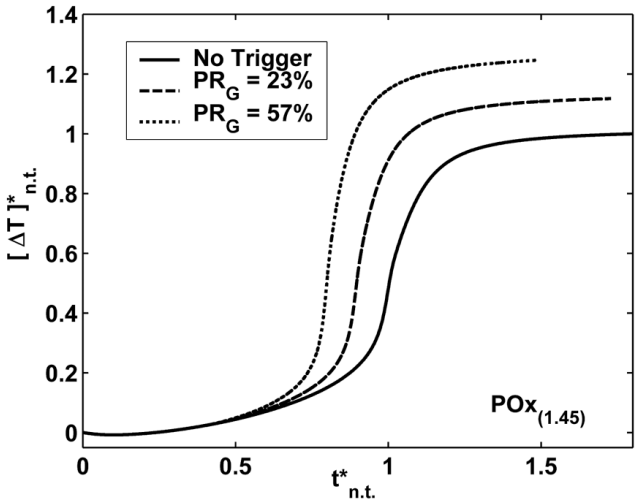

(c)

Figure 46 (continued)

energy input to achieve the same performance.

The Chemkin results for all cases with vitiated-air$_{(0.4)}$ and $\phi_{surr.fuel}$ of 0.35 are summarized by the $[\Delta t]^*_{n.t.}$ profiles in Figure 47. Note that the cases from Figure 46 are represented in these profiles. Figure 47(a) confirms that the H_2 trigger is most effective at reducing $[\Delta t]^*_{n.t.}$ (or t_{ign}) of the mixture over the full PR_G range, followed by the

$POx_{(3.325)}$ trigger and then the $POx_{(1.45)}$ trigger. These results again show that the reduction in $[\Delta t]^*_{n.t.}$ is not solely a function of energy added to the flow (PR_G); otherwise, the $[\Delta t]^*_{n.t.}$ profiles would have collapsed onto a single curve. The results also reiterate that not just any POx gas should be used as a trigger, because $POx_{(3.325)}$ is more effective than the $POx_{(1.45)}$ trigger at a given PR_G. Finally, Figure 47(a) shows that the surrogate fuel trigger actually increases $[\Delta t]^*_{n.t.}$ for all values of PR_G. Thus, despite the addition of energy to the mixture, the surrogate fuel trigger inhibits the autoignition process. This confirms that H_2 and POx gases are specially suited for use as triggers.

Figure 47(b) shows the results from Figure 47(a) as a function of $PR_{G,H2}$. The profiles somewhat collapse, which again suggests that the reduction in $[\Delta t]^*_{n.t.}$ is largely a function of H_2 content. This trend may be misleading, however, because other trigger gas properties change together with the H_2 content and may themselves be the root cause for the reduction in $[\Delta t]^*_{n.t.}$, as discussed in the next section.

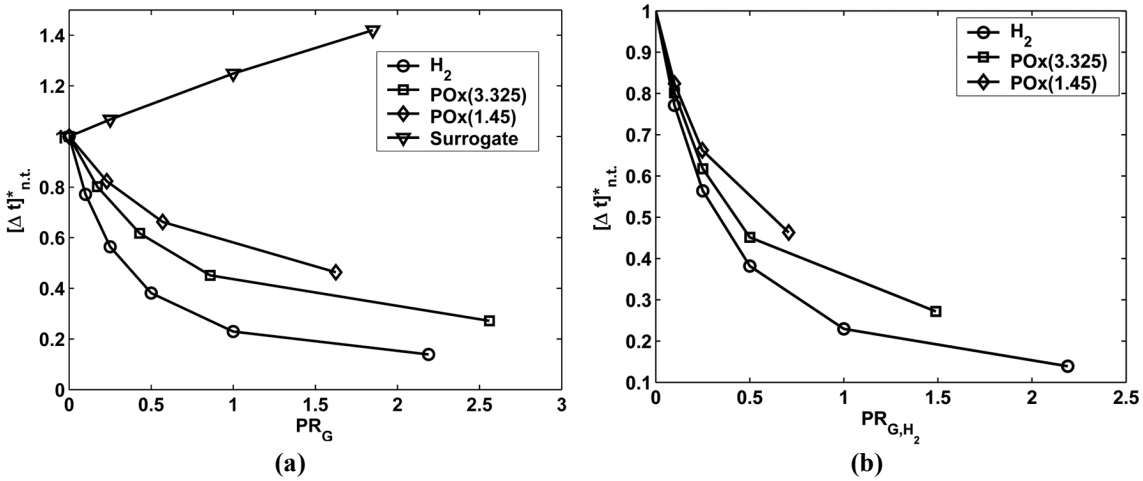

Figure 47. $[\Delta t]^*_{n.t.}$ **profiles for combustion in vitiated-air$_{(0.4)}$ with** $\phi_{surr.fuel}$ **of 0.35 shown as function of (a)** PR_G **and (b)** PR_{G,H_2}**.**

Figure 48 shows the results for autoignition in vitiated-air$_{(0.4)}$ with $\phi_{surr.fuel}$ of 0.75. The trends are the same as in Figure 47 with two exceptions: first, the POx$_{(1.45)}$ trigger actually increases $[\Delta t]^*_{n.t.}$ (see next section for explanation); and, second, the profiles do not collapse as closely when expressed as a function of $PR_{G,H2}$. Also, the H_2 and POx$_{(3.325)}$ triggers are less effective than in the $\phi_{surr.fuel} = 0.35$ case ($[\Delta t]^*_{n.t.}$ values are higher). For example, the minimum $[\Delta t]^*_{n.t.}$ for the H_2 trigger with $\phi_{surr.fuel} = 0.75$ is about 0.55, while the minimum $[\Delta t]^*_{n.t.}$ for the H_2 trigger with $\phi_{surr.fuel} = 0.35$ is about 0.15. Therefore, an increase in $\phi_{surr.fuel}$ lessens the ability of the trigger to decrease t_{ign} and could even reverse its effect for some POx gas compositions.

Finally, Figure 49 shows the results from autoignition in vitiated-air$_{(0.75)}$ with $\phi_{surr.fuel}$ of both 0.35 and 0.75. Unlike autoignition in vitiated-air$_{(0.4)}$, the POx$_{(1.45)}$ trigger reduces $[\Delta t]^*_{n.t.}$ (or t_{ign}) for all values of $\phi_{surr.fuel}$. Also, at a given PR_G the values of $[\Delta t]^*_{n.t.}$ are slightly lower than the corresponding values in vitiated-air$_{(0.4)}$, which indicates

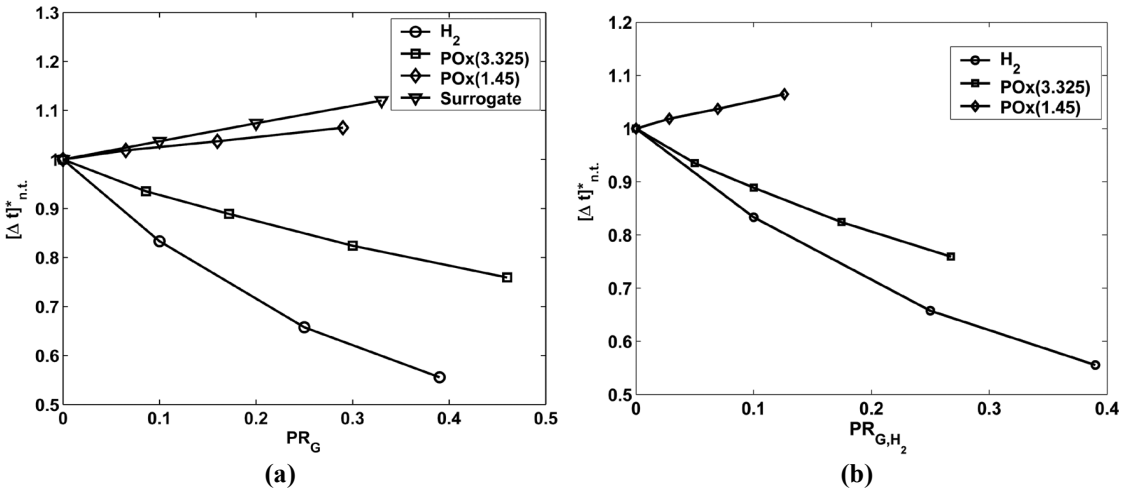

Figure 48. $[\Delta t]^*_{n.t.}$ **profiles for combustion in vitiated-air$_{(0.4)}$ with** $\phi_{surr.fuel}$ **of 0.75 shown as function of (a)** PR_G **and (b)** PR_{G,H_2} **.**

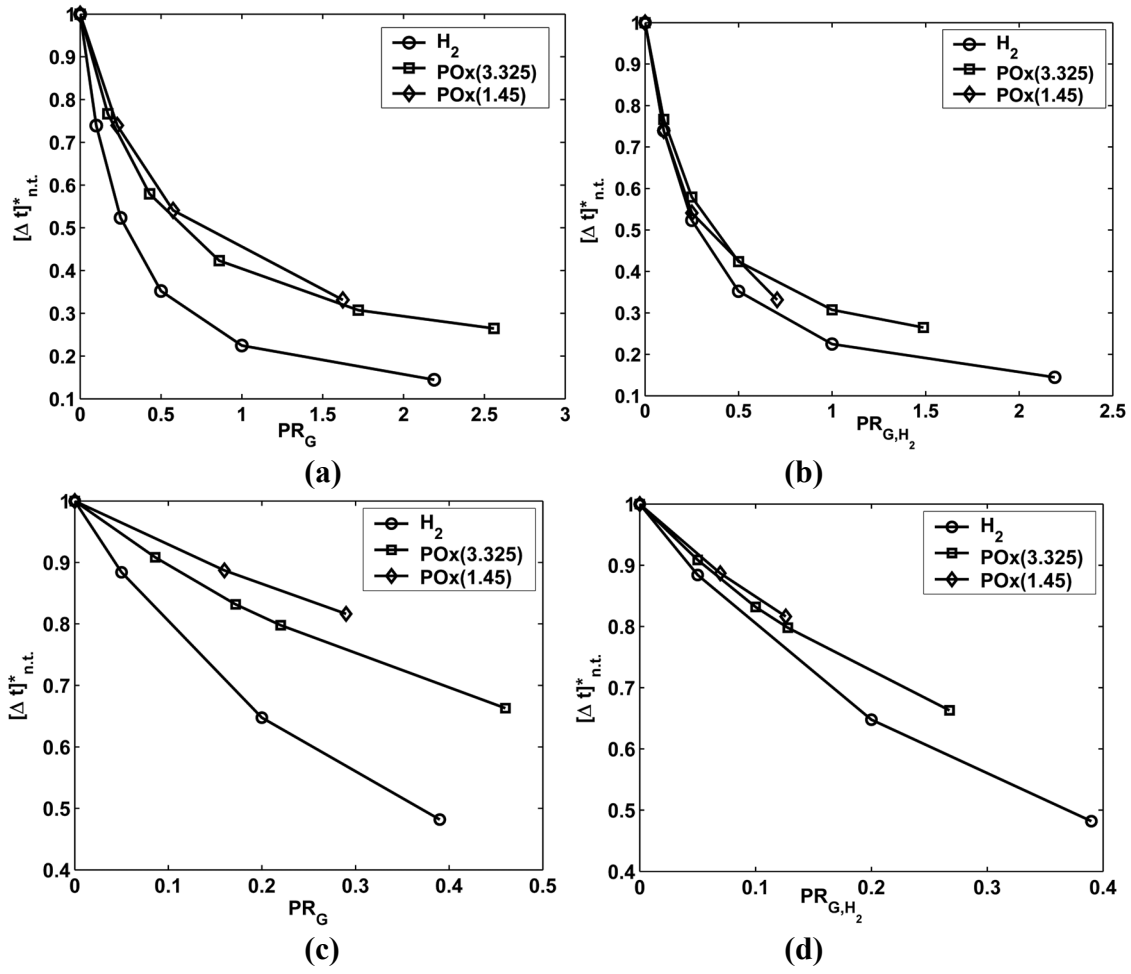

Figure 49. $[\Delta t]^{*}_{n.t.}$ **profiles for combustion in vitiated-air$_{(0.75)}$ for (a)** $\phi_{surr.fuel}$ **of 0.35 as a function of** PR_G **; (b)** $\phi_{surr.fuel}$ **of 0.35 as a function of** PR_{G,H_2} **; (c)** $\phi_{surr.fuel}$ **of 0.75 as a function of** PR_G **; and (d)** $\phi_{surr.fuel}$ **of 0.75 as a function of** PR_{G,H_2} **.**

that the triggers are more effective at the lower vitiated-air O_2 content. Finally, the H_2 and POx profiles collapse more closely together than in the vitiated-air$_{(0.4)}$ cases when expressed as a function of $PR_{G,H2}$.

To summarize, the Chemkin simulations of combustion with a trigger indicate that the H_2 and POx triggers generally reduce t_{ign} of a surrogate fuel/vitiated-air mixture, whereas a surrogate fuel trigger increases t_{ign}. For the most part, $[\Delta t]^{*}_{n.t.}$ decreases with

(1) an increase in PR_G or $PR_{G,H2}$, (2) an increase in trigger gas H_2 content, (3) a decrease in $\phi_{surr.fuel}$ (at a fixed PR_G) and (4) a decrease in vitiated-air O_2 content (higher primary combustion ϕ, at a fixed PR_G). However, the surrogate fuel trigger and the single $POx_{(1.45)}$ case in vitiated-air$_{(0.4)}$ at $\phi_{surr.fuel}$ of 0.75 were exceptions to those trends. As was expected, the H_2 trigger produced the lowest t_{ign}, which is why it serves as a 'gold standard' for judging the relative performance of different POx gas compositions. The POx triggers were actually not too far behind the H_2 trigger if larger quantities were used. For example, the POx triggers produced nearly the same $[\Delta t]^*_{n.t.}$ values as the H_2 trigger when added at the same $PR_{G,H2}$. This suggests that $PR_{G,H2}$ alone could be used to roughly approximate the performance of POx triggers.

7.4 Trigger Gas Properties

An analysis of several trigger gas properties was conducted to help explain the $[\Delta t]^*_{n.t.}$ trends shown in the previous section. The following questions were addressed in this analysis:

- Why did the H_2 and POx gas triggers reduce $[\Delta t]^*_{n.t.}$ while the surrogate fuel trigger increased $[\Delta t]^*_{n.t.}$?
- Why did the $POx_{(1.45)}$ trigger increase $[\Delta t]^*_{n.t.}$ for the single case shown in Figure 48?
- Why was the reduction in $[\Delta t]^*_{n.t.}$ more closely correlated to H_2 content than to the energy added to the mixture (PR_G)?

These questions were addressed by studying the following trigger gas properties:

- The ignition delay time of trigger-gas/vitiated-air (without surrogate-fuel)
- The change in adiabatic temperature due to trigger gas addition
- The rapid production of radicals from the reaction of the trigger gas

The trigger-gas/vitiated-air ignition delay time, termed $t_{ign,trigger}$, was used to indicate the relative trigger-gas and surrogate-fuel chemical reactions rates. Intuitively, a trigger gas should autoignite faster than the primed mixture in order for it affect the primed mixture chemistry. With respect to the Chemkin simulations, this condition can be expressed as $t_{ign,trigger} < \left(t_{ign,n.t.} - t_{trigger}\right)$. If $t_{ign,trigger}$ is too long relative to the primed mixture chemistry, the trigger gas could actually hinder the autoignition process by acting as a diluent or even "stealing" radicals from the primed mixture. If the trigger gas reaction is sufficiently rapid, it could potentially accelerate the primed mixture autoignition process by providing radicals and by increasing the mixture temperature, which are the two other properties considered in this analysis.

The adiabatic (or equilibrium) temperature of the trigger-gas/surrogate-fuel/vitiated-air mixture was studied to determine how changes in the product temperature correlate with the computed changes in $[\Delta t]^*_{n.t.}$ (or t_{ign}). Naturally, it was expected that an increase in temperature from trigger gas combustion would cause a decrease in $[\Delta t]^*_{n.t.}$. The effect of temperature also depends on when the trigger gas is added to the mixture. Thus, the results of this analysis are specific to $t^*_{n.t.,trigger} = 0.4$. Note that the temperature increase from trigger gas combustion is also related to $t_{ign,trigger}$,

which dictates how much time the trigger takes to provide thermal energy to the primed mixture.

Finally, radical production was studied to determine how the trigger gas interacts with the prime mixture on a chemical level, rather than acting simply as a source of thermal energy. When the H_2 and POx triggers are added to the high temperature primed mixture, they immediately begin to react. For example, the H_2 in the trigger gas rapidly dissociates into H atoms. These H atoms react with the O_2 and other intermediate species in the mixture to form O, OH, H_2O_2, and HO_2 [10]. In the absence of hydrocarbon molecules, these radicals and intermediate species would form H_2O, thus completing the H_2 oxidation process. However, in the PAT application the H_2 dissociates in the presence of a primed hydrocarbon mixture. Therefore, the radicals are unavoidably shared between the species originating from the trigger gas and the species originating from the afterburner fuel. Since the radicals provided by the trigger gas are crucial for hydrocarbon autoignition [5, 27, and 28], this chemical interaction is likely an important underlying mechanism for the observed reduction in $[\Delta t]^*_{n.t.}$. Note that the effect of radicals also depends on $t_{trigger}$ (time of trigger addition, not $t_{ign,trigger}$), since the primed mixture composition encountered by the radicals depends on when the trigger gas is added.

It should be noted that the trigger gas diluents also plays a role in this process. For example, differences in trigger gas diluent content lead to differences in adiabatic temperature at a fixed PR_G. Also, the diluent content can reduce the influence of radicals by lowering their concentration. This is discussed in more detail in the following sections.

The Trigger Gas Ignition Delay Time

The autoignition of trigger-gas/vitiated-air was simulated in Chemkin using the following procedure:

1. The desired PR_G of trigger gas was added to the CHBR mixture at $t^*_{n.t.,trigger} = 0.4$ following steps #1-4 in Section 7.3.
2. All other species were removed from the new mixture except for O_2, N_2, CO_2, H_2O, and the trigger gas species.
3. The CHBR simulation was run using this new mixture as the initial composition and the previous mixture temperature at $t^*_{n.t.} = 0.4$ as the initial temperature.

Since the total mole fraction of the removed species (step #2) was relatively small, this procedure was similar to selectively 'freezing' the surrogate-fuel chemistry. Note that the partial oxidation process that occurs from $t^*_{n.t.} = 0$ to $t^*_{n.t.,trigger} = 0.4$ consumes O_2 and produces CO_2 and H_2O. Thus, the vitiated-composition used for the trigger-gas autoignition simulations differs from the original vitiated-air composition (e.g., vitiated-air$_{(0.4)}$). As such, the results are specific to $t^*_{n.t.,trigger} = 0.4$.

The trigger-gas/vitiated-air autoignition analysis was performed only for an initial mixture of surrogate-fuel/vitiated-air$_{(0.4)}$ at $\phi_{surr.fuel}$ of 0.75. This was the case where the POx$_{(1.45)}$ trigger increased $[\Delta t]^*_{n.t.}$, see Figure 48. The results of this study were expressed in terms of the 'scaled trigger-gas ignition delay time', $t^*_{\Delta t,n.t.}$, which is defined as follows:

$$t^*_{\Delta t,n.t.} = \frac{t_{ign,trigger}}{t_{ign,n.t.} - t_{trigger}} = \frac{t_{ign,trigger} \big/ t_{ign,n.t.}}{1 - t^*_{n.t.,trigger}} \tag{7.7}$$

Note that $t^*_{\Delta t,n.t.}$ is a convenient expression of the aforementioned hypothesis that a trigger can accelerate the primed mixture autoignition process if $t_{ign,trigger} < (t_{ign,n.t.} - t_{trigger})$, which translates to $t^*_{\Delta t,n.t} < 1$.

Figure 50 shows $t^*_{\Delta t,n.t.}$ profiles for each trigger gas. As expected, the H_2 trigger has the lowest $t^*_{\Delta t,n.t.}$, between 0.75 and 0.85. The $POx_{(3.325)}$ trigger has a slightly higher $t^*_{\Delta t,n.t.}$, between 0.78 and 0.92. The $POx_{(1.45)}$ trigger starts with $t^*_{\Delta t,n.t.} > 1$. Therefore, it is not surprising that the $POx_{(1.45)}$ trigger increased $[\Delta t]^*_{n.t.}$ at low PR_G for the vitiated-$air_{(0.4)}$/$\phi_{surr.fuel} = 0.75$ case. However, $t^*_{\Delta t,n.t.}$ for $POx_{(1.45)}$ drops below 1 for PR_G greater than about 0.09, even though $POx_{(1.45)}$ increased $[\Delta t]^*_{n.t.}$ over the entire PR_G range. Thus, the hypothesized condition that a trigger can accelerate the primed mixture autoignition process if $t^*_{\Delta t,n.t.} < 1$ does not hold, or the condition is countered by other properties of the $POx_{(1.45)}$ trigger.

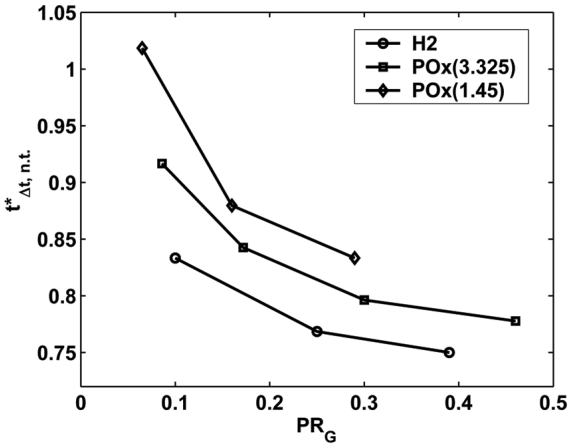

Figure 50. $t^*_{\Delta t,n.t.}$ profiles for autoignition of trigger gas in the products of surrogate-fuel/vitiated-$air_{(0.4)}$ at $t^*_{n.t.} = 0.4$ (where $t^*_{ign,n.t.} = 1.8 m\sec$ for this case).

The Adiabatic Temperature of the Surrogate-fuel/Trigger-gas/Vitiated-air Mixture

The adiabatic temperature of the surrogate-fuel/vitiated-air/trigger-gas mixture was studied using the following 'scaled increase in adiabatic temperature':

$$[\Delta T]^{*}_{n.t.,final} = \frac{T_{final} - T_{initial}}{(T_{final} - T_{initial})_{n.t.}} \tag{7.8}$$

where $T_{initial}$ is the initial mixture temperature of 1200K, T_{final} is the mixture temperature after complete combustion, and the quantity with the subscript 'n.t.' corresponds the case with no trigger.

Figure 51(a) show profiles of $[\Delta T]^{*}_{n.t.,final}$ for combustion in vitiated-air$_{(0.4)}$ with $\phi_{surr.fuel}$ of 0.35. The $[\Delta T]^{*}_{n.t.,final}$ profile for the surrogate fuel trigger is not shown because it nearly overlaps with the H_2 profile. This occurred because both are pure fuels, so for the same PR_G they added the same amount of energy to the system and none of it is wasted in heating extra diluents. At a given PR_G, $[\Delta T]^{*}_{n.t.,final}$ decreases from the H_2 (and

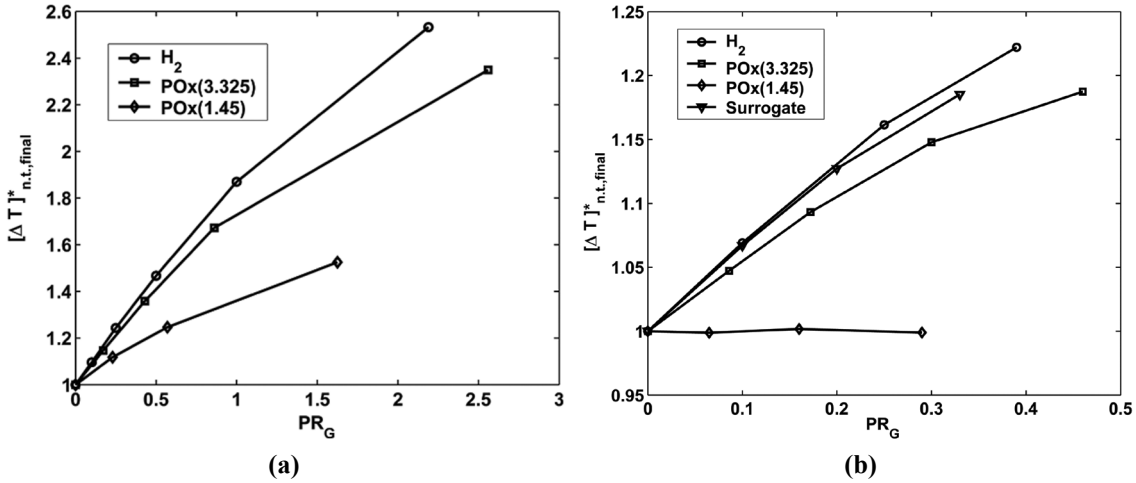

Figure 51. $[\Delta T]^{*}_{n.t.,final}$ **profiles for combustion in vitiated-air$_{(0.4)}$ at** $\phi_{surr.fuel}$ **of (a) 0.35 and (b)0.75**

surrogate fuel) trigger to $POx_{(3.325)}$ and then again to $POx_{(1.45)}$. This is because of the increasing trigger gas diluent content at a given PR_G. Comparison with Figure 47 shows that the H_2 and POx $[\Delta T]^*_{n.t.,final}$ profiles exhibit the expected trend, namely, that $[\Delta t]^*_{n.t.}$ decreases as $[\Delta T]^*_{n.t.,final}$ increases. However, the surrogate fuel trigger exhibits the complete opposite trend. Although it increases $[\Delta T]^*_{n.t.,final}$, it also increases $[\Delta t]^*_{n.t.}$. Thus, temperature alone cannot explain the effects of the trigger gas.

Figure 51(b) show profiles of $[\Delta T]^*_{n.t.,final}$ for combustion in vitiated-air$_{(0.4)}$ with $\phi_{surr.fuel}$ of 0.75, which was the case where the $POx_{(1.45)}$ increased $[\Delta t]^*_{n.t.}$. For this case, the surrogate-fuel and H_2 profiles do not overlap, which is likely due to small differences in the product gas specific heat. $[\Delta T]^*_{n.t.,final}$ is approximately equal to one for the $POx_{(1.45)}$ trigger over the entire PR_G range. Evidently, for this case the energy added by the $POx_{(1.45)}$ gas is used only to heat its own diluents.

Figure 52 shows the correlation between $[\Delta T]^*_{n.t.,final}$ and $[\Delta t]^*_{n.t.}$ for all the cases considered in the Chemkin analysis: both vitiated-air compositions; $\phi_{surr.fuel}$ of 0.35 and 0.75; and the full range of PR_G for each trigger. It shows that the H_2 and POx data nearly overlap. Without the surrogate fuel trigger results, this would have suggested a direct correlation between $[\Delta T]^*_{n.t.,final}$ and $[\Delta t]^*_{n.t.}$. However, again the surrogate-fuel trigger exhibits the complete opposite trend. This confirms that that the performance of the trigger gas is dependent on other factors besides temperature increase. Note that, with the exception of the surrogate fuel trigger the data suggest that $[\Delta t]^*_{n.t.} < 1$ if $[\Delta T]^*_{n.t.,final} > 1$. This condition even holds for all cases of $POx_{(1.45)}$ addition.

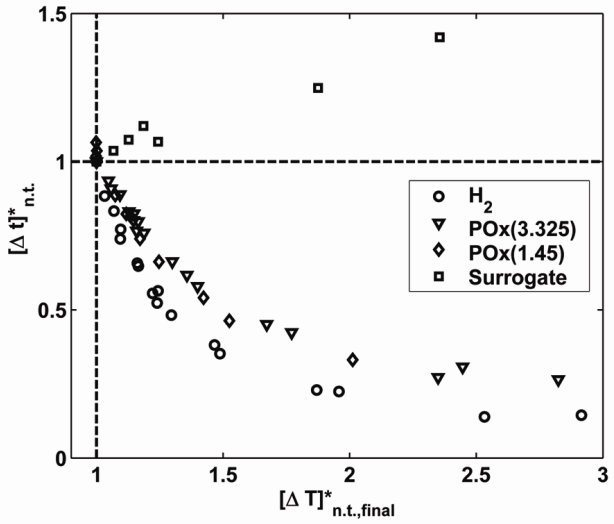

Figure 52. Correlation between $[\Delta t]^*_{n.t.}$ and $[\Delta T]^*_{n.t.,final}$ for all the Chemkin cases considered in this study.

Radicals Contributed by the Trigger Gas

The following is a brief qualitative analysis of radical production by the H_2 and POx trigger gases. Results are shown only for vitiated-air$_{(0.4)}$ at $\phi_{surr.fuel}$ of 0.35. The discussed radicals are O, OH, H_2O_2, and HO_2. As stated previously, these radicals are produced by the H_2 in the trigger gas and are critical for hydrocarbon autoignition.

Figure 53 through Figure 55 present mole fraction profiles of the above-mentioned radicals for cases with a H_2 trigger. Figure 53(a) shows the temporal shift and the increase in the O and H mole fractions with increasing PR_G. The peaks of the O and H profiles are situated at the corresponding values of t_{ign} for each case. Figure 53(b) is a zoomed-in view at the time of H_2 addition. It reveals an immediate increase in H atom mole fraction from the dissociation of a small fraction of the H_2 trigger gas. This increase in H is almost immediately accompanied by an increase in O atom mole fraction and also OH mole fraction, which is shown in Figure 54. Figure 55 shows that the H_2 accelerates

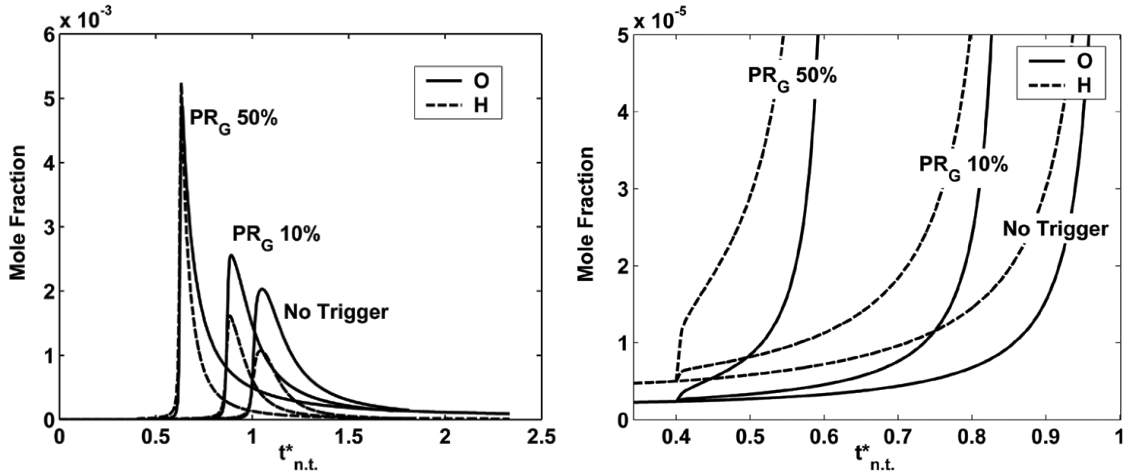

Figure 53. Mole fraction profiles of O and H from combustion in vitiated-air$_{(0.4)}$ with $\phi_{surr.fuel}$ of 0.35 and with a H_2 trigger: (a) full time scale and (b) time of trigger addition.

the HO_2 and H_2O_2 production and produces a slight HO_2 overabundance relative to the no trigger case.

Figure 56 shows the mole fraction profiles of H, HO_2 and H_2O_2 for POx$_{(3.325)}$ and POx$_{(1.45)}$ triggers. The POx triggers are added at $PR_{G,H2}$ of 10% and 25%. The H and O atom profiles again shift in time due to the changes in t_{ign}. The 10% $PR_{G,H2}$ cases produce the same initial increase in H mole fraction as the 10% PR_G H_2 trigger, which is

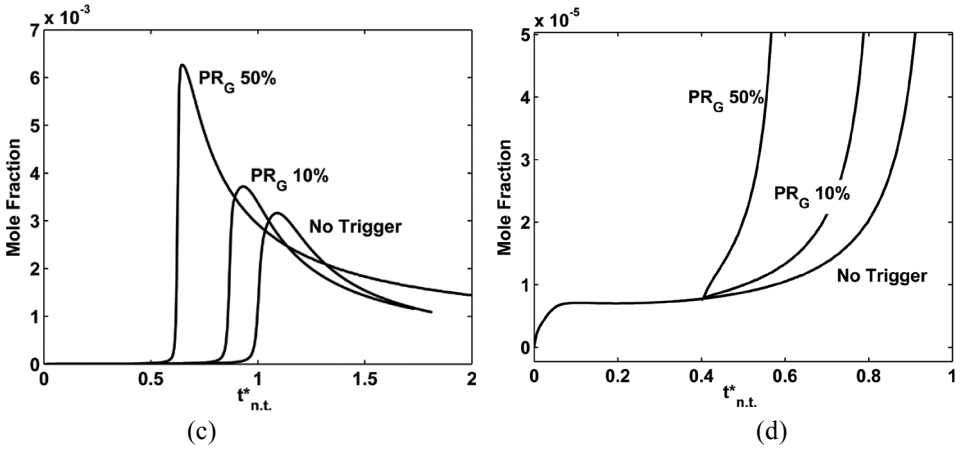

Figure 54 OH mole fraction profiles from combustion in vitiated-air$_{(0.4)}$ with $\phi_{surr.fuel}$ of 0.35 and with a H_2 trigger: (a) full time scale and (b) time of trigger addition.

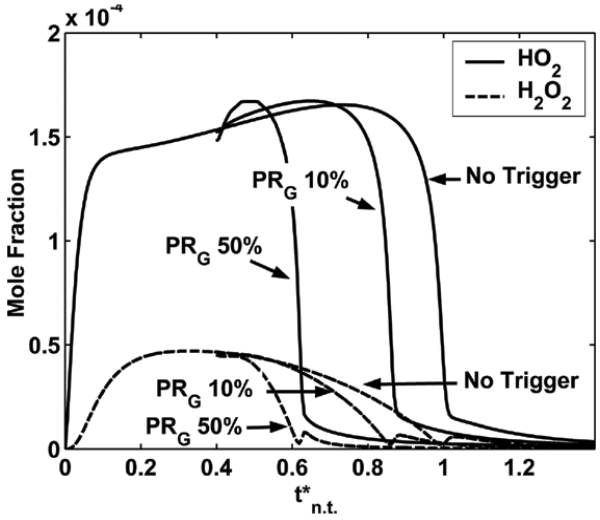

Figure 55. Profiles of HO_2 and H_2O_2 from combustion in vitiated-air$_{(0.4)}$ with $\phi_{surr.fuel}$ of 0.35 and with a H_2 trigger.

expected since the same amount of H_2 is added to the mixture. However, the HO_2 and H_2O_2 profiles differ significantly from those for the H_2 trigger. HO_2 and H_2O_2 are produced in smaller quantities than H. Consequently, the large fraction of diluents in the POx gases actually lowers the HO_2 and H_2O_2 mole fractions, thus inhibiting their participation in the autoignition process. This effect is strongest for the $POx_{(1.45)}$, which has the largest fraction of diluents. Therefore, these radical mole fraction profiles suggest that one of the reasons for the decrease in trigger effectiveness from H_2 to $POx_{(3.325)}$ and then again to $POx_{(1.45)}$ is the reduced production and increased dilution of radicals.

Trigger Gas Properties: Summary

Chemkin simulations were conducted to correlate trigger gas performance with (1) the trigger-gas/vitiated-air ignition delay time, expressed as $t^*_{\Delta t,n.t.}$; (2) the trigger-gas/surrogate-fuel/vitiated-air adiabatic flame temperature, expressed as $[\Delta T]^*_{n.t.,final}$; and (3) the rapid production of radicals from the trigger gas H_2 component. The results

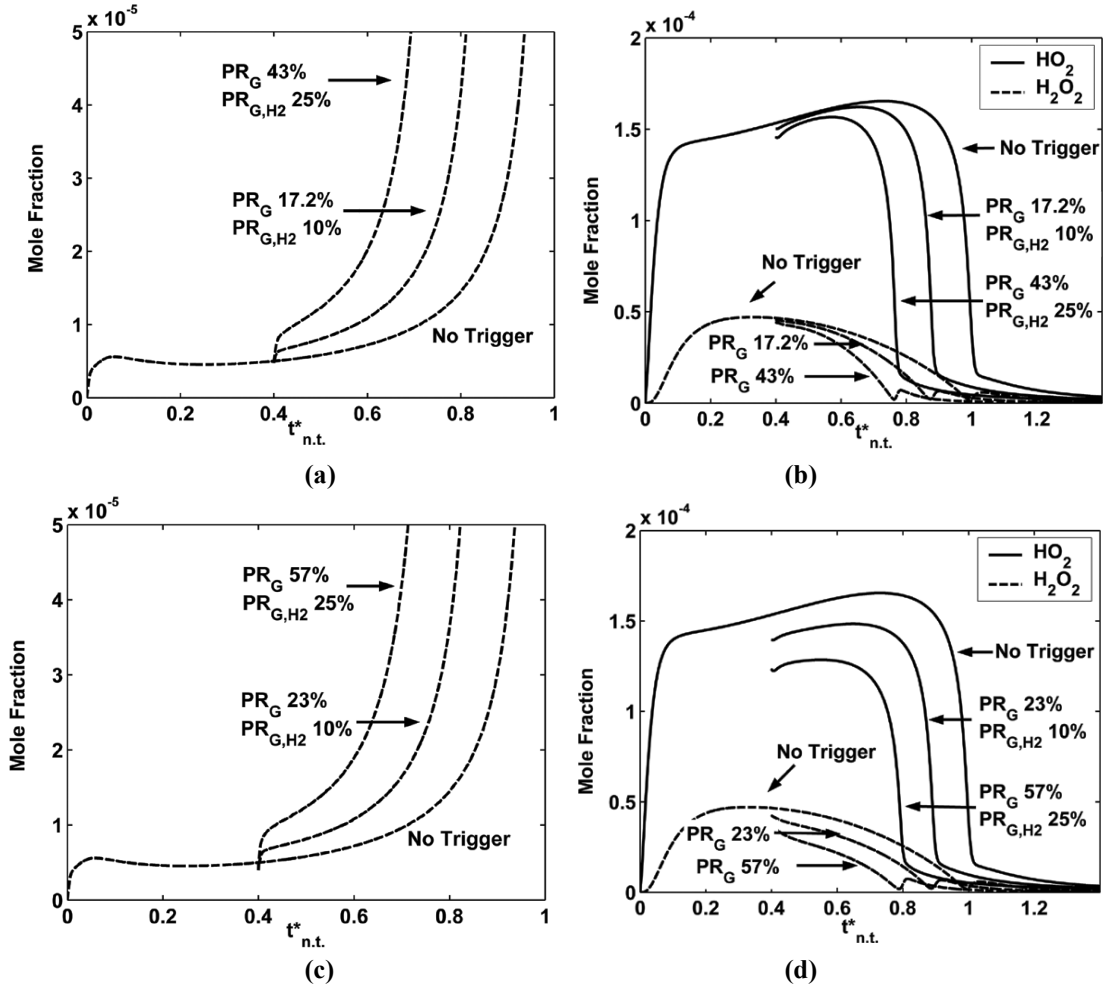

Figure 56. Mole fraction profiles from combustion in vitiated-air$_{(0.4)}$ with $\phi_{surr.fuel}$ of 0.35: (a) H profiles with POx$_{(3.325)}$; (b) HO_2 and H_2O_2 profiles with POx$_{(3.325)}$; (c) H profiles with POx$_{(1.45)}$; and (d) HO_2 and H_2O_2 profiles with POx$_{(1.45)}$.

showed that $[\Delta t]^*_{n.t.}$ clearly correlates with both $t^*_{\Delta t,n.t.}$ and $[\Delta T]^*_{n.t.,final}$. There were, however, some exceptions: the POx$_{(1.45)}$ trigger increased $[\Delta t]^*_{n.t.}$ for only a single case; and the surrogate-fuel trigger always increased $[\Delta t]^*_{n.t.}$. These exceptions indicate that not just any gas can be used as a trigger mechanism in a PAT afterburner. The results from all the simulations can be combined into the following criterion for a suitable trigger gas: $t^*_{\Delta t,n.t.} < 1$ *and* $[\Delta T]^*_{n.t.,final} > 1$. This criterion essentially places lower limits on the trigger

gas reaction rate and energy density relative Jet-A, and it is consistent with the surrogate fuel trigger and the $POx_{(1.45)}$ exception. Radical production is not included in the above criterion, because a single metric that quantifies radicals was not defined. Note, however, that the trigger gas ignition delay time ($t^*_{\Delta t,n.t.}$) may indirectly reflect the radical production rate. The Chemkin simulations showed that the H_2 component of the trigger gas dissociates almost immediately and reacts to form radicals such as OH, HO_2 and H_2O_2. These radicals help initiate or accelerate the hydrocarbon autoignition process. Thus, rapid radical production is an important requirement for an effective trigger gas.

CHAPTER 8 EXPERIMENTS IN THE PAC

This Chapter describes the experiments of propane/vitiated-air combustion with a H_2 trigger in the PAC, which was shown in Figure 11. The PAC had several roles in the trigger stage investigation, each discussed in detail shortly. The initial purpose of the PAC was to help interpret the AF results by addressing certain deficiencies in the AF measurement techniques. In the process, the PAC was also used to formulate and demonstrate a procedure for quantifying the effects of the trigger (later applied to the AF results). In a more general sense, the PAC represented an intermediate step between the Chemkin simulations and the AF trigger stage experiments. As such, it provided a larger overall picture of the PAT concept and, notably, helped reduce the number of costly, time-consuming AF experiments.

The PAC measurements of gas composition and chemiluminescence were more detailed than those in the AF experiments. For example, the Horiba gas analyzer measured both the dry O_2 and dry CO_2 mole fractions via a water-cooled sampling probe. This ensured quick quenching of the sampled gas and more accurate estimates of combustion efficiency. In the AF, only the dry O_2 mole fraction was measured and the probe was not water-cooled. The PAC gas analyzer measurements were used to determine if dry O_2 alone was an accurate indicator of combustion efficiency in the AF. The PAC combustion zone intensity was measured using an optical spectrometer, which allowed the distinction between chemiluminescence and background radiation. The AF intensity measurements taken through the 430+/-5nm filter did not allow this distinction.

Thus, the PAC intensity measurements helped determine the magnitude of background radiation and its effect on both the PAC and AF combustion zone analysis. Finally, the PAC design afforded measurements of continuous axial intensity profiles. In contrast, the intensity profiles measured in the AF were segmented because of the gaps between the windows. Curve-fits had to be applied to the AF measurements to form the continuous profiles necessary for analysis, as described in Section 9.1. The PAC played the important role of providing examples of complete axial intensity profiles, which could then be used to confidently apply polynomial curve-fits to the AF data.

The PAC was an intermediate step between the Chemkin simulations and the AF trigger stage experiments because of the transition from numerical to experimental results and the increase in the combustion process complexity. The latter concerns the role of mixing, evaporation, chemical kinetics and variable bulk flow properties. As described in Chapter 7, the combustion process in Chemkin depended only on chemical kinetics because it assumed a uniform mixture and instantaneous trigger gas addition. In contrast, the PAC combustion process depended on both mixing and chemical kinetics because the H_2 trigger was added through a tube pointed in the flow direction. This was still simpler than the AF, where the combustion process depended on Jet-A evaporation, mixing, chemistry and variable bulk flow properties, as described in Chapter 5. Notably, the simplicity of the PAC combustion process relative to the AF afforded its smaller, simpler design. This, in turn, made it more accessible during experiments and provided the opportunity to use the spectrometer and Horiba gas analyzer for more detailed measurements.

The operating range of the PAC was dictated by the lean blowout limit (LBO) of the primary combustor. The LBO was at an equivalence ratio (ϕ_1) of about 0.65, and stable operation was achieved for $\phi_1 > 0.7$. Although this minimum stable ϕ_1 is higher than typical combustors, it was still low enough to produce vitiated-air with sufficient O_2 content for propane autoignition. Moreover, this range of ϕ_1 was not attainable in the AF, where the corresponding equivalence ratio, termed ϕ_{vit}, was limited to the range of about 0.4 to 0.55. Thus, the PAC complemented the AF experiments by extending the measurements of combustion with a trigger to higher values of primary combustor equivalence ratio (and, thus, lower vitiated-air O_2 content). For all the results presented in this chapter, the PAC air flow rate was about 2.5g/s and ϕ_1 was about 0.77. The resulting test section temperature was between 1510-1525K. Note that the vitiated-air composition was approximately the same as vitiated-air$_{(0.75)}$ from the Chemkin simulations.

This chapter consists of five sections: the first section describes the procedure for post-processing the spectrometer data; the second section describes the combustion zone analysis method; the third section presents the expressions used in the analysis of gas composition and combustion efficiency; the fourth section presents the results from PAC experiments with and without the H_2 trigger; and, finally, the last section reviews the PAC results that were used to support the AF measurements.

8.1 Processing the Optical Spectrometer Measurements

This section describes the procedure for processing the optical spectrometer measurements into axial profiles of total, background, and chemiluminescence intensity.

Figure 57 shows an example of a spectrometer measurement taken midway along the test section. The data corresponds to primary combustion of natural-gas/air at $\phi_1 \approx 0.8$ followed by propane/vitiated-air combustion at a slightly rich equivalence ratio (not carefully measured for this sample run), termed ϕ_2. Natural gas was used only for this case; all other tests used methane. The points are the raw data and the solid line connects the data points after removal of pixel noise. The pixel noise was removed by analyzing the spectrum when the combustor was off and cold. At these conditions, the measured 'dark spectrum' exhibited a small mean offset from zero with fluctuations of individual pixels about this mean. The standard deviation of the dark spectrum data was computed, and any pixel measuring intensity greater than one standard deviation from the mean was removed from all subsequent data sets. This procedure was applied to dark spectra recorded before each set of tests, and it typically removed about 6% of the pixels. Note that this is a heuristic procedure. The one standard deviation condition was chosen because it provided a visibly smoother profile without removing too many pixels or

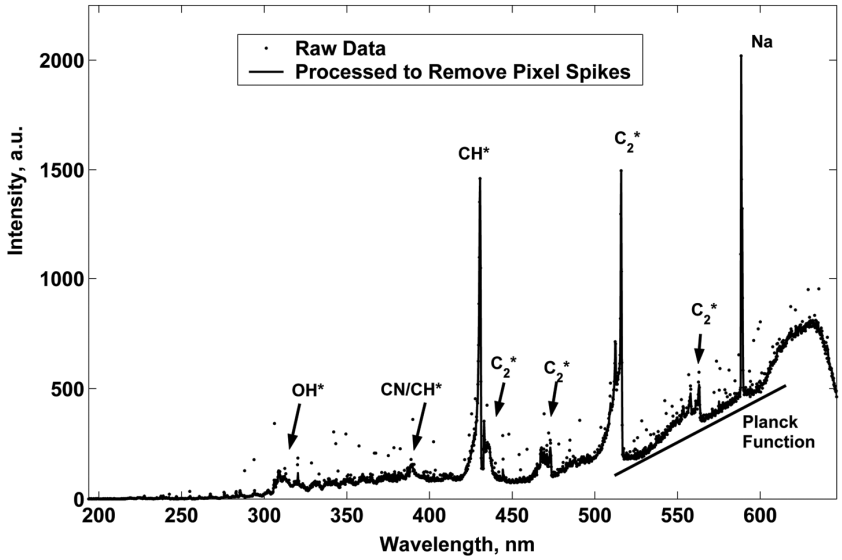

Figure 57. Sample optical spectrometer measurement taken midway along the test section length.

reducing the spikes produced by chemiluminescence. Also note that the dark spectrum mean was also subtracted from subsequent measurements with the combustor in operation in order to set zero intensity.

Figure 57 displays typical features of a hydrocarbon combustion spectrum. Peaks from OH* and CH* chemiluminescence are centered at 309nm and 430nm, respectively. A small peak from CN/CH* is visible at about 390nm and series of C_2* peaks are observed from about 433nm to 565nm. The natural gas must have contained a trace amount of sodium, since the 589nm sodium doublet was present. The baseline of the spectrum (the profile excluding the spikes from OH*, CH*, C_2*, and CN*) is greater than zero for wavelengths greater than about 300 nm. For wavelengths less than about 450 nm, this baseline intensity is background radiation from sources such as CO_2* chemiluminescence [29]. At wavelengths greater than 450 nm, the thermal radiation from the ceramic and quartz add to the background radiation and cause the baseline profile to slope upward as a Planck function. The intensity drops to zero for wavelengths greater than 600 nm because of the rapidly decreasing spectrometer sensitivity.

Figure 58 shows the portions of the spectrum from Figure 57 that are used to compute total, background and chemiluminescence intensity. Figure 58(a) shows the 430+/-5nm wavelength range, which contains the CH* chemiluminescence intensity. Total intensity in this wavelength range is computed by integrating the spectrum profile from 425nm to 435nm. Note that a small C_2* peak is observed at about 433nm, but its contribution to the measured intensity is relatively small. The background radiation intensity is estimated as the area within the trapezoid drawn on the plot, where the heights of the top left and top right corners are the average intensities from 415nm to 425nm and

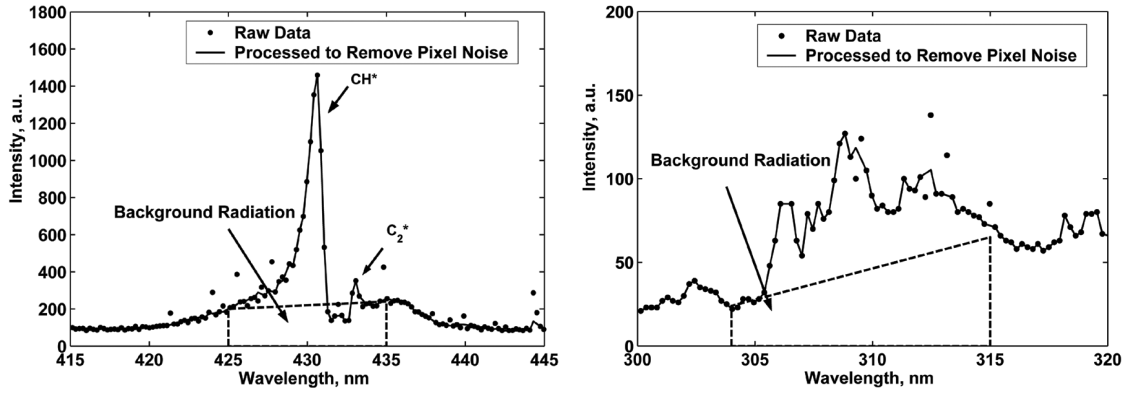

Figure 58. Measured spectrum and estimated background radiation for the (a) 430+/-5nm range and (b) 309+/-5nm range

from 435nm to 445nm, respectively. The CH* chemiluminescence intensity is computed by subtracting the total and background intensities. Figure 58(b) shows the 309+/-5nm wavelength range, which contains the OH* chemiluminescence intensity. The total intensity in this range is calculated by integrating the spectrum profile from 304nm to 314nm, and the background radiation is estimated as the area of the trapezoid drawn in the plot, where the heights of the top left and top right corners are the average intensities from 299nm to 304nm and from 314nm to 319nm, respectively. Note that the intensity in the 309+/-5nm range is relatively lower and, thus, noisier than the data in the 430+/-5nm range. This integration procedure was applied to the spectra at incremental axial locations along the test section to the produce axial profiles of total, background, and chemiluminescence (CH* and OH*) intensity.

A correction was applied to the chemiluminescence intensity profiles after baseline intensity subtraction at axial locations upstream of the H_2 injection tube outlet (5.1cm). The H_2 tube reduced the spectrometer optical path length by approximately 42%. It was assumed that reactions were uniform along the test section cross-section.

Thus, to correct for the H_2 tube obstruction, the intensity measured at positions upstream of 5.1cm was divided by 0.42.

8.2 The Combustion Zone Characteristics

The position and shape of the PAC combustion zone was described using a set of 'combustion zone characteristics', which were computed using the measured total and chemiluminescence intensity profiles in the 430+/-5nm range only. These characteristics were used to quantify the effects of ϕ_2 and trigger addition on the combustion process. This section defines the combustion zone characteristics and illustrates them using the preliminary intensity measurements from Section 5.2.

Axial intensity profiles were first shown in Figure 29 for the prime stage investigation. The images were taken through a single window, which showed only a small portion of the combustion zone. It was postulated that the intensity profile would continue to increase axially and then decrease to zero, thus delineating the entire combustion zone. Figure 59(a) shows the intensity data from Figure 29(c) together with a guessed intensity profile along the unseen length of the combustion zone. Note that the guessed profile was drawn to highlight certain combustion zone properties that were observed in the PAC experiments. For instance, the profile is asymmetric with a tail extending in the downstream direction.

Figure 59(b) shows the combustion zone characteristics for the guessed intensity profile. The characteristics can be divided into the two categories of 'location' and 'shape' parameters based on how they are computed. The location parameters are the position of 5% and 95% cumulative axial intensity and the position of maximum

intensity, termed $X_{5\%}$, $X_{95\%}$ and X_{MAX}, respectively. $X_{5\%}$ and $X_{95\%}$ were used to the denote the beginning and end of the combustion zone. Thus, the length of the combustion zone, termed L_{comb}, was defined as the difference between $X_{5\%}$ and $X_{95\%}$. The shape parameters consisted of the mean location, standard deviation, and skewness, termed X_M, STD and SK, respectively. As their names imply, the shape parameters were computed by treating the axial intensity profile, after scaling by its total area, as if it were a continuous probability distribution function. They were named using capital letters to distinguish them from the mean, standard deviation and skewness of actual statistical distributions, which are typically represented by the Greek letters such as μ, σ and γ. Denoting x as the axial distance from the propane tube outlets and $I(x)$ as the continuous axial intensity profile, the expressions for the shape parameters are defined as follows:

$$f_I = \frac{I(x)}{\int_0^\infty I(x)\,dx} \tag{8.1}$$

$$X_M = \int_0^\infty x\, f_I(x)\,dx \tag{8.2}$$

$$STD = \sqrt{\int_0^\infty (x - X_M)^2 f_I\ dx} \tag{8.3}$$

$$SK = \frac{1}{STD^3}\int_0^\infty \left(x - X_M\right)^3 f_I\,dx \tag{8.4}$$

X_M indicates the location about which the combustion zone intensity is concentrated. STD indicates the 'compactness' of the combustion zone. It is similar to L_{comb}, but

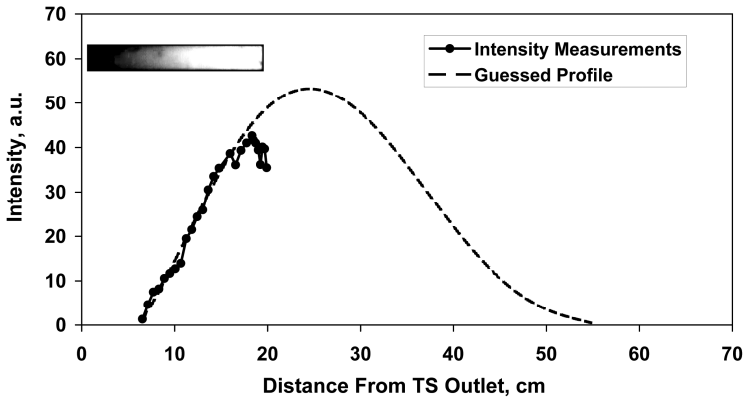

(a)

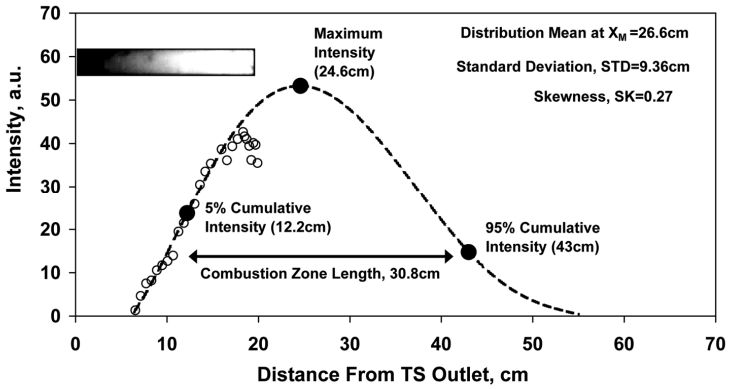

(b)

Figure 59. Intensity measurements from Figure 29(c) with (a) the guessed complete axial intensity profile and (b) the guessed profile and the combustion zone characteristics.

conveys unique information about the combustion zone when the intensity profile is highly asymmetric. *SK* indicates the asymmetry of the profile. It is greatly affected by the use of a trigger, as will be shown subsequently.

8.3 Analysis of Gas Composition and Combustion Efficiency

The gas analyzer data and the measured fuel and air flow rates were used to study the gas composition and combustion efficiency at the outlet of the test section (where the gas samples were drawn). This section describes the expressions used to predict the PAC product composition and to process the gas analyzer measurements.

The predicted gas composition was computed from the measured fuel and air flow rates by assuming the following global reaction mechanism (valid for $(\phi_G \le 1)$:

$$\phi_G\, C_{x'}H_{y'} + a'(O_2 + 3.76N_2) \rightarrow a'(1-\phi_G)O_2 + \phi_G\, x'CO_2 + \phi_G \frac{y'}{2} H_2O + a'3.76\, N_2 \quad (8.5)$$

where ϕ_G is the global equivalence ratio of the PAC, as defined below; $C_{x'}H_{y'}$ is a composite fuel based on the proportion of methane, propane and H_2 flow rates; x' and y' are the number of carbon and hydrogen atoms in a $C_{x'}H_{y'}$ molecule, respectively; and a' is the number of O_2 moles needed for complete combustion of one $C_{x'}H_{y'}$ mole. x', y' and a' are defined by the following equations:

$$f_i = \frac{\dot{n}_i}{\dot{n}_{CH_4} + \dot{n}_{C_3H_8} + \dot{n}_{H_2}} \quad (8.6)$$

$$x' = \sum_i x_i f_i \quad (8.7)$$

$$y' = \sum_i y_i f_i \quad (8.8)$$

$$a' = x' + \frac{y'}{4} \quad (8.9)$$

where the subscript i corresponds to each fuel; $\dot{n}_i$ is the measured flow rate of fuel i in moles per second; and x_i and y_i are the number of carbon and hydrogen atoms in fuel i, respectively. ϕ_G is computed using the following expression:

$$\phi_G = \left[\frac{\dot{m}_{fuel,total}}{\dot{m}_{air}}\right] \Big/ \left[\frac{MW_{C_{x'}H_{y'}}}{a'MW_{air}}\right] \quad (8.10)$$

where $\dot{m}_{fuel,total}$ is the sum of the measured methane, propane and H_2 flow rates; $\dot{m}_{air}$ is the measured air flow rate; MW_{air} is the molecular weight of air; and $MW_{C_xH_y}$ is the molecular weight of $C_{x'}H_{y'}$, equal to $(12x' + y')$. With ϕ_G known from the flow measurements, Equation (8.5) can be used to predict the product O_2 and CO_2 mole fractions, termed χ_{O_2} and χ_{CO_2}, respectively:

$$\chi_{O_2} = \frac{a'(1-\phi_G)}{a'(1-\phi_G) + \phi_G x' + \phi_G {y'}/{2} + a'3.76} \tag{8.11}$$

$$\chi_{CO_2} = \frac{\phi_G x'}{a'(1-\phi_G) + \phi_G x' + \phi_G {y'}/{2} + a'3.76} \tag{8.12}$$

The Horiba gas analyzer measures the 'dry' χ_{O_2} and χ_{CO_2}, since it removes the water vapor from the gas sample prior to measuring the composition. Equation (8.11) and Equation (8.12) can be used to predict $\chi_{O_2,dry}$ and $\chi_{CO_2,dry}$ simply by setting $y' = 0$.

The gas analyzer measurements of $\chi_{O_2,dry}$ and $\chi_{CO_2,dry}$ can be compared either to their predicted values or to the value of ϕ_G computed using Equation (8.10). The latter involves the formulation of equivalence ratio values based on χ_{O_2}, termed $\phi_{[O_2]}$, and based on χ_{CO_2}, termed $\phi_{[CO_2]}$. The following expressions for $\phi_{[O_2]}$ and $\phi_{[CO_2]}$ were derived by inverting Equation (8.11) and Equation (8.12), respectively:

$$\phi_{[O_2]} = \frac{a'(1 - 4.76\chi_{O_2})}{a' + \chi_{O_2}(x' + y'/2 - a')} \tag{8.13}$$

$$\phi_{[CO_2]} = \frac{4.76a'\chi_{CO_2}}{x' - \chi_{CO_2}(x' + y'/2 - a')} \tag{8.14}$$

By setting $y' = 0$, the measured values of $\chi_{O_2,dry}$ and $\chi_{CO_2,dry}$ can be input into the above equations to yield $\phi_{[O_2],dry}$ and $\phi_{[CO_2],dry}$. When there is complete combustion by the test section outlet, the values of $\phi_{[O2],dry}$ and $\phi_{[CO2],dry}$ are approximately equal to each other and to ϕ_G.

Finally, the combustion efficiency, η, at the test section outlet was approximated as $\eta_{[O_2]} = \phi_{[O_2],dry} / \phi_G$ and $\eta_{[CO_2]} = \phi_{[CO_2],dry} / \phi_G$, respectively. Recall that one of the goals of the trigger mechanism is to increase η. Thus, the trends in $\eta_{[O_2]}$ and $\eta_{[CO_2]}$ were used to quantify the performance of the H_2 trigger in the PAC.

8.4 Experimental Results: Autoignition without a Trigger

The first set of results, termed Set 1, consists of four baseline cases of propane autoignition without a trigger. Table 4 lists the operating points for the four cases. They consist of primary combustion at about $\phi_1 \approx 0.77$ and propane/vitiated-air autoignition at varying values of ϕ_2. Results are presented for the 430+/-5nm wavelength range only, because the intensity in the 309+/-5nm wavelength range was very low for these cases.

Figure 60(a) shows the total intensity profiles measured by the spectrometer. The intensity is initially between 100 and 200 a.u. and then drops at 5.1 cm. This 'intensity defect' was caused by higher levels of background radiation from the H_2 injection tube

Table 4. Set 1 (Cases 1-4) operating points.

Case	Temperature, K	ϕ_1	ϕ_2	ϕ_G
1	1512	0.76	0.41	0.86
2	1512	0.77	0.56	0.90
3	1522	0.77	0.69	0.93
4	1522	0.77	0.82	0.96

relative to the ceramic walls, as discussed shortly. Note that this higher background radiation is visible in Figure 13(a). Aside from this small defect, the total intensity profiles are parabolic in nature. They increase to maximum values located at 13.34 cm for Case 1 and about 17.15 cm for Cases 2 through 4 and then decrease up to the test section outlet. For Case 1, the total intensity dropped slightly below zero at the end of the test section. This negative intensity was caused by a small drift in the spectrometer's baseline intensity away from the previously recorded dark spectrum baseline intensity, which was used to zero the data. The measured profiles clearly show that the combustion zone shifted downstream as ϕ_2 was increased. This downstream shift occurred primarily from Case 1 to Case 2, and to a lesser extent from Case 2 up to Case 4.

The effect of ϕ_2 on the combustion zone was quantified using the combustion zone characteristics defined in Section 8.2. Table 5 lists the combustion zone characteristics computed from the total intensity (430+-5nm) profiles. Note that the intensity defect from the H_2 tube was excluded from these calculations of the characteristics by neglecting the data upstream of 5.1 cm. This was assumed to have little effect, since the total intensity is relatively low upstream of 5.1cm. $X_{5\%}$, $X_{95\%}$ and L_{comb} show that the combustion zone generally shifts downstream and lengthens as ϕ_2 increases. For example, $X_{5\%}$ is 7.49 cm for Case 1 and increases to 8.76 cm. 9.65 cm and 9.39 cm for Cases 2 to 4, respectively. This is consistent with the Chemkin results, which showed that $t_{ign,n.t.}$ increases with $\phi_{surr.fuel}$ for autoignition in vitiated-air$_{(0.75)}$, see Figure 42. X_M increases from 14.63 cm for Case 1 to 16.68 cm, 17.44 cm and 17.86 cm for

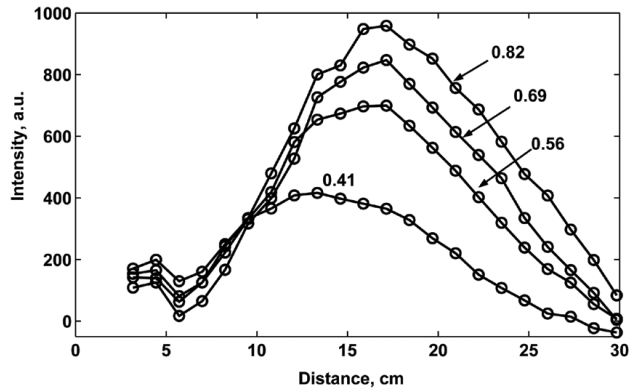

(a)

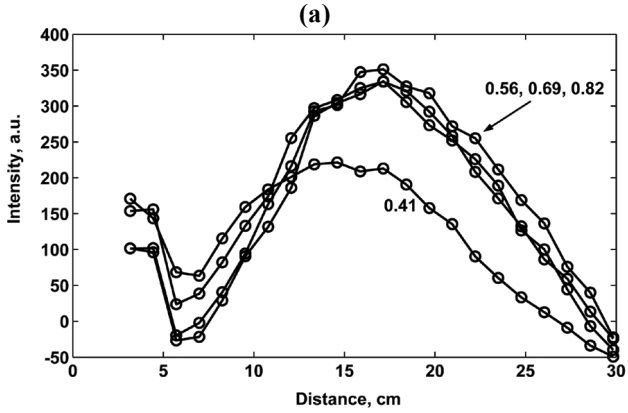

(b)

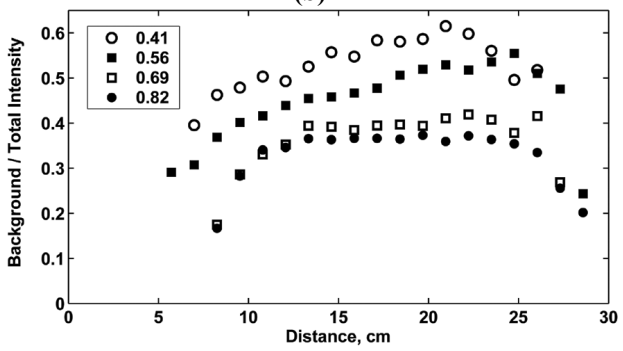

(c)

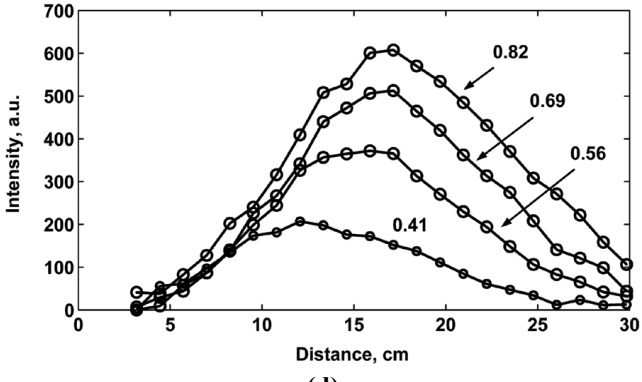

(d)

Figure 60. Results from Set 1 (430+/-5nm): (a) total intensity; (b) background intensity; (c) the ratio of background to total intensity; and (d)CH* chemiluminescence intensity.

Cases 3 to 4, respectively. Thus, the region with highest intensity (indicative of highest heat release) shifts downstream together with the beginning and end of the combustion zone. STD shows that the combustion zone generally widens (becomes less compact) as ϕ_2 increases. Finally, SK shows no significant trends with ϕ_2. Its values are very low relative to SK for cases with the H_2 trigger, which are presented shortly. Thus, the total intensity profiles without the trigger are relatively symmetric about X_M.

Figure 60(b) shows the Set 1 profiles of background radiation intensity (430+/-5nm). The background intensity profiles are similar to the total intensity profiles shown in Figure 60(a). They include the same intensity defect upstream of 5.1 cm, which confirms that it was caused by background radiation from the H_2 tube. They also reach maximum intensities at nearly the same positions as the total intensity profiles, see X_{MAX} in Table 5. This similarity between the total and background profiles has important consequences for the AF experiments, as discussed in Section 8.6.

Figure 60(c) shows profiles of the ratio of background to total intensity (430+/-5nm) for Set 1. The first few and last few points on each profile should be neglected, because the low intensity measured at those locations causes the ratio to drop to zero or jump to very high values (not shown). The ratio values are approximately 0.35 for Cases 3 and 4, 0.45 for Case 2, and 0.55 for Case 1. Thus, the contribution of background

Table 5. Set 1 combustion zone characteristics based on total intensity profiles (430+/-5nm). The data upstream of the H_2 tube outlet (5.1cm) were excluded.

Case	X_{MAX}, cm	X_M, cm	STD, cm	SK	$X_{5\%}$, cm	$X_{95\%}$, cm	L_{comb}, cm
1	13.34	14.63	4.51	0.06	7.49	22.53	15.04
2	17.15	16.68	4.98	0.17	8.76	25.35	16.59
3	17.15	17.44	4.86	0.13	9.65	25.80	16.15
4	17.15	17.86	5.23	0.07	9.39	26.76	17.37

radiation decreases as ϕ_2 increases. Clearly, background radiation is a large fraction of the measured total intensity. As such, it could potentially alter the 'location' and 'shape' of the combustion zone, as computed using the total intensity profiles. However, Figure 60(c) shows that the ratio profiles are approximately constant or increase with only a shallow slope along the test section length. This confirms that the background and total intensity profiles exhibit similar axial trends, as mentioned above. Importantly, the nearly constant ratio values also indicate that background radiation does not greatly affect the values of the location and shape parameters, since the intensity profiles are normalized before computing them.

Figure 60(d) shows the Set 1 CH* chemiluminescence intensity profiles, and Table 6 lists the combustion zone characteristics computed from those profiles. The CH* chemiluminescence intensity profiles are relatively smooth throughout the entire combustion zone. Clearly, the subtraction of background radiation from total intensity removed both the intensity defect upstream of 5.1 cm and the negative intensity from the drifting spectrometer baseline. The values of the location and shape parameters are slightly different than those computed from the total intensity profiles. For instance, the values of STD and L_{comb} suggest a slightly longer combustion zone. Nevertheless, the trends are the same - the location and shape parameters indicate a downstream shift and widening of combustion zone with an increase in ϕ_2. The trends exhibited by the CH*

Table 6. Set 1 combustion zone characteristics based on CH* chemiluminescence profiles.

Case	X_{MAX}, cm	X_M, cm	STD, cm	SK	$X_{5\%}$, cm	$X_{95\%}$, cm	L_{comb}, cm
1	12.07	14.18	5.29	0.38	6.11	23.60	17.49
2	15.88	16.24	5.22	0.23	8.04	25.54	17.50
3	17.15	17.17	5.31	0.08	8.63	26.39	17.76
4	17.15	17.60	5.67	-0.02	8.17	27.13	18.96

chemiluminescence and total intensity profiles are the same because of the similarity between the background and total intensity profiles, or, rather, because of the similarity between the background and CH* chemiluminescence intensity profiles. As a result, either the total or CH* chemiluminescence intensity profiles could be used to analyze the combustion zone. The advantage of using the CH* chemiluminescence intensity profiles is that they provide better qualitative representations of the combustion zone, since they exclude the intensity defect, are smoother, begin at zero, and do not drop below zero.

Finally, Table 7 lists the Set 1 gas composition measurements and predictions. For Case 1, $\phi_{[O_2],dry} = \phi_{[CO_2],dry}$ and $\eta = 0.98$. Thus, the results suggest nearly complete combustion for Case 1. However, the values of $\phi_{[O_2],dry}$, $\phi_{[CO_2],dry}$ and ϕ_G begin to differ as ϕ_2 increases from Case 1 to Case 4. For Case 4, $\phi_{[O2],dry} = 0.93$ and $\phi_{[CO2],dry} = 0.89$, which corresponds to $\eta_{[O_2]}$=0.97 and $\eta_{[CO_2]}$=0.93, respectively. The low $\eta_{[CO_2]}$ values suggest that there is appreciable CO present in the gas sample. The general decrease in both values of η is consistent with the intensity measurements, which showed that the intensity at the test section outlet (gas sampling probe inlet) increased from zero for Case 1 to about 150 a.u. for Case 4 (25% of Case 4 maximum intensity), see Figure 60(d). Without the composition measurements, the increase in intensity at the test section outlet alone would suggest incomplete combustion. The gas analyzer verified this and showed

Table 7. Set 1 gas composition predictions and measurements.

Case	Predicted		Measured		$\phi_{[O_2],dry}$ ($\eta_{[O_2]}$)	$\phi_{[CO_2],dry}$ ($\eta_{[CO_2]}$)	ϕ_G
	χ_{O_2}	χ_{CO_2}	χ_{O_2}	χ_{CO_2}			
1	3.26	10.11	3.67	9.82	0.84 *(0.98)*	0.84 *(0.98)*	0.86
2	2.32	10.70	2.63	10.38	0.89 *(0.99)*	0.88 *(0.98)*	0.90
3	1.62	11.16	2.18	10.57	0.91 *(0.98)*	0.89 *(0.96)*	0.93
4	0.94	11.60	1.67	10.71	0.93 *(0.97)*	0.89 *(0.93)*	0.96

that even low values of intensity at the outlet correlate with η values significantly below unity. This conclusion was used to help interpret the AF measurements, as discussed in Section 8.6.

8.5 Experimental Results: Combustion with the H_2 Trigger

The measurements of combustion with the H_2 trigger are presented in two sets, termed Set 2 and Set 3. Each set consists of several cases with fixed values of both ϕ_1 and ϕ_2 but varying values of H_2 PR_G. Intensity profiles in the 430+/-5nm range are shown for both sets of results. The combustion zone characteristics based on those profiles are computed and compared to quantify the effect of the H_2 trigger. For Set 1, the OH* chemiluminescence intensity profiles are also presented and used to study the H_2 combustion process separately from the propane combustion process.

Set 2 Results: 430+/-5nm Range

The Set 2 operating points are listed in Table 8. Each case has ϕ_1 of 0.77 and ϕ_2 of 0.56, which are the same values as Case 2 in Set 1. Two values of ϕ_G are listed in the table: ϕ_{G,noH_2} is the global equivalence ratio prior to H_2 addition and ϕ_G is the global equivalence ratio after H_2 addition at the specified value of PR_G. It should be noted that the Case 6 PR_G of 8% is an estimate, because for this case the pressures upstream of

Table 8. Set 2 (Cases 5-8) operating points.

Case	Temperature, K	ϕ_1	ϕ_2	ϕ_{G,noH_2}	PR_G,%	ϕ_G
5	1512.00	0.77	0.56	0.90	0	0.90
6	1512.00	0.77	0.56	0.90	~8	0.91
7	1512.00	0.77	0.56	0.90	11	0.91
8	1512.00	0.77	0.56	0.90	17	0.92

several fuel metering orifices were just under choking conditions.

Figure 61(a) shows the total intensity profiles for Set 2. The Case 5 profile corresponds to autoignition without the H_2 trigger. Note that this is the same data as Case 2 in Set 1, see Figure 60(a). Again, it shows that the combustion zone with no trigger produces a relatively symmetric total intensity profile centered at about 17 cm for this case. The profiles for Cases 6-8 show the effect of H_2 injection. For these cases, the intensity increases sharply at the H_2 tube outlets (5.1cm), and then decreases to zero farther upstream than the Case 5 profile. Thus, the H_2 gas 'triggered' propane combustion process and reduced the length of the combustion zone, as desired. The Case 7 ($PR_G = 11\%$) profile has higher spatial resolution in the vicinity of the H_2 tube outlet and, thus, confirms that the sharp increase in intensity occurred only downstream of 5.1 cm.

Table 9 lists the combustion zone characteristics for the Set 2 total intensity profiles. As for the Set 1 total intensity analysis, the data points upstream of 5.1 cm were excluded from the shape and location parameter expressions. The location parameters show that the combustion zone shifts upstream as PR_G increases. For example, $X_{95\%}$ shifts from 25.35 cm for Case 5 (no trigger) to 22.68 cm, 22.70 cm, and 21.42 cm for Cases 6, 7 and 8, respectively. Thus, the combustion process is complete well before the outlet of the test section (30 cm) for all cases. X_M exhibits the same trend, thus indicating that the region of bulk heat release also shifts upstream. The length of the combustion zone, as quantified by L_{comb} and STD, generally decreases from Case 5 to Case 8. This suggests that the H_2 trigger also increased the rate toward complete combustion. Finally, SK indicates that as PR_G increases the combustion zone becomes highly asymmetric and is concentrated closer to the H_2 tube outlet.

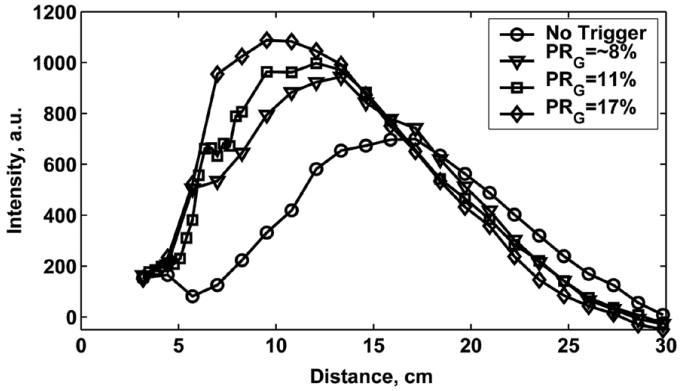

(a)

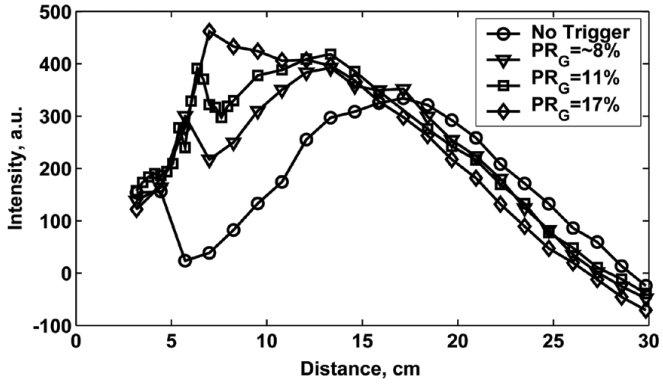

(b)

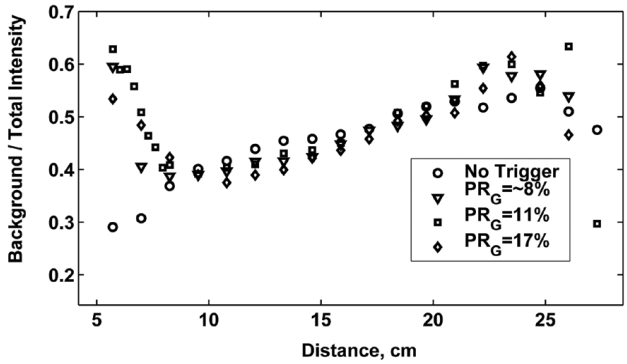

(c)

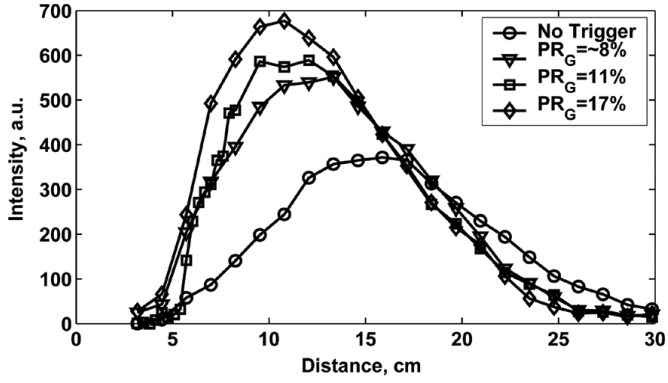

(d)

Figure 61. Results from Set 2 (430+/-5nm): (a) total intensity; (b) background intensity; (c) the ratio of background to total intensity; and (d)CH* chemiluminescence intensity.

Table 9. Set 2 combustion zone characteristics based on total intensity profiles (430+/-5nm). The data upstream of the H_2 tube outlet (5.1cm) were excluded.

Case	X_{MAX} , cm	X_M , cm	STD , cm	SK	$X_{5\%}$, cm	$X_{95\%}$, cm	L_{comb} , cm
5	17.15	16.68	4.98	0.17	8.76	25.35	16.59
6	13.34	14.16	4.78	0.30	6.90	22.68	15.78
7	12.07	13.66	4.91	0.44	6.52	22.70	16.18
8	9.53	13.02	4.50	0.41	6.70	21.42	14.72

Figure 61(b) shows the Set 2 background radiation intensity profiles (430+/-5nm). The profiles show that background radiation increases with PR_G. This is likely caused by the increase in temperature in the vicinity of the H_2 tube outlet, which causes local increases in CO_2* chemiluminescence intensity and thermal radiation from the ceramics and H_2 injection tube.

Figure 61(c) shows the ratio of background to total intensity (430+/-5nm) for each Case in Set 2. Interestingly, the intensity ratio profiles nearly overlap for combustion with and without a trigger. They show that background radiation was the source of about 40-50% of the total measured intensity. The profiles are not exactly constant along the length of the test section; they have a slightly positive slope. As a result, the values of the location and shape parameters calculated from CH* chemiluminescence intensity differed slightly from those calculated from total intensity, as shown below. However, the trends were the same because the intensity ratio profiles are linear.

Figure 61(d) shows the Set 2 profiles of CH* chemiluminescence intensity. As for Set 1, the intensity defect upstream of 5.1 cm and the negative intensity toward the end of the combustion zone are not present. The profiles increase smoothly to a maximum and drop to zero near the end of the test section. The combustion zone characteristics for the CH* chemiluminescence intensity profiles are listed in Table 10. As expected, the values show nearly the same trends as discussed above for the total intensity profiles. Namely,

Table 10. Set 2 combustion zone characteristics based on CH* chemiluminescence profiles.

Case	X_{MAX}, cm	X_M, cm	STD, cm	SK	$X_{5\%}$, cm	$X_{95\%}$, cm	L_{comb}, cm
5	15.88	16.24	5.22	0.23	8.04	25.54	17.50
6	13.34	13.68	4.94	0.45	6.37	22.48	16.11
7	12.07	13.50	4.75	0.65	6.90	22.39	15.49
8	10.80	12.75	4.73	0.64	6.20	21.36	15.16

that the combustion zone shifts upstream and decreases in length with the addition of the H_2 trigger. Moreover, the trends are more consistent across all the cases, as opposed to some of the characteristics in Table 9. This shows that there is also a quantitative advantage to using the relatively 'smoother' CH* chemiluminescence intensity profiles even though the conclusions from the total intensity profiles are generally the same.

Finally, Table 11 lists the gas composition measurements and predictions for Set 2. For all cases, $\phi_{[CO_2]}$, $\phi_{[O_2]}$ and ϕ_G are in close agreement, which indicates nearly complete combustion. For example, $\eta_{[CO_2]}$ is 0.97 or 0.98 for all cases and $\eta_{[O_2]}$ is 0.99 for all cases. Since the intensity profiles all drop to zero upstream of the test section outlet, these results support the previous observation that zero intensity correlates with complete combustion.

Set 2 Results: 309+/-5nm Range

Propane combustion at the PAC operating conditions produces little OH*

Table 11. Set 2 (Cases 5-8) gas composition predictions and measurements

Case	Predicted		Measured		$\phi_{[O_2],dry}$ ($\eta_{[O_2]}$)	$\phi_{[CO_2],dry}$ ($\eta_{[CO_2]}$)	ϕ_G
	χ_{O_2}	χ_{CO_2}	χ_{O_2}	χ_{CO_2}			
5	2.32	10.70	2.63	10.38	0.89 *(0.99)*	0.88 *(0.98)*	0.90
6	2.16	10.70	2.55	10.37	0.89 *(0.99)*	0.88 *(0.97)*	0.91
7	2.12	10.69	2.37	10.55	0.89 *(0.99)*	0.89 *(0.98)*	0.91
8	1.90	10.74	2.12	10.42	0.91 *(0.99)*	0.89 *(0.97)*	0.92

chemiluminescence intensity relative to CH* chemiluminescence intensity. In contrast, the reaction of the H_2 trigger produces significant OH* chemiluminescence intensity. Consequently, the measured profiles of OH* chemiluminescence intensity were used to distinguish the H_2 combustion process from the propane combustion process. This distinction provided the opportunity to study the role of the H_2 trigger in the PAC.

Figure 62(a) shows the Set 2 OH* chemiluminescence intensity profiles. The Case 5 profile confirms that OH* chemiluminescence was relatively weak when there was no H_2 injection (for refrence, the Case 5 CH* chemiluminescence intensity profile has a maximum value of 400 a.u.). The profiles for Cases 6-8 show that H_2 injection produced an immediate spike in OH* chemiluminescence intensity whose maximum value increased slightly with PR_G. Downstream of the spike, the OH* chemiluminescence intensity relaxed to somewhat of a plateau and then dropped steadily to zero. Note that the rapid spike in OH* chemiluminescence intensity was expected based on the Chemkin simulations, which indicated that the H_2 trigger chemistry begins immediately after injection, see Section 7.3.

Figure 62(b) shows the OH* chemiluminescence intensity profiles for Case 7 and a 'H_2-only' case, which was Case 7 with the propane valve closed during operation. The

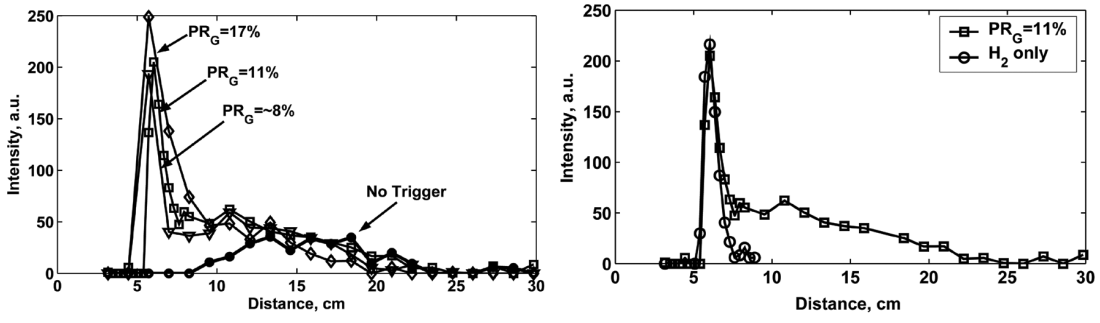

Figure 62. Set 2 (Cases 5-8) OH* chemiluminescence intensity profiles: (a) Cases 5-8 and (b) Case 7 and the H_2-only case.

H_2-only intensity profile almost exactly overlaps with the spike portion of the Case 7 profile. However, it drops to zero while the Case 7 profile continues into the plateau and slow decline. This suggests that for all cases the H_2 was rapidly consumed within about 3 cm from the H_2 tube outlet. Within this short distance, the H_2 was able to 'trigger' the propane combustion process and, thus, cause the entire combustion zone to shift upstream. Note from Figure 62(a) that downstream of the spike the Case 6, 7 and 8 OH* chemiluminescence intensity profiles all resemble the second half of the Case 5 profile shifted upstream by about 7 cm. This suggests that the downstream half of the combustion process proceeded to completion at the same rate regardless of H_2 injection.

Set 3 Results

The final set of measurements, termed Set 3, investigates the effect of the H_2 trigger at higher values of ϕ_2 than Set 2. The Set 3 operating conditions are listed in Table 12. Note that Case 9, the no trigger case, is the same as Case 4 in Set 1. For brevity, the plot of background to total intensity ratio (430+/-5nm) is not shown. As in Set 2, the intensity ratios are the same for combustion with and without a trigger and, thus, follow the Case 4 profile shown in Figure 60(c). Results are shown only for the 430+/-5nm range.

Figure 63 shows the Set 3 total and CH* chemiluminescence intensity profiles. As in Set 2, the intensity increases immediately after H_2 injection, and the combustion zone

Table 12. Set 3 (Cases 9-11) operating points.

Case	Temperature, K	ϕ_1	ϕ_2	$\phi_{G,no\,H_2}$	PR_G,%	ϕ_G
9	1522	0.77	0.82	0.96	x	0.96
10	1522	0.77	0.824	0.959	10	0.98
11	1522	0.77	0.833	0.962	17	0.99

shifts upstream. However, in contrast to Set 2 there is almost no difference between the 11% and 17% PR_G cases. These effects are quantified by the combustion zone characteristics listed in Table 13, which were computed using the CH* chemiluminescence intensity profiles. X_M, $X_{5\%}$ and $X_{95\%}$ all indicate that the H_2 trigger shifts the combustion zone upstream relative to Case 9. However, L_{comb} remains about the same and STD actually increases from 5.67 cm for Case 9 to about 5.75 cm for Cases 10 and 11. The values of the location and shape parameters are approximately the same for Case 10 and 11, which confirms that the corresponding increase in PR_G has little effect on the combustion process. This is an important result, because it indicates that there is a

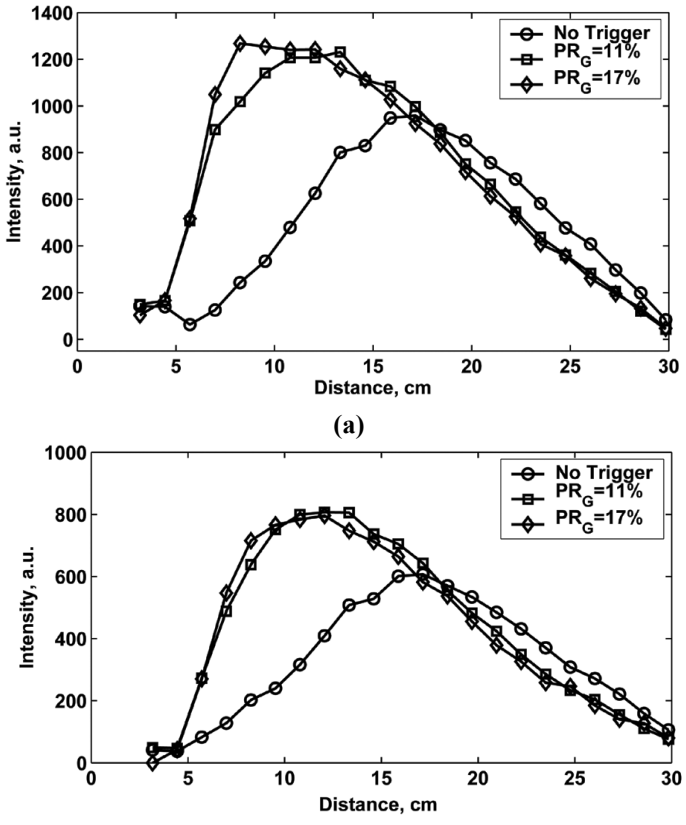

Figure 63. Set 3 (Cases 9-11) intensity profiles (430+/-5nm): (a) total intensity and (b) CH* chemiluminescence intensity

Table 13. Set 3 (Cases 9-11) combustion zone characteristics based on the CH* chemiluminescence intensity profiles.

Case	X_{MAX} , cm	X_{M} , cm	STD , cm	SK	$X_{5\%}$, cm	$X_{95\%}$, cm	L_{comb} , cm
9	17.15	17.60	5.67	-0.02	8.17	27.13	18.96
10	12.07	14.91	5.73	0.43	6.69	25.61	18.92
11	12.07	14.74	5.78	0.49	6.70	25.62	18.92

limit to the effect of the trigger gas. This limited return is consistent with Chemkin simulations, which showed that the *reduction* in ignition delay time (expressed as t_{ign} or $[\Delta t]^{*}_{n.t.}$) tapered toward a constant value as PR_G increased to its maximum value, see Figure 49.

Lastly, Table 14 lists the predicted and measured gas composition for Set 3. The values of $\eta_{[CO_2]}$ are unaffected by the H_2 trigger and suggest incomplete combustion for all cases. This was expected since none of the intensity profiles dropped to zero upstream of the test section outlet. On the other hand, the values of $\eta_{[O_2]}$ increased toward 1.0 as PR_G increased. This was likely due to the complete combustion of the H_2, which consumed its entire share of O_2 without producing any CO. Note that the relatively constant value of $\eta_{[CO_2]}$ despite H_2 trigger addition does not indicate that the trigger had no effect. For these cases the trigger fulfilled only part of its purpose. It was able to shift the combustion zone upstream and anchor it near the H_2 tube outlet, but it was unable to make it more compact or to increase the combustion efficiency by the test section outlet.

Table 14. Set 3 (Cases 9-11) gas composition predictions and measurements

Case	Predicted		Measured		$\phi_{[O_2],dry}$ (η_{c,o_2})	$\phi_{[CO_2],dry}$ (η_{c,co_2})	ϕ_G
	χ_{O_2}	χ_{CO_2}	χ_{O_2}	χ_{CO_2}			
9	0.94	11.60	1.67	10.71	0.93 *(0.97)*	0.89 *(0.93)*	0.96
10	0.57	11.64	0.99	10.69	0.96 *(0.98)*	0.90 *(0.92)*	0.98
11	0.25	11.70	0.34	10.61	0.99 *(1.0)*	0.91 *(0.92)*	0.99

8.6 Application of PAC Results to the AF Experiments

Some of the conclusions from the PAC experiments were used to help interpret the results from the AF experiments. The relevant conclusions involved two of the advantages of the PAC measurements over the AF measurements – the distinction between chemiluminescence intensity and total intensity and the measurement of both χ_{O_2} and χ_{CO_2}.

The camera and filter in the AF could not distinguish between background radiation and chemiluminescence. This raised the concern that the contribution of the background radiation resulted in location and shape parameters that inaccurately described the AF combustion zone. The PAC experiments revealed that background radiation is a significant fraction of the total intensity. However, the ratio of background to total intensity was approximately constant along the test section or linear with a shallow slope. As a result, the total and chemiluminescence intensity profiles provided combustion zone characteristics with similar values and trends. Since the PAC was designed to mimic the AF sources of background radiation, the observed relationship between total and chemiluminescence intensity was assumed to apply to the AF measurements as well. Thus, the PAC experiments suggest that the AF total intensity profiles accurately portrayed the combustion zone.

The AF gas composition measurements were limited to χ_{O_2} only, which were compared with predicted values and used to estimate η at the AF outlet. However, the PAC results showed that χ_{O_2} alone cannot be used to determine η since it consistently indicated higher values ($\eta_{[O_2]}$) than χ_{CO_2} ($\eta_{[CO_2]}$). The PAC results also showed that there

is complete combustion only if the intensity drops completely to zero. Even weak intensity at the test section outlet indicated a significant drop in η_c. This knowledge was used to check the conclusions from the AF χ_{O_2} measurements. If the intensity profiles did not drop to zero by the AF outlet, then η_c was likely less than unity even if the O_2 sensor indicated nearly complete combustion.

CHAPTER 9 AF EXPERIMENTS

This chapter describes the AF experiments for the trigger stage investigation. These experiments were performed after the hardware modifications described in Chapter 2, which included the addition of an H_2 injector just downstream of the TS outlet, an O_2 sensor near the exhaust, additional quartz windows and a high-speed camera. Altogether, the AF with the H_2 trigger was the closest representation of the PAT concept in this study – simulating both the prime stage and the trigger stage at realistic turbine bulk flow temperatures, velocities, and gas compositions. The purpose of these AF experiments was to evaluate the effect of the H_2 trigger on the primed Jet-A/vitiated-air combustion process. Note that the Chemkin simulations (with surrogate fuel) and PAC experiments (with gaseous propane) already showed that the H_2 trigger can shift the combustion zone upstream, reduce its length and increase the combustion efficiency. The AF experiments re-evaluated those trigger effects at more realistic turbine engine conditions, where the combustion process depends on Jet-A evaporation, mixing, chemical kinetics and variable bulk flow properties. In addition, the AF experiments evaluated the effect of the H_2 trigger on combustion zone fluctuations.

This chapter proceeds as follows: the first section describes the method for processing the high-speed camera images; the second section describes the method for the analysis of combustion zone fluctuations; and the third section describes the results of the AF experiments.

9.1 Procedure for Processing the High-speed Camera Images

Continuous axial intensity profiles are needed to calculate the combustion zone characteristics, which were discussed in Section 8.2. However, the gaps between the AF windows (see Figure 10) segmented the images of the combustion zone into three sections. As a result, continuous axial intensity profiles were generated by fitting polynomial curves across the segmented intensity measurements. This section discusses the procedure used to process the high-speed camera images into the estimated, continuous intensity profiles. The procedure is demonstrated using several representative measured data sets.

Figure 64 shows camera images of the AF windows without the 430+/-5nm filter. The flow direction is from left to right. Thus, the left edge of the images is the outlet of the TS and the right edge is just upstream of the O_2 sensor sampling tube inlet. The direction normal to the flow, from top to bottom of the images, will be referred to as the spanwise direction. Note that the ceramic panels and several thermocouple ports (holes in

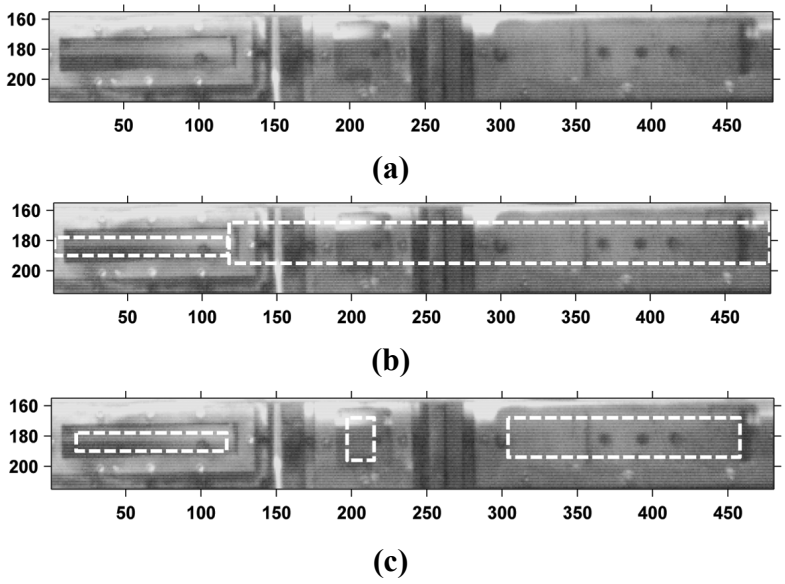

Figure 64. The diverging and afterburner sections as viewed by the camera with lights on and no filter: (a) raw image, (b) image with full-axis boxes, (c) image with sampling windows. The axes units are pixel number.

ceramic panels) are visible through the windows. Figure 64(b) shows the portion of the image - contained in the dashed boxes - that is processed to obtain an axial intensity profile. These dashed boxes are referred to as the 'full-axis boxes', and the data extracted from their domain are referred to as the 'full-axis data'. Figure 64(c) shows the portions of the full-axis boxes that exclude the spaces between the windows. These boxes are referred to as the 'sampling windows'. The sampling window data are simply a subset of the full-axis data and are used to generate the fitted continuous intensity profiles, as discussed shortly.

The following procedure was used to process each image recorded during experiments into an axial intensity profile:

1. The full image was input into Matlab, which assigns a numerical value to each pixel that corresponds to its grayscale intensity.
2. A spanwise average was applied to the pixels within the full-axis boxes to produce an axial grayscale intensity profile.
3. A 3-pixel moving average was applied to the axial intensity profile to reduce noise.
4. The baseline radiation was subtracted from the profile (see below).
5. The data outside the sampling windows range (in gaps between windows) were removed to produce a segmented intensity profile.
6. A polynomial curve from the TS outlet to the exhaust was fitted to the segmented sampling window data.

Through trial and error, it was found that a 6^{th} order polynomial provided the best fit to the sampling window data when the maximum intensity was less than 4 a.u., otherwise a

10^{th} order polynomial was necessary. Note that each pixel corresponds to approximately 1.27 mm, so the 3-pixel average (step 3) corresponds to about a 4 mm spatial average. The combustion zone is much longer than 4 mm, as will be shown, so this averaging procedure did not significantly change the intensity profile position or shape.

The first three steps of the above procedure were first applied to images of the facility without any afterburner combustion (cold flow) in order to obtain a baseline intensity profile. Figure 65 shows the results of the baseline intensity analysis. Figure 65(a) shows the cold flow intensity data from a single frame (1/60 sec exposure time) with the spanwise and 3-pixel average already applied. The small points represent the full-axis data and the larger open circles correspond to the sampling window data. The results show that the baseline radiation increases linearly in the flow direction from about 1 a.u. to 3 a.u. Figure 65(b) shows a 100 frame average (1.66 sec) of the cold flow intensity data. The solid line is the linear fit to the data, which will be referred to as the baseline intensity profile.

Figure 66 shows intensity data processed from images of the Jet-A combustion

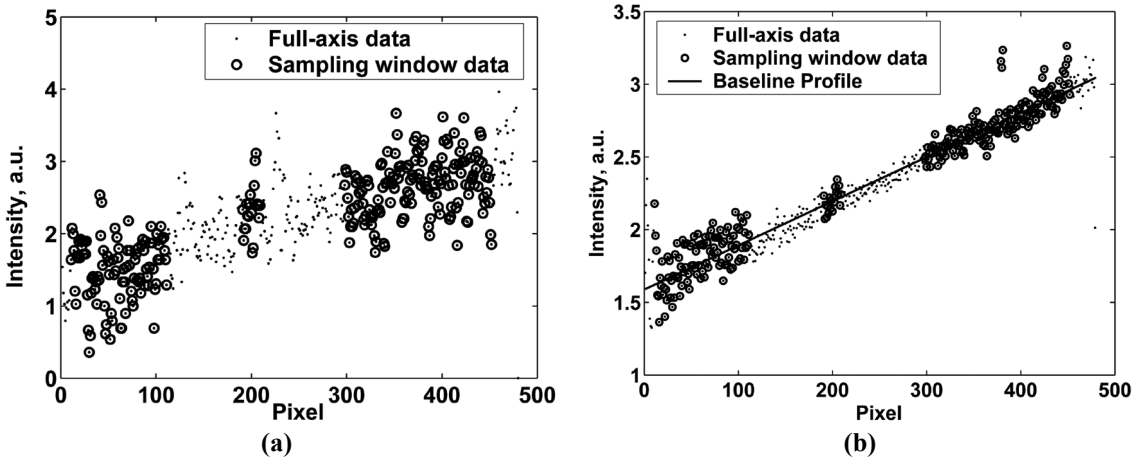

Figure 65. Profiles of cold flow baseline intensity with different degrees of image processing: (a) single frame profile with span-wise average and 3 pixel axial average, and (b) 100 frame average of profiles with span-wise average and 3-pixel axial average.

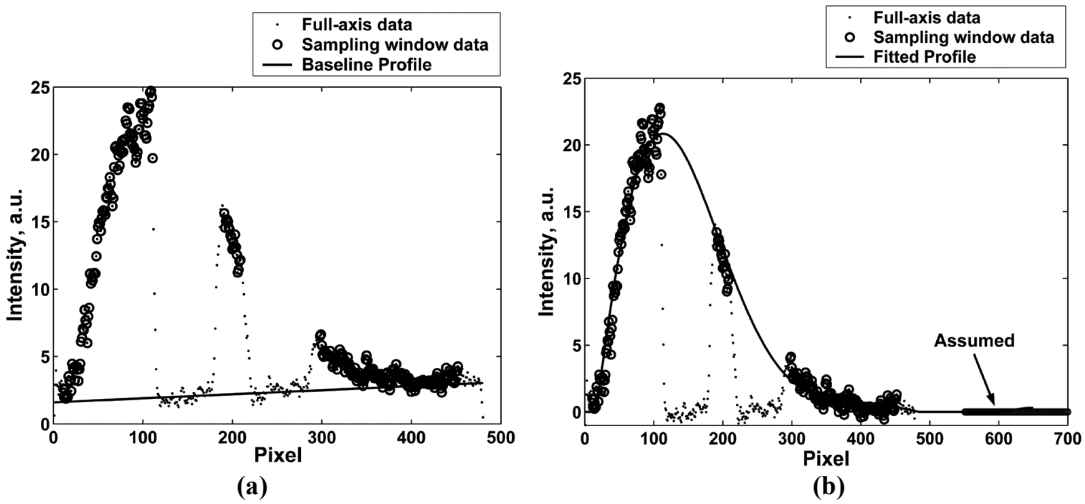

Figure 66. Example of a higher intensity single-frame profile of the combustion zone after the span-wise average and 3 pixel axial average: (a) before baseline intensity subtraction and (b) after baseline intensity subtraction.

zone. The data corresponds to a single frame (1/60 sec) after the spanwise and axial averaging procedure. Figure 66(a) shows the data before subtraction of baseline intensity. Again, the small points are the full-axis data, and the open circles are the sampling window data. The solid line is the baseline intensity profile, which was shown in Figure 65(b). Note that the full-axis data drops to the baseline intensity profile in the spaces between the windows. Due to edge effects, this drop is not discontinuous; instead, it occurs over about 7-pixels. Figure 66(b) shows the intensity data after baseline intensity subtraction. The profile fit of the sampling window data (10^{th} order polynomial) is also shown. An additional set of zero intensity points, labeled 'assumed', were added to the plot from pixels 550 to 750. These assumed zero intensity data points were added to help constrain the polynomial profile fit. Note that pixels 550 to 750 correspond to locations about 70 cm to 95 cm from the TS outlet, see Figure 10. For reference, the O_2 sensor sampling tube inlet is located at about 66cm.

Figure 67 shows data from a lower intensity combustion zone. Figure 67(a) and Figure 67(b) show the data before and after baseline intensity subtraction, respectively.

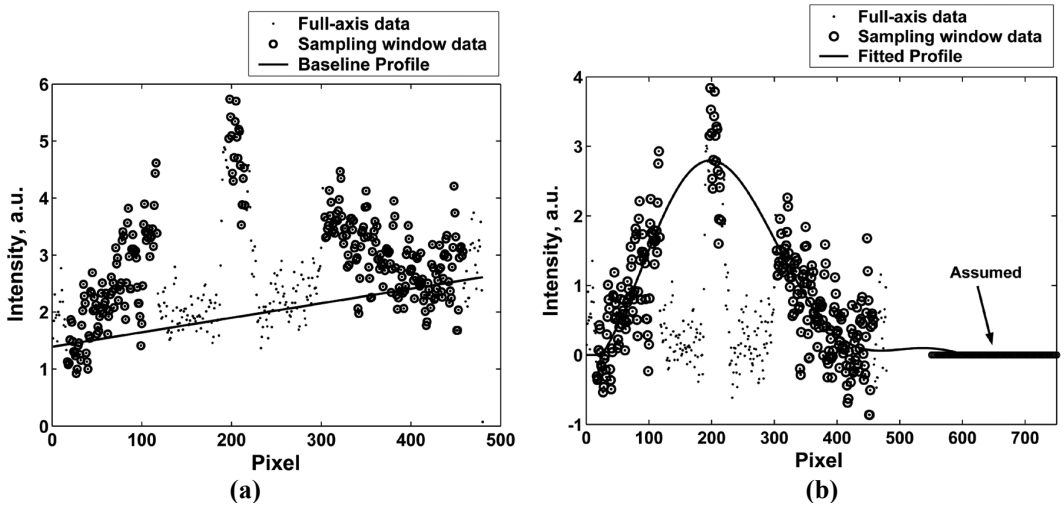

Figure 67. Example of a lower intensity single frame profile of the combustion zone after the span-wise average and 3 pixel axial average: (a) before baseline intensity subtraction and (b) after baseline intensity subtraction.

Figure 67(b) also shows the assumed data points and the fitted profile (6^{th} order polynomial). Despite the low intensity and scatter, the combustion zone is clearly discerned by the increase and decrease in the magnitudes of the measured intensity and fitted profile (a familiar trend from the PAC intensity measurements). Note that there is also a clear decrease in intensity in the gaps between the windows. This is evident in Figure 67(a), where the data between the windows drop to the baseline intensity profile and in Figure 67(b), where the data between the windows drop to zero.

As a final example, Figure 68 shows data for a low intensity case that has been averaged over 240 frames (4 sec average). The data demonstrate the reduced scatter of time-averaged, low intensity data as compared to the single frame, low intensity data shown in Figure 67. Again, the sampling window and fitted profile clearly show the rise and fall of intensity along the combustion zone length. Also, the data between the windows clearly follow the baseline intensity profile in Figure 68(a) and fall to zero in Figure 68(b).

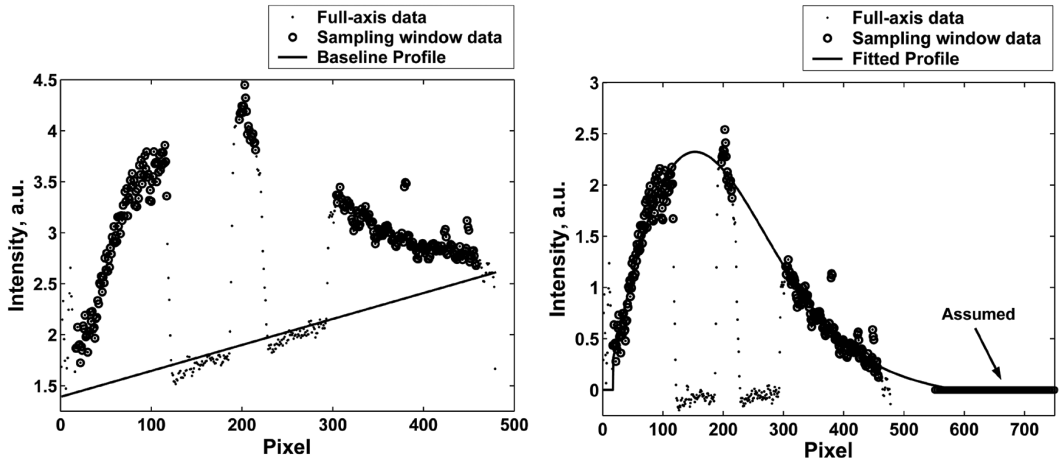

(a) (b)

Figure 68. Example a lower intensity time-averaged profile of the combustion zone after the span-wise average and 3 pixel axial average: (a) before baseline intensity subtraction and (b) after baseline intensity subtraction.

9.2 Expressions for the Analysis of Combustion Zone Fluctuations

In Section 8.2, combustion zone characteristics were defined to quantify the shape and location of the PAC combustion zone. These same combustion zone characteristics were also used to analyze the AF combustion zone. First, the fitted intensity profiles were used to compute the combustion zone characteristics for each camera frame. Denote the fitted intensity profile from frame 'i' as $I(x,t_i)$, where t_i is the time at the beginning of frame 'i' and x is the axial distance from the TS outlet. $I(x,t_i)$ was input into Equations (8.1) to (8.4) to calculate the shape parameters. The computed characteristics adopt the 'i' subscript as well, e.g., $X_{5\%,i}$, STD_i, etc. Next, the distributions of each characteristic over *n* frames were used to quantify the combustion zone fluctuations. The distributions were computed using the following expressions, which are applied to STD_i as an example:

$$\mu_1 = \frac{1}{n}\sum_{i=1}^{n} STD_i \tag{9.1}$$

$$\sigma = \sqrt{\frac{1}{n}\sum_{i=1}^{n}(STD_i - \mu_1)^2} \tag{9.2}$$

where μ_1 and σ are the STD_i distribution mean value and centralized standard deviation, respectively. The μ_1 values indicate the time-averaged changes of the combustion zone. They are analogous to the characteristics values quoted for the PAC experiments. The σ values quantify how much the AF combustion zone fluctuates over the n-frame interval.

9.3 Results and Discussion

The results from three cases will be presented. As in the Chemkin simulations and the PAC experiments, the first case provides baseline measurements of autoignition without a trigger. During this case, ϕ_{vit} was increased in steps to produce corresponding increases in temperature and decreases in $\chi_{O_2,dry}$[8]. The second case demonstrates Jet-A/vitiated-air combustion with the H_2 trigger. The H_2 PR_G was high for this case to emphasize the effects of the trigger. Finally, the third case demonstrates combustion at two relatively lower values of H_2 PR_G. For all cases, Jet-A was injected through port CV1, see Figure 10. The plenum pressure and the thermocouple measurements upstream of the TS were unaffected by Jet-A injection. Thus, no significant heat release occurred

[8] Between temperature and $\chi_{O_2,dry}$, temperature is expected to have the strongest effect on the combustion zone due to the exponential term in Equation (4.26). See Reference [1] for further discussion of the relative effects of temperature and $\chi_{O_2,dry}$.

upstream of the TS. Note that the AF axis used to plot the results in this section is illustrated in Figure 10.

Case 1 Results

Case 1 consists of measurements taken over a data acquisition time of 630 sec to 710 sec. This time interval is divided into four subintervals that correspond to events such as Jet-A injection and ϕ_{vit} changes. Table 15 lists the operating point parameters for each subinterval. Subinterval 1 corresponds to the time before any Jet-A injection. Subinterval 2 corresponds to the onset of Jet-A injection with all other parameters fixed. Subintervals 3 and 4 correspond to step changes in ϕ_{vit}, which produce step changes in T_{tot} of 25 K and 45 K, respectively. The combustion zone intensity was recorded during subintervals 3 and 4 only.

Figure 69 shows the time traces of Plenum pressure, thermocouple temperature, and measured $\chi_{O_2,dry}$ over the entire Case 1 time interval. The circled numbers above the plot indicate the approximate midpoints of each subinterval. Predicted profiles are shown for $\chi_{O_2,dry}$ after vitiator (methane/air) combustion and $\chi_{O_2,dry}$ after complete Jet-A/vitiated-air combustion. These were calculated using the measured air, methane and Jet-A flow rates. Several of the profiles in Figure 69 are shown after some post-processing. A 5-point moving average was applied to the PL1 thermocouple data to

Table 15. Case 1 subinterval operating parameters

Event #: (Time Interval)	$P_{PL}, psia$	T_{tot}, K	$\Delta T_{TS}, K$	$\dot{m}_{air}\ {}^{kg}/_{s}$	ϕ_{vit}	$\dot{m}_{Jet\,A}\ {}^{g}/_{s}$	$SMD, \mu m$	ϕ_{aft}
1: (631-636)	30	1260	110	0.215	0.408	x	x	x
2: (655-660)	30	1260	110	0.215	0.408	0.816	30	0.096
3: (685-690)	30.5	1285	110	0.215	0.418	0.816	30	0.098
4: (694-698)	31	1330	110	0.215	0.454	0.816	30	0.104

reduce noise. Also, offsets were added to the D3 and D5 thermocouple data so that they match the other thermocouples during subinterval 1, when there was no afterburner combustion. Note that this thermocouple offset procedure was also performed in the prime stage investigation, see Section 5.1. Finally, the O_2 sensor data was translated in time to compensate for the gas sample travel time from the plenum to the sensor housing. The data was translated such that abrupt changes in the measured $\chi_{O_2,dry}$ matched the corresponding abrupt changes in fuel and air flow rates. In Case 1, Jet-A was injected into the AF at 641 sec. At this time, the measured temperature downstream of the TS increased due to Jet-A autoignition. After about 5-10 sec, the thermocouples reached steady-state temperatures that were higher with each successive downstream thermocouple, as was observed in the prime stage investigation (see Section 5.1). ϕ_{vit} was increased at approximately 669 sec, which caused an increase in the thermocouple temperatures and a decrease in the measured and predicted $\chi_{O_2,dry}$. At first, the building methane control system overshot the target methane flow rate. Thus, the initial ϕ_{vit} increase at 669 sec was followed by a steady decline to the target ϕ_{vit} value from 670 sec to 690 sec, as reflected by the temperature and $\chi_{O_2,dry}$ profiles. The same overshoot and decay occurred with the next ϕ_{vit} step change at 691 sec.

Figure 69 shows that the measured $\chi_{O_2,dry}$ profile closely matches the predicted $\chi_{O_2,dry}$ profile during the entire Case 1 time interval. During subinterval 1, the measured $\chi_{O_2,dry}$ profile (solid line) coincides with the predicted vitiated-air $\chi_{O_2,dry}$ profile (long-dashed line). When Jet-A was injected at 641sec, the measured $\chi_{O_2,dry}$ profile decreased

for about 3 sec to reach the profile of predicted $\chi_{O_2,dry}$ for Jet-A/vitiated-air combustion (short-dashed line). The 3 sec gradual decrease of the measured $\chi_{O_2,dry}$ profile was caused by the filling of the O_2 sensor housing with fresh sampled gas. At 669 sec, and then again at 691 sec, the measured and predicted $\chi_{O_2,dry}$ decreased due to the increase in ϕ_{vit}. The Jet-A valve was shut at about 698 sec, which caused the measured $\chi_{O_2,dry}$ to increase back toward the predicted $\chi_{O_2,dry}$ profile for primary combustion only. The agreement between measured and predicted $\chi_{O_2,dry}$ provides a strong, yet incomplete, indication that $\eta_c \approx 1$ during Case 1. It is an incomplete indication because the results from the PAC

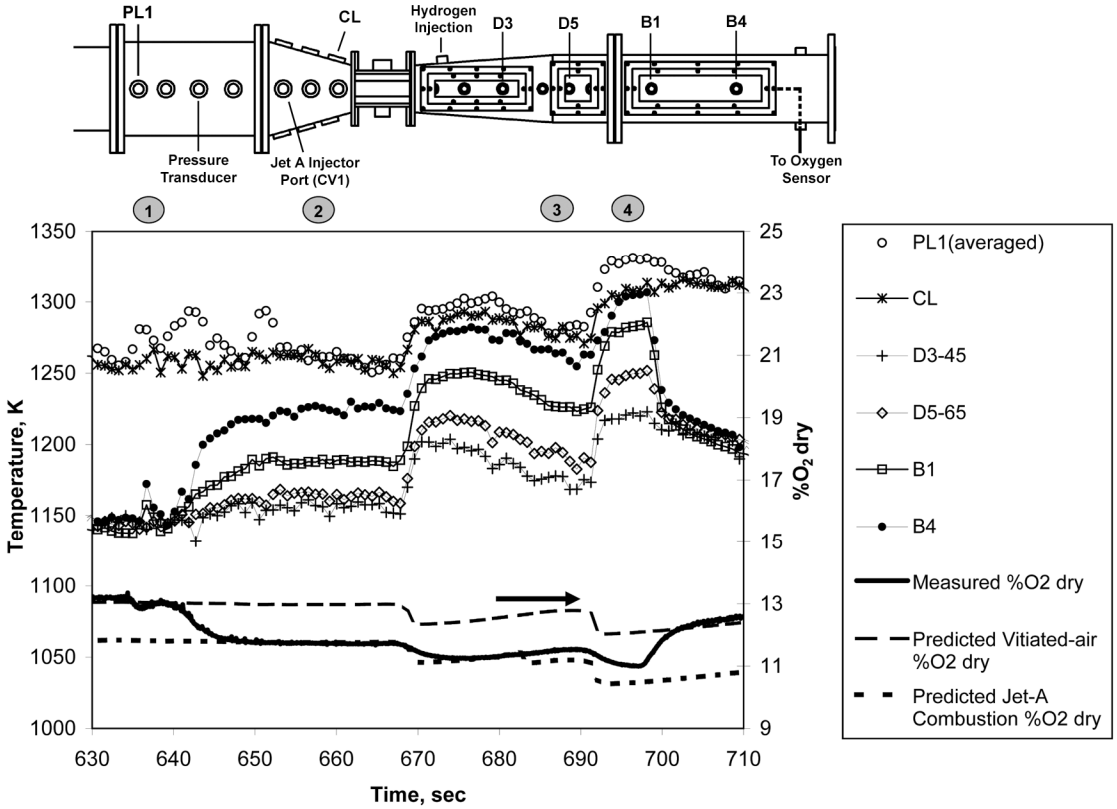

Figure 69. Case 1 thermocouple measurements and dry oxygen content measurements and predictions. Numbers listed above the plot are approximately centered over the corresponding subintervals.

experiments showed that $\chi_{O_2,dry}$ often reached nearly equilibrium values well before $\chi_{CO_2,dry}$, see Section 8.6. Thus, it is possible that $\eta_c < 1$ for Case 1 despite the agreement between the measured and predicted $\chi_{O_2,dry}$.

Figure 70 shows the temperature increase measured by each thermocouple scaled by the predicted temperature increase from complete Jet-A/vitiated-air combustion with no dissociation. Note that this scaled temperature increase, termed $\Delta T / \Delta T_{\text{expected}}$, is the time-averaged value over the corresponding subinterval. The profiles for subintervals 2, 3 and 4 show the axial increase in temperature due to Jet-A autoignition (a trend first shown in Figure 24). These profiles indicate the progress of the Jet-A/vitiated-air autoignition process: an inflection point in the profile (positive to negative second derivative, such as at the B1 thermocouple in the subinterval 4 profile) indicates that the autoignition process is nearing completion, and a zero slope at the end of the profile suggests complete combustion. The subinterval 2 and 3 profiles do not have inflection points and are well below a scaled temperature of one, which indicates that the autoignition process was far from complete by the B4 thermocouple. This is inconsistent

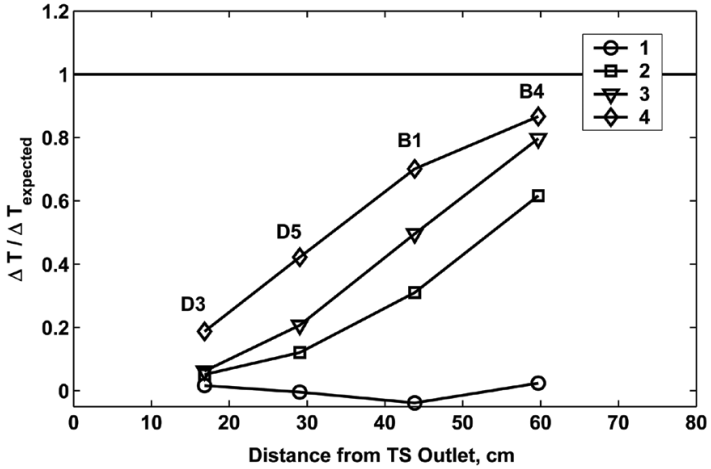

Figure 70. Scaled temperature increase for the Case 1 subintervals.

with the $\chi_{O_2,dry}$ measurements, which suggested nearly complete combustion. The subinterval 4 profile does not suggest complete combustion either. It has an inflection point at the B1 thermocouple, but the slope is still far from zero at the B4 thermocouple and the maximum scaled temperature is only about 0.87. However, it should be noted that more thermocouples (higher spatial resolution) could have revealed an inflection point and a more significant decrease in slope, especially for subintervals 3 and 4.

Figure 71 shows the time-averaged intensity measurements and the fitted profiles for subintervals 3 and 4. The data are shown after subtraction of the baseline intensity. The data and fitted profiles clearly indicate that the combustion zone shifted upstream with the ϕ_{vit} increase. This upstream shift was accompanied by an increase in intensity and a shorter combustion zone, as quantified shortly. These intensity profiles can be used to double-check the $\chi_{O_2,dry}$ measurements. In the PAC experiments, $\eta_c = 1$ only if the intensity dropped completely to zero by the sampling tube inlet, see Section 8.6. In Figure 71, the fitted profiles for both subintervals fall to zero intensity 5-10 cm

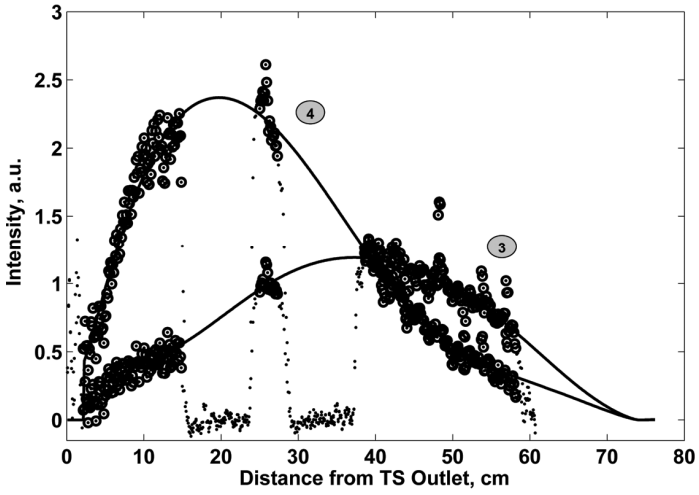

Figure 71. Time-averaged intensity profiles over subintervals 3 and 4 with fitted profiles. The points correspond to the full-axis data, the open circles correspond to the sampling window data and the line is the profile fit.

downstream of the sampling tube inlet, which is located at 66 cm. Thus, η_c was likely less than unity. Since the measured $\chi_{O_2,dry}$ data indicates nearly complete O_2 consumption, the intensity measurements suggest that there was still significant CO at the AF outlet for Case 1.

Figure 72(a) and (b) show the fitted intensity profiles for five sequential frames within subintervals 3 and 4, respectively. The profile sequences illustrate how the combustion zone location and shape change from frame to frame. Arrows guide through the frame sequence starting from the profile labeled 'A'. The profiles in each new frame clearly have different values of $X_{5\%,i}$, $X_{95\%,i}$, $L_{comb,i}$, STD_i, etc. This variation is depicted in Figure 73, which shows the $X_{5\%,i}$ and STD_i values over the Case 1 time range. The data after 698 sec should be neglected since there was no longer any Jet-A injection. Figure 73(a) depicts the strong effect of the ϕ_{vit} changes on $X_{5\%,i}$. Initially, the value of $X_{5\%,i}$ varied widely over the first half of the diverging section. The step increase in ϕ_{vit} at 691 sec greatly reduced the $X_{5\%,i}$ mean value and variation, as quantified shortly. In

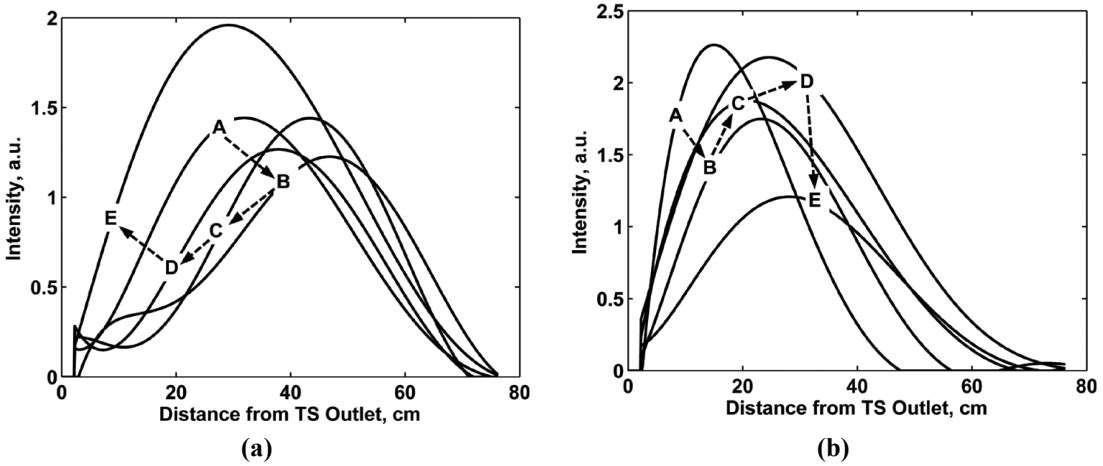

Figure 72. Sample 5 frame sequences of the profile fits starting from a random frame within (a) subinterval 3 and (b) subinterval 4. The sequences begin with curve A and proceed in alphabetical order.

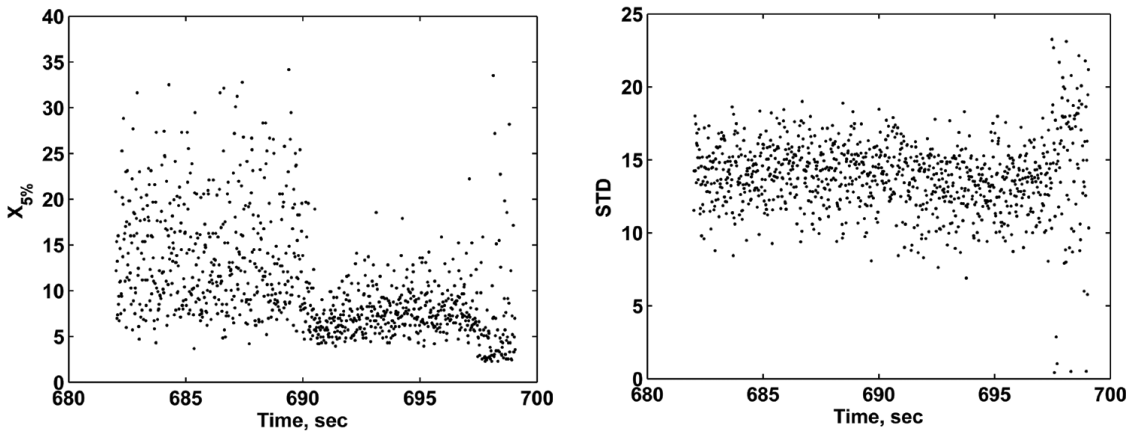

Figure 73. Values of (a) $X_{5\%,i}$ [cm] and (b) $STD_{,i}$ [cm] for all Case 1 frames (includes subintervals 3 and 4).

contrast, Figure 73(b) shows that STD_i was not as significantly affected by the ϕ_{vit} change. In other words, the results suggest that ϕ_{vit} had a stronger effect on the position of the autoignition combustion zone than on its length.

Figure 74 and Figure 75 show histograms of the combustion zone characteristics for Case 1 subintervals 3 and 4. The corresponding values of μ_1 and σ are listed on each plot. The μ_1 values for each characteristic quantify the observed upstream shift and decrease in length of the combustion zone from subinterval 3 to 4. For example, μ_1 for $X_{5\%}$ decreased from 14.02 cm to 8.14 cm, and L_{comb} decreased from 46.44cm to 43.60 cm. The σ values quantify the effect of ϕ_{vit} on the frame-by-frame combustion zone fluctuations. The ϕ_{vit} increase from subinterval 3 to 4 decreased σ for $X_{5\%}$, X_{MAX} and X_M. For example, σ for X_{MAX} decreased from 9.29 cm to 6.72 cm. However, σ of $X_{95\%}$ increased, which caused σ of L_{comb} to increase. σ of *STD* and *SK* remained about the same. Thus, the ϕ_{vit} increase helped stabilize the onset of the combustion process but did not reduce the variation in length or shape.

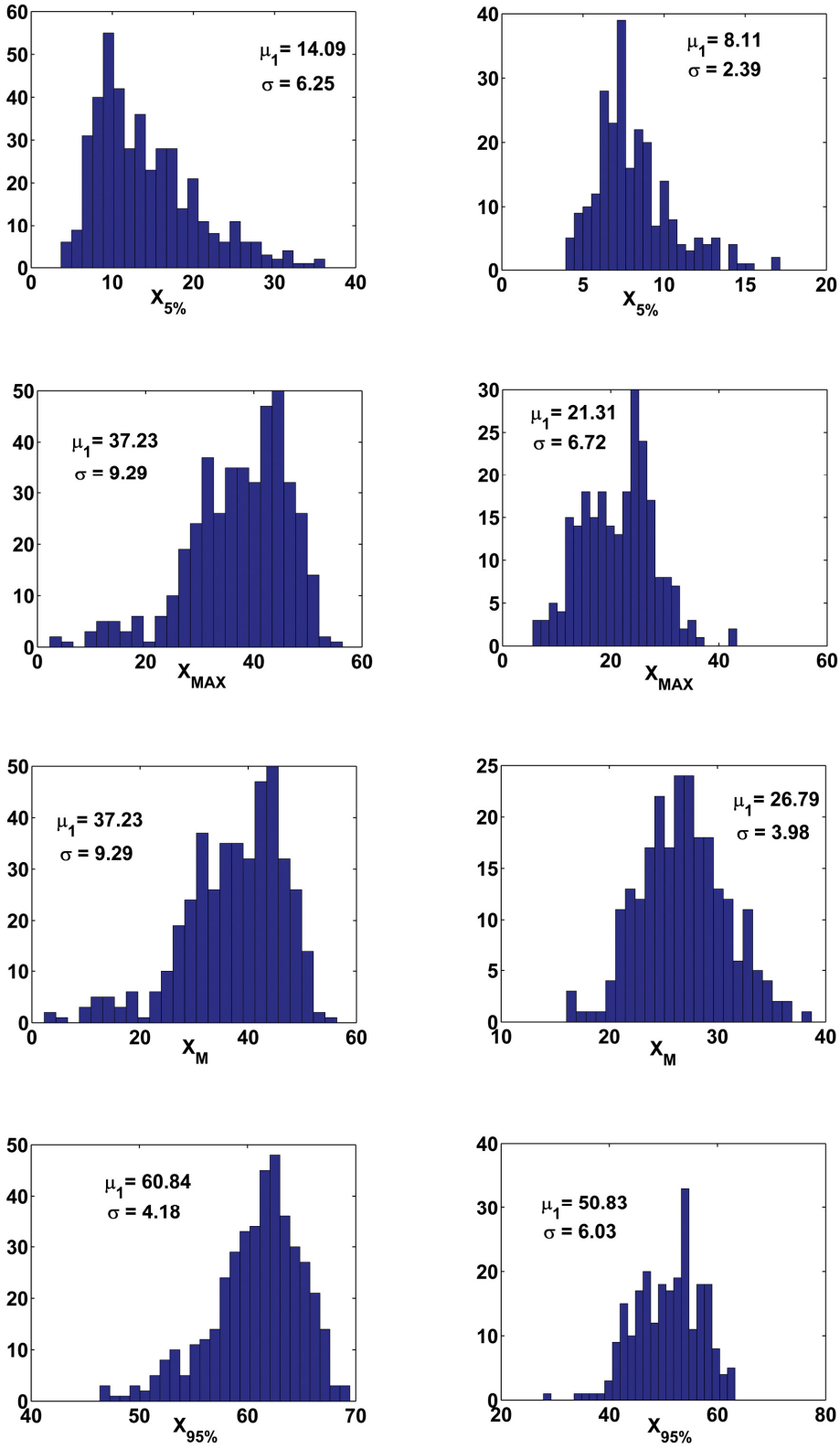

Figure 74. Case 1 histograms of $X_{5\%,i}$, $X_{MAX,i}$, $X_{M,i}$, and $X_{95\%,i}$. Left column is subinterval 3 and right column is subinterval 4. Units are in cm.

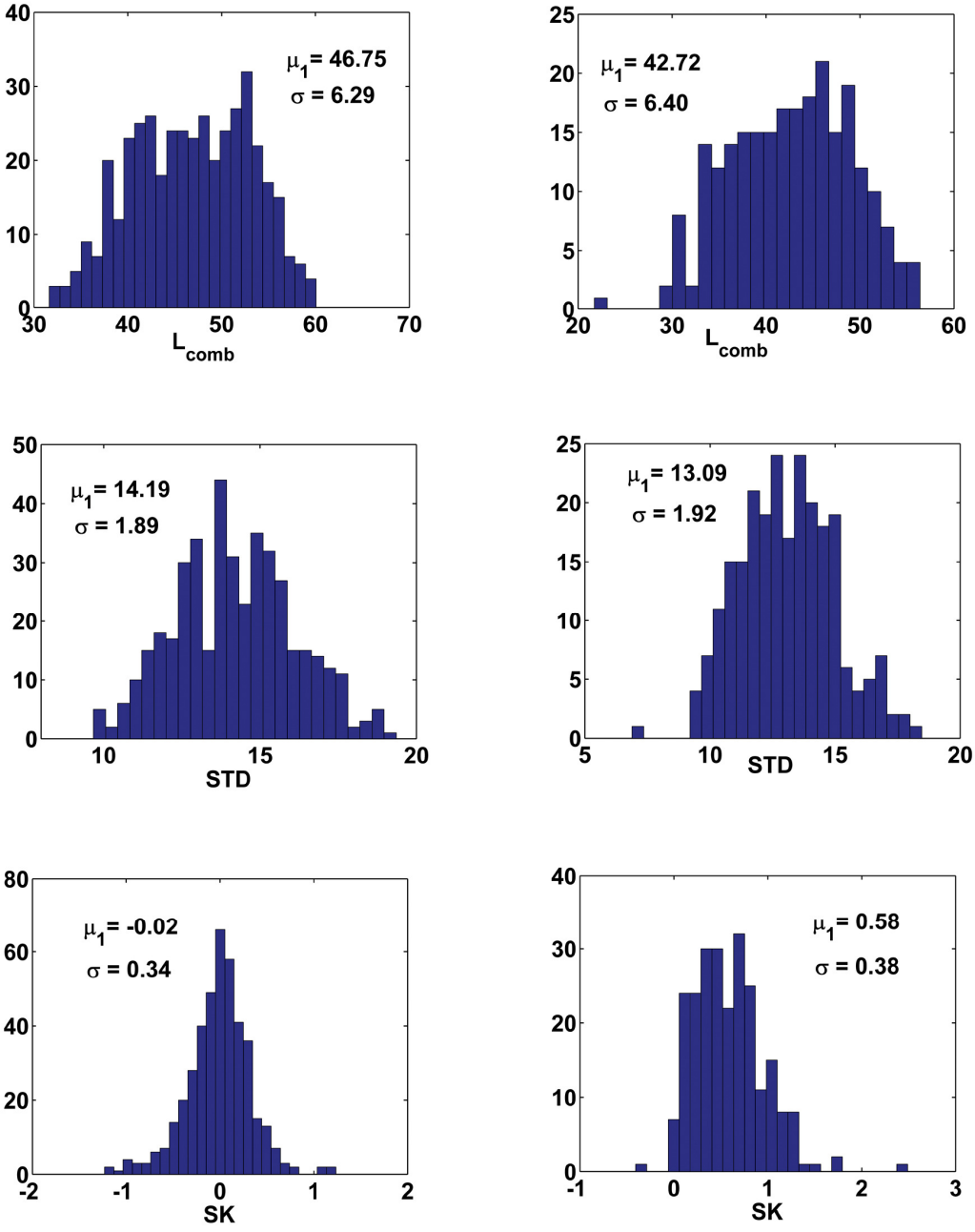

Figure 75 Case 1 histograms of $L_{comb,i}$ [cm], STD_i [cm], and SK_i [nondimensional]. Left column is subinterval 3 and right column in subinterval 4.

Case 2 Results

Table 16 shows the operating parameters for the Case 2 subintervals. All the subintervals had either Jet-A combustion or Jet-A combustion with H_2 at a PR_G of 55%; There are no subintervals shown without Jet-A combustion such as in Case 1. Chemiluminescence intensity was recorded between 1030-1047sec, which includes subintervals 5 and 6 only. Note that a 55% PR_G is extremely high for practical application in an engine. However, a 55% PR_L is likely to occur in the vicinity of the trigger gas jet (see Figure 45(b) and accompanying discussion). Thus, the Case 2 results could be interpreted as expected effects in the near-field of the PAT afterburner trigger.

Figure 76 shows the time traces of the Plenum pressure, thermocouple temperature, and measured $\chi_{O_2,dry}$. Predicted $\chi_{O_2,dry}$ profiles are shown for primary combustion only, for Jet-A injection, and for Jet-A/H_2 injection. The numbered circles above the plot are approximately centered at each subinterval. For this case, there were oscillations in the building methane flow rate controller with a period of about 40 sec, as indicated by the predicted primary combustion $\chi_{O_2,dry}$ profile. Subintervals 1, 4 and 5 have no H_2 injection. The temperature profiles in these subintervals depict the typical AF Jet-A autoignition process; i.e., the temperature increase measured by each successive

Table 16. Case 2 subinterval operating parameters

Event #: (Time Interval)	$P_{PL}, psia$	T_{tot}, K	$\Delta T_{TS}, K$	$\dot{m}_{air}\ ^{kg}/_{s}$	ϕ_{vit}	$\dot{m}_{Jet\,A}\ ^{g}/_{s}$	$SMD, \mu m$	ϕ_{aft}	$PR_{G,H2}, \%$
1: (1000-1003)	31	1300	110	0.22	0.418	1.06	31	0.096	x
2: (1007-1009)	31	1300	110	0.22	0.418	1.06	31	0.096	55
3: (1015-1017)	31.5	1320	110	0.22	0.443	1.06	31	0.1	55
4: (1021-1025)	31.5	1310	110	0.22	0.44	1.06	31	0.1	x
5: (1031-1034)	31	1290	110	0.22	0.42	1.06	31	0.096	x
6: (1040-1043)	31	1300	110	0.22	0.42	1.06	31	0.096	55

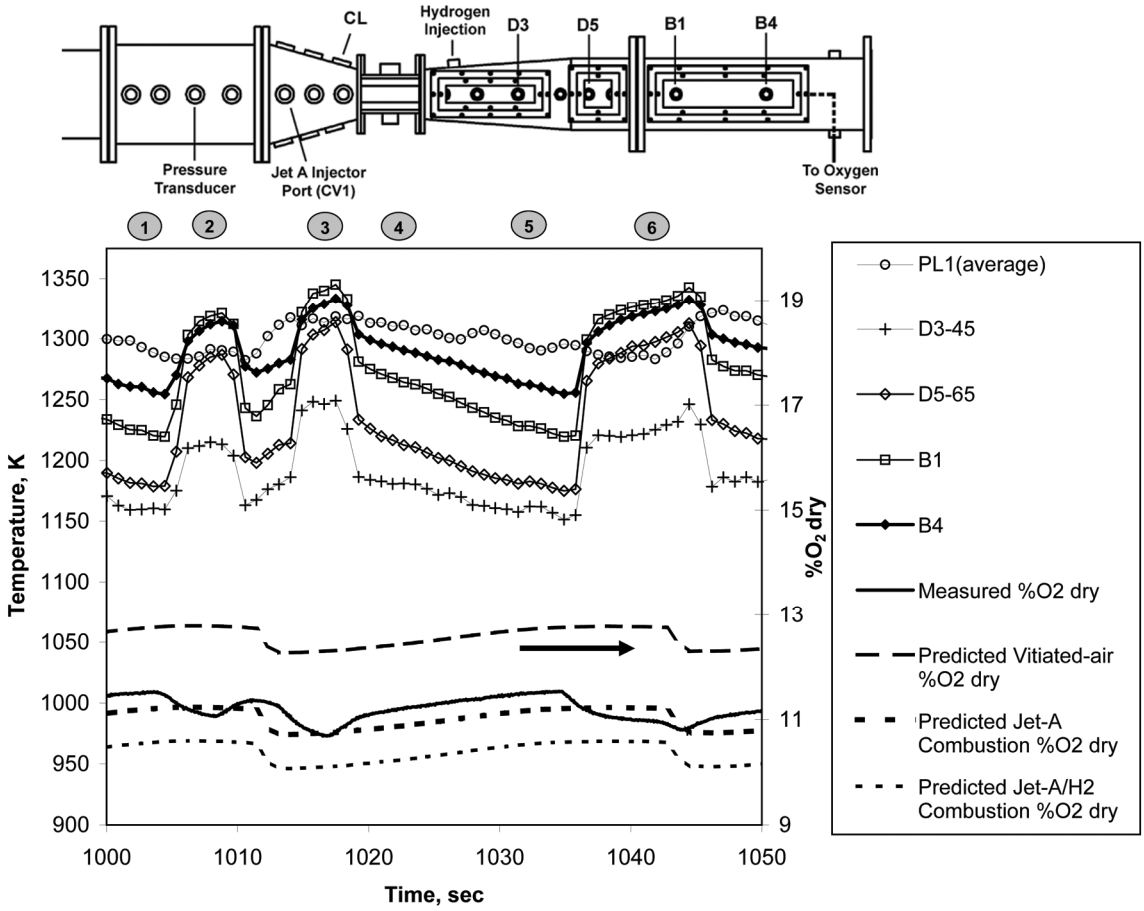

Figure 76. Case 2 thermocouple measurements and dry oxygen content measurements and predictions. Numbers listed above the plot are approximately centered over the corresponding subintervals.

downstream thermocouple. The H_2 trigger was utilized within subintervals 2, 3 and 6. During these subintervals, the temperature profiles clearly show a sharp increase due to the H_2 combustion process. Like Case 1, the measured $\chi_{O_2,dry}$ profile closely matches the predicted $\chi_{O_2,dry}$ profiles with and without H_2 injection.

Figure 77 shows the scaled temperature profiles for Case 2. Note that the denominator of the scaled temperature increase, $\Delta T_{\text{expected}}$, is computed without H_2 injection (only Jet-A), so the subinterval profiles with H_2 injection reach values greater than unity. The horizontal lines indicate the expected values with and without H_2

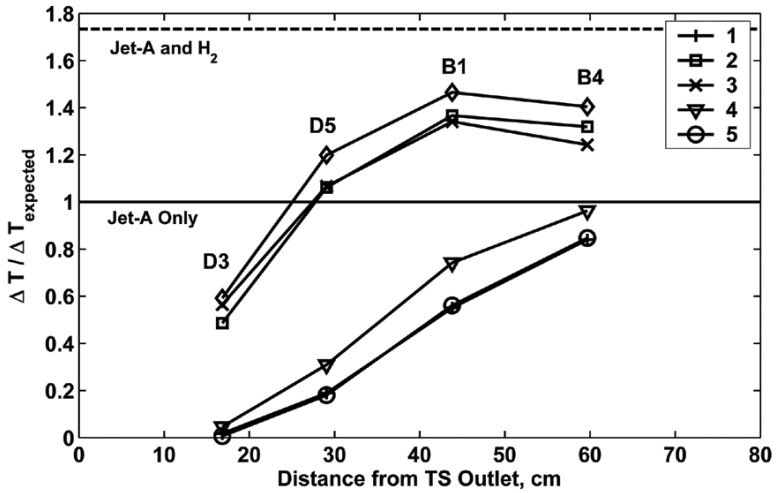

Figure 77. Scaled temperature increase for the Case 2 subintervals. The horizontal lines denote the expected values with Jet-A combustion only (1 by definition) and with Jet-A/H_2 combustion.

injection. The profiles for subintervals 1 and 5 nearly overlap, which demonstrates the repeatability of the autoignition combustion process. The profile for subinterval 4 is slightly higher than 1 and 5 because of the momentarily higher methane flow rate. The subinterval 1, 4 and 5 profiles all have an inflection point at the B1 thermocouple, but their slopes are still well above zero at the B4 thermocouple. However, the Subinterval 4 profile reaches a scaled temperature of nearly one, which does suggest complete combustion. The profiles for subintervals 2, 3 and 6 show that H_2 injection significantly increased the measured temperature. Although the maximum scaled temperatures reach only about 80% of the predicted value for complete Jet-A/H_2/vitiated-air combustion, the inflection points and nearly zero slope at the B4 thermocouple location suggest complete combustion.

Figure 78 shows the time-averaged intensity profiles of the combustion zone for subintervals 5 and 6. The profile for subinterval 5 was multiplied by 2 so that it could be compared with the much higher intensity subinterval 6 profile. The large amount of H_2 injection significantly increased the maximum intensity and clearly shifted the

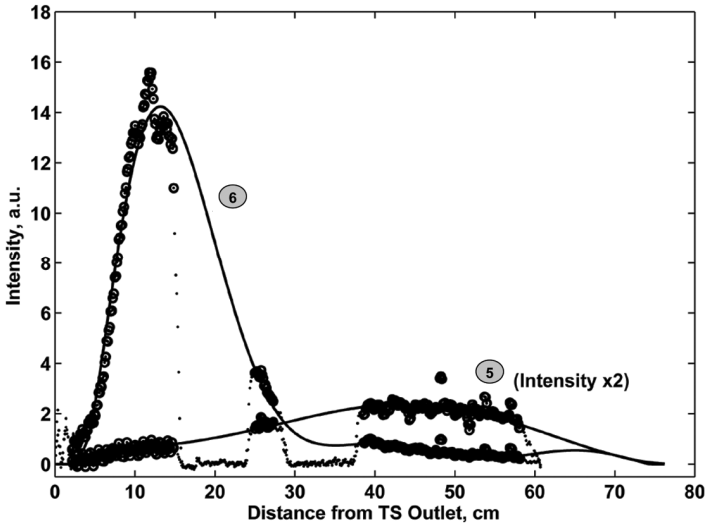

Figure 78. Time-averaged intensity profiles over Case 2 subintervals 5 and 6 with fitted profiles. The points correspond to the intensity profile along the full length of the facility, the open circles correspond to the data within the sampling window and the line is the profile fit.

combustion zone far upstream, as was observed by the thermocouple measurements. Note that the changes in the intensity profile with H_2 addition are similar to those observed in the PAC experiments, e.g., see Figure 61. The subinterval 5 fitted profile does not reach zero until about 10-15 cm downstream of the sampling tube inlet. This suggests incomplete combustion and contradicts the suggested $\eta_c \approx 1$ from the O_2 sensor measurements. The subinterval 6 profile drops to zero well before the sampling tube inlet, which does suggest complete combustion.

Figure 79(a) and (b) demonstrate the effect of the H_2 trigger on $X_{5\%,i}$ and STD_i, respectively. H_2 was injected at about 1036 sec. At this time, the $X_{5\%,i}$ mean value and variation drops dramatically. Thus, the H_2 trigger anchored the combustion zone near the trigger injection location. The trigger had a weaker effect on STD_i. Although the mean STD_i decreased, the variation about the mean was only slightly smaller, as quantified

shortly. The H_2 trigger was turned off at 1045 sec, and the mean value and scatter in $X_{5\%,i}$ and STD_i increased immediately thereafter.

Figure 80 and Figure 81 show histograms of the combustion zone characteristics for Case 2 subintervals 5 and 6. The values of μ_1 for each characteristic quantify the combustion zone upstream shift and reduction in length. For example, μ_1 for $X_{5\%,i}$ decreases from 16.54 cm to 3.07 cm, and μ_1 for STD_i decrease from 14.19 cm to 11.58 cm. SK increases significantly above zero with H_2 injection, indicating that the combustion process is concentrated nearer to the H_2 injection location. The trigger reduces σ of $X_{5\%,i}$, X_{MAX}, and STD_i. For example, σ of $X_{5\%,i}$ decreases from 7.69 cm to 0.58 cm. This trend is opposed to the trend observed in Case 1, where the increase in ϕ_{vit} decreased σ for only $X_{5\%,i}$ and X_{MAX} and did so by a lesser amount. On the other hand, σ increases for $X_{95\%,i}$, which caused σ to increase for $L_{comb,i}$ and SK_i. The higher σ for $X_{95\%,i}$ in subinterval 6 was caused by actual intensity variations and also polynomial curve fit inaccuracies. Since STD_i is calculated using the entire profile, the

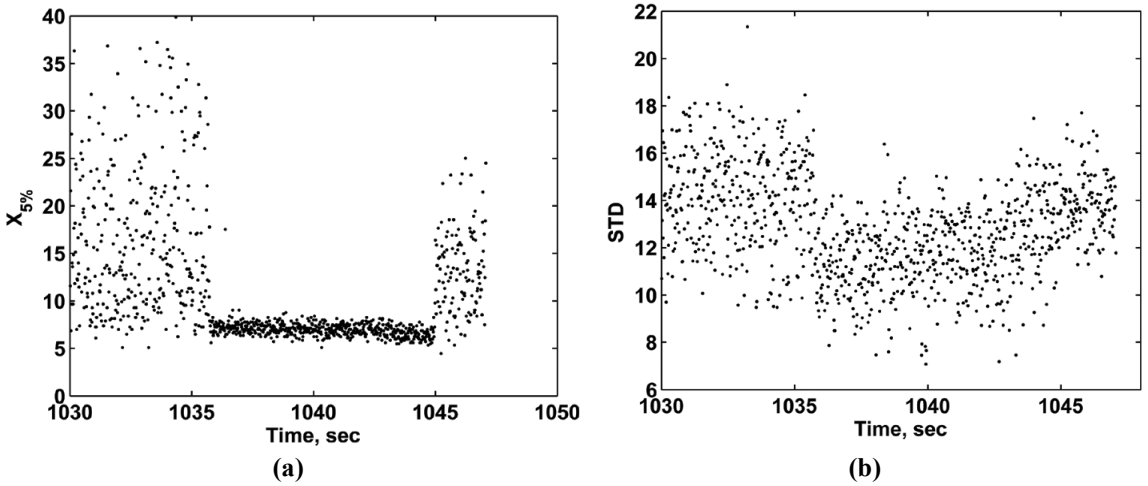

Figure 79. Values of (a) $X_{5\%,i}$ [cm] and (b) STD_i [cm] for the Case 2 frames (includes subintervals 5 and 6).

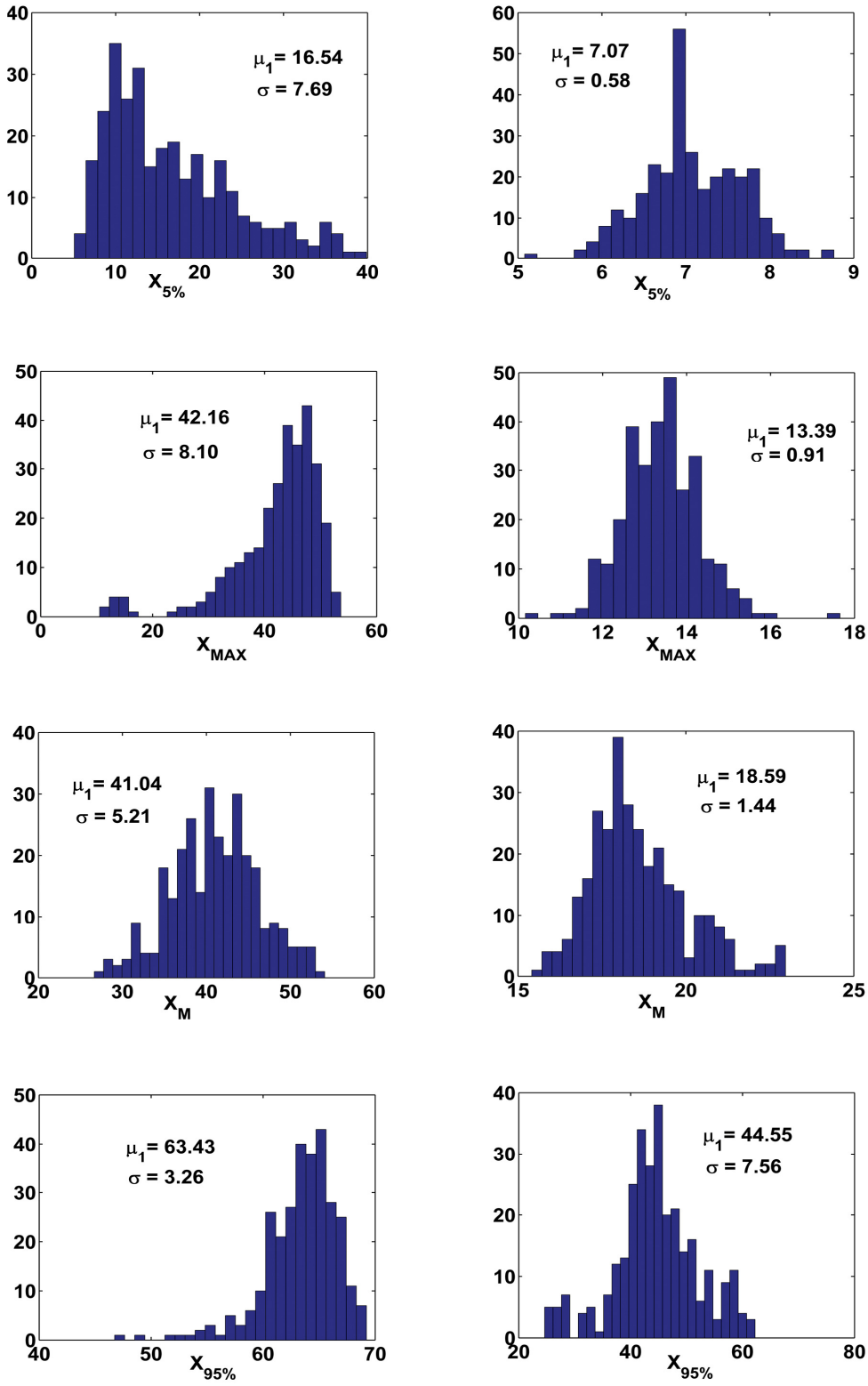

Figure 80 Case 2 histograms of $X_{5\%,i}$, $X_{MAX,i}$, $X_{M,i}$, and $X_{95\%,i}$. Left column is subinterval 5 and right column is subinterval 6. Units are in cm.

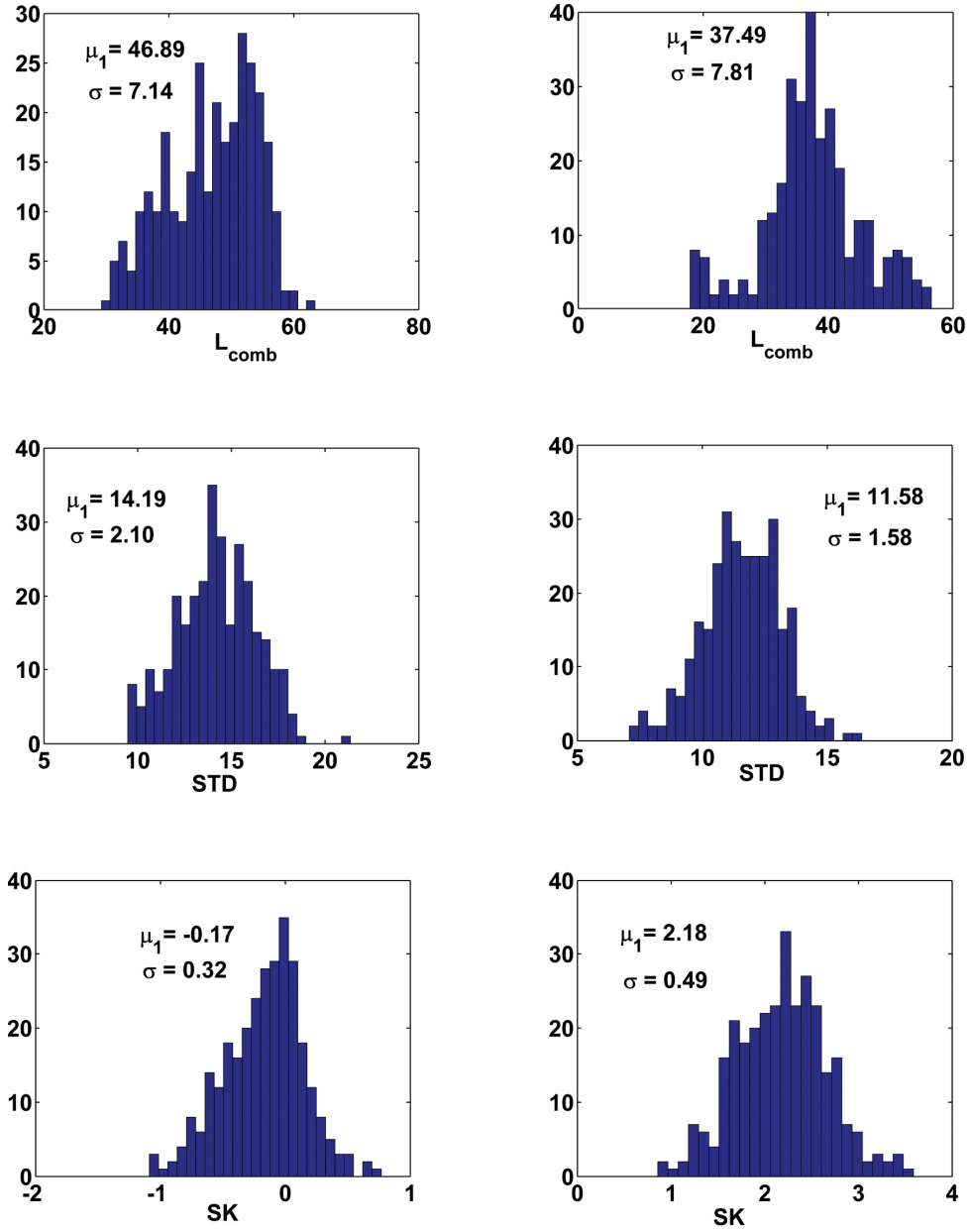

Figure 81. Case 2 histograms of $L_{comb,i}$ [cm], STD_i [cm], and SK_i [nondimensional]. Left column is subinterval 5 and right column in subinterval 6.

influence of tail end fluctuations is reduced. Thus, the reduction in μ_1 and σ for STD_i best represents the effect of the H_2 trigger on the combustion zone width.

Case 3 Results

Table 17 lists the Case 3 subinterval operating parameters. For all subintervals, the value of ϕ_{aft} was nearly twice as high as in Cases 1 and 2. Two values of H_2 PR_G were tested, and they were both much lower than the H_2 PR_G in Case 2. The chemiluminescence intensity was measured during subintervals 2 and 3 only.

Figure 82 shows the time traces of the plenum pressure, thermocouple temperatures, and measured and predicted $\chi_{O_2,dry}$. The B4 thermocouple is not shown, because it was damaged during the test. Jet-A was injected throughout the entire case, and H_2 was injected at approximately 810 sec. The H_2 flow rate initially overshot its target value, resulting in a momentary spike in temperature, and subsequently relaxed to the target value by approximately 812 sec. The H_2 flow rate (and PR_G) was increased at 822 sec. The H_2 injection and flow rate increase produced rapid increases in the measured temperature and decreases in the measured $\chi_{O_2,dry}$, as expected. As in Cases 1 and 2, the measured $\chi_{O_2,dry}$ nearly matched the predicted $\chi_{O_2,dry}$ for combustion with and without H_2.

Table 17. Case 3 subinterval operating points

Event #: (Time Interval)	$P_{PL}, psia$	T_{tot}, K	$\Delta T_{TS}, K$	$\dot{m}_{air}$ $^{kg}/_{s}$	ϕ_{vit}	$\dot{m}_{Jet\,A}$ $^{g}/_{s}$	$SMD, \mu m$	ϕ_{aft}	$PR_{G,H2}$,%
1: (802-807)	28.6	1240	90	0.211	0.39	3.03	38	0.346	x
2: (819-821)	28.6	1237	90	0.211	0.39	3.03	38	0.346	8
3: (822-824)	28.6	1247	90	0.211	0.39	3.03	38	0.346	14.6

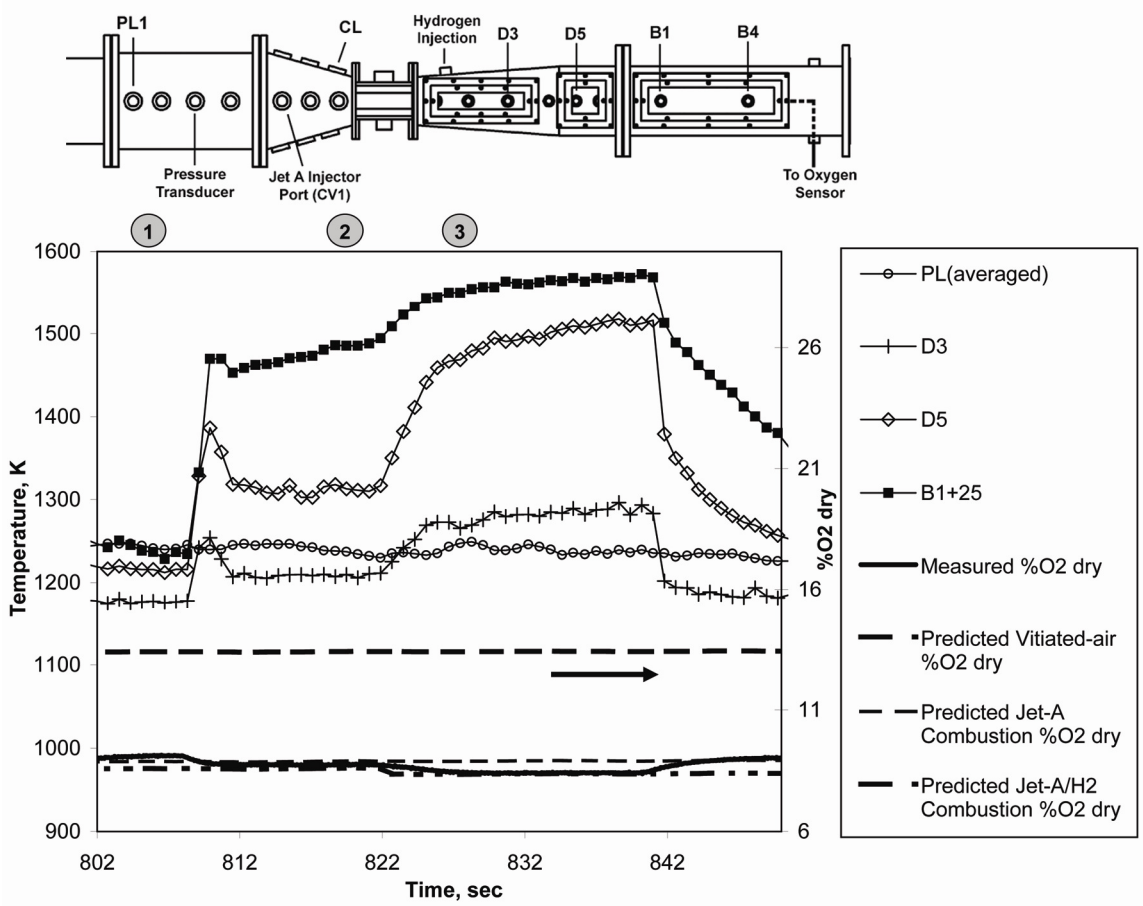

Figure 82. Case 3 thermocouple measurements and dry oxygen content measurements and predictions. Numbers listed above the plot are approximately centered over the corresponding subintervals.

Figure 83 shows the scaled temperature profiles for the Case 3 subintervals. The profiles suggest a significant upstream shift of the combustion zone from subinterval 1 to subinterval 3. For subinterval 3, the combustion zone shifted far enough upstream so that the inflection point appeared at the B1 thermocouple, far upstream of the damaged B4 thermocouple and the AF exhaust. The maximum scaled temperature is far below unity for subinterval 1, but the H_2 trigger brings the profiles much closer to their corresponding values for complete combustion. The low value of the subinterval 1 scaled temperature profile contradicts the $\chi_{O_2,dry}$ measurements, which suggest $\eta_c \approx 1$. It is speculated, however, that additional downstream thermocouples would have revealed a more

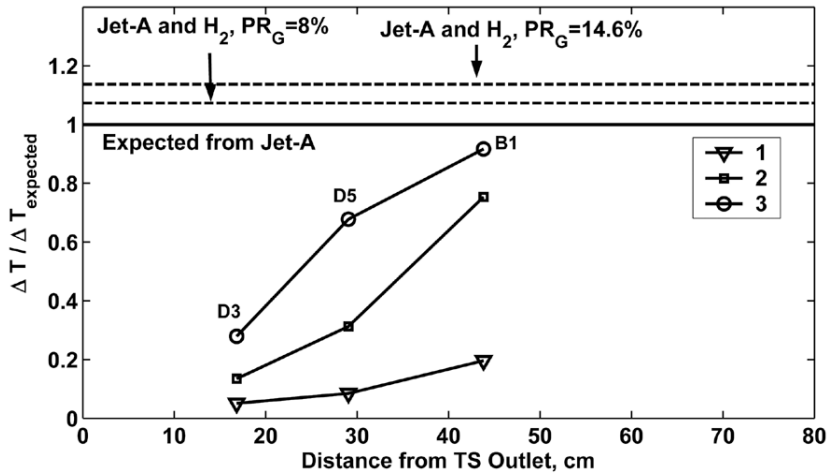

Figure 83. Scaled temperature increase for the Case 3 subintervals. Horizontal lines denote the expected values with Jet-A combustion only (1 by definition) and with Jet-A/H_2 combustion.

significant temperature increase before the sampling tube inlet. The subinterval 2 and 3 profiles attain maximum values close to prediction and, thus, do suggest that $\eta_c \approx 1$ was possible by the sampling tube inlet.

Figure 84 shows the time-averaged intensity measurements for Case 3 subintervals 2 and 3. The profiles clearly show that the H_2 PR_G increase shifted the combustion zone upstream and increased the chemiluminescence intensity. Note that these profiles closely resemble the PAC intensity profiles for cases with increasing H_2 PR_G, see Figure 61. The subinterval 2 intensity profile was still slightly above zero intensity at the sampling tube inlet, which suggests a significant amount of CO in the sampled gas. The subinterval 3 fitted profile was also above zero at the sampling tube outlet. It seems, however, that the polynomial fit did not capture the correct behavior of the intensity profile downstream of 60 cm, because the sampling window data suggests that intensity drops to zero by about 62 cm.

Finally, Figure 85 and Figure 86 show the histograms for the subinterval 2 and 3 combustion zone characteristics. The values of μ_1 and σ quantify the upstream shift and

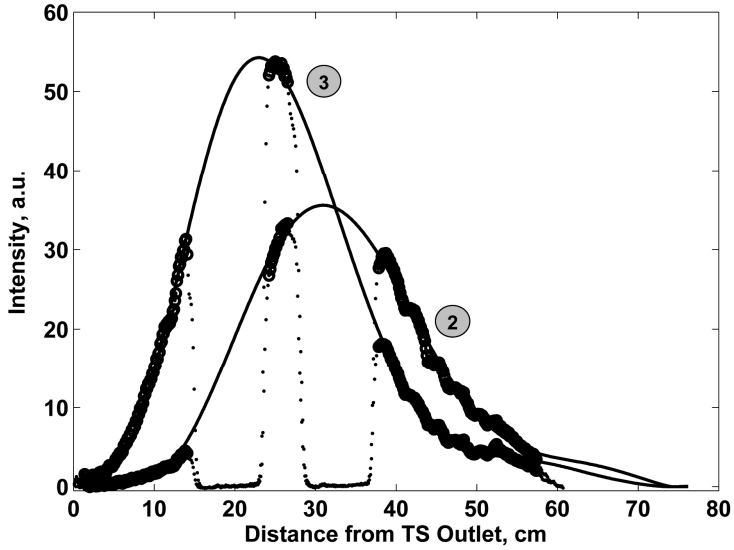

Figure 84. Time-averaged intensity profiles over Case 3 subintervals 2 and 3 and fitted profiles. The points correspond to the intensity profile along the full length of the facility, the open circles correspond to the data within the sampling window and the line is the profile fit.

reduction in fluctuations from subintervals 2 to 3. For example, μ_1 for $X_{5\%,i}$ decreases from 18.39 cm to 12.00 cm and σ for $X_{5\%,i}$ decreases from 3.02 cm to 2.42 cm. The μ_1 values for STD_i and $L_{comb,i}$ decrease to a lesser extent than $X_{5\%,i}$. Thus, H_2 injection had a stronger effect on combustion zone location than length, as was also observed in Case 2 and in the PAC experiments. Note that σ for $X_{95\%,i}$ was less than in Case 2 subinterval 6 (H_2 injection). Consequently, σ for STD_i, $L_{comb,i}$ and SK_i actually decreased with the addition of more H_2 trigger gas. In summary, the increase in H_2 trigger gas from subinterval 2 to 3 reduced the mean value and variation of all combustion zone characteristics except σ for $X_{95\%,i}$.

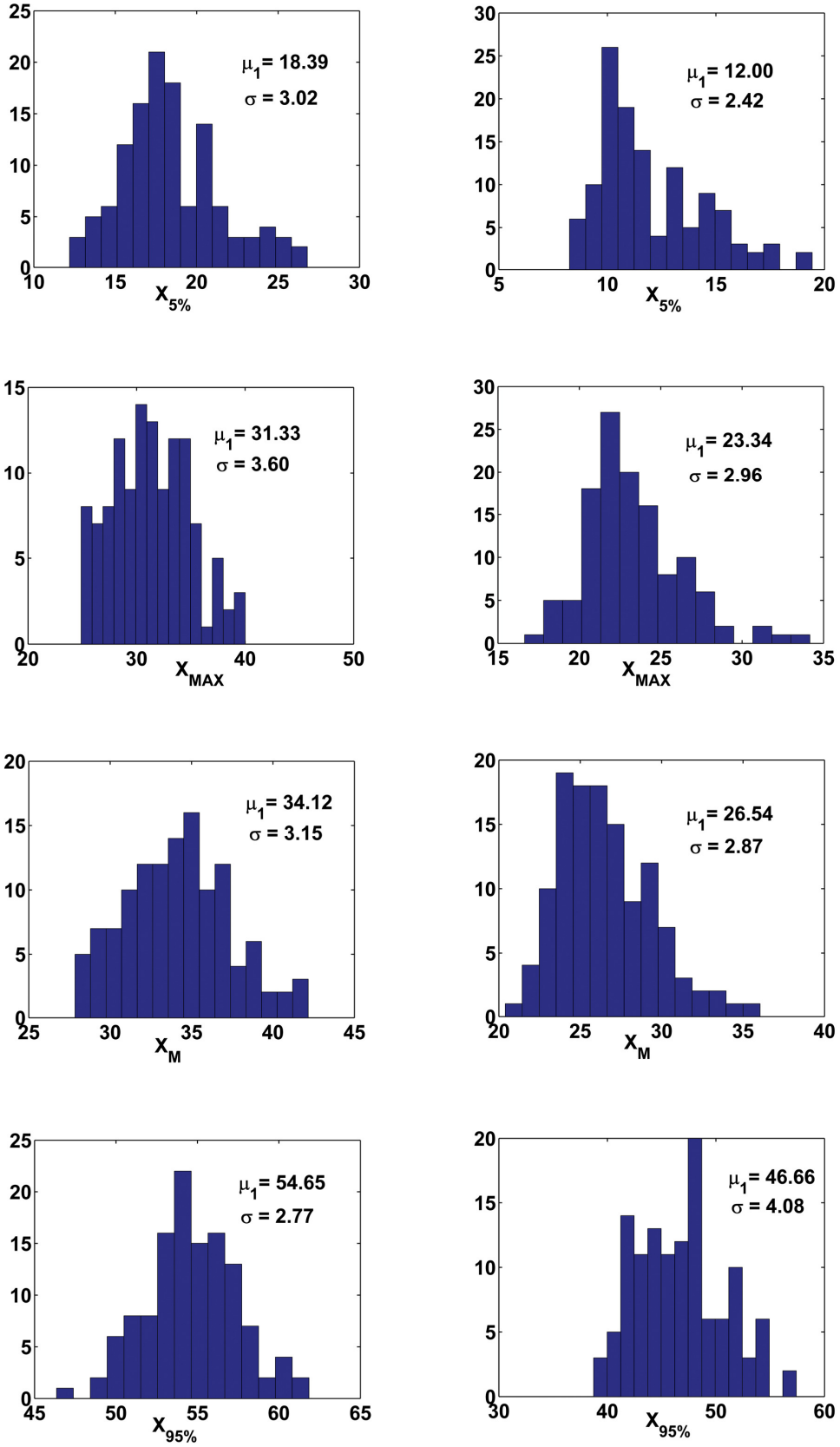

Figure 85 Case 3 histograms of $X_{5\%,i}$, $X_{MAX,i}$, $X_{M,i}$, and $X_{95\%,i}$. Left column is subinterval 2 and right column is subinterval 3. Units are in cm.

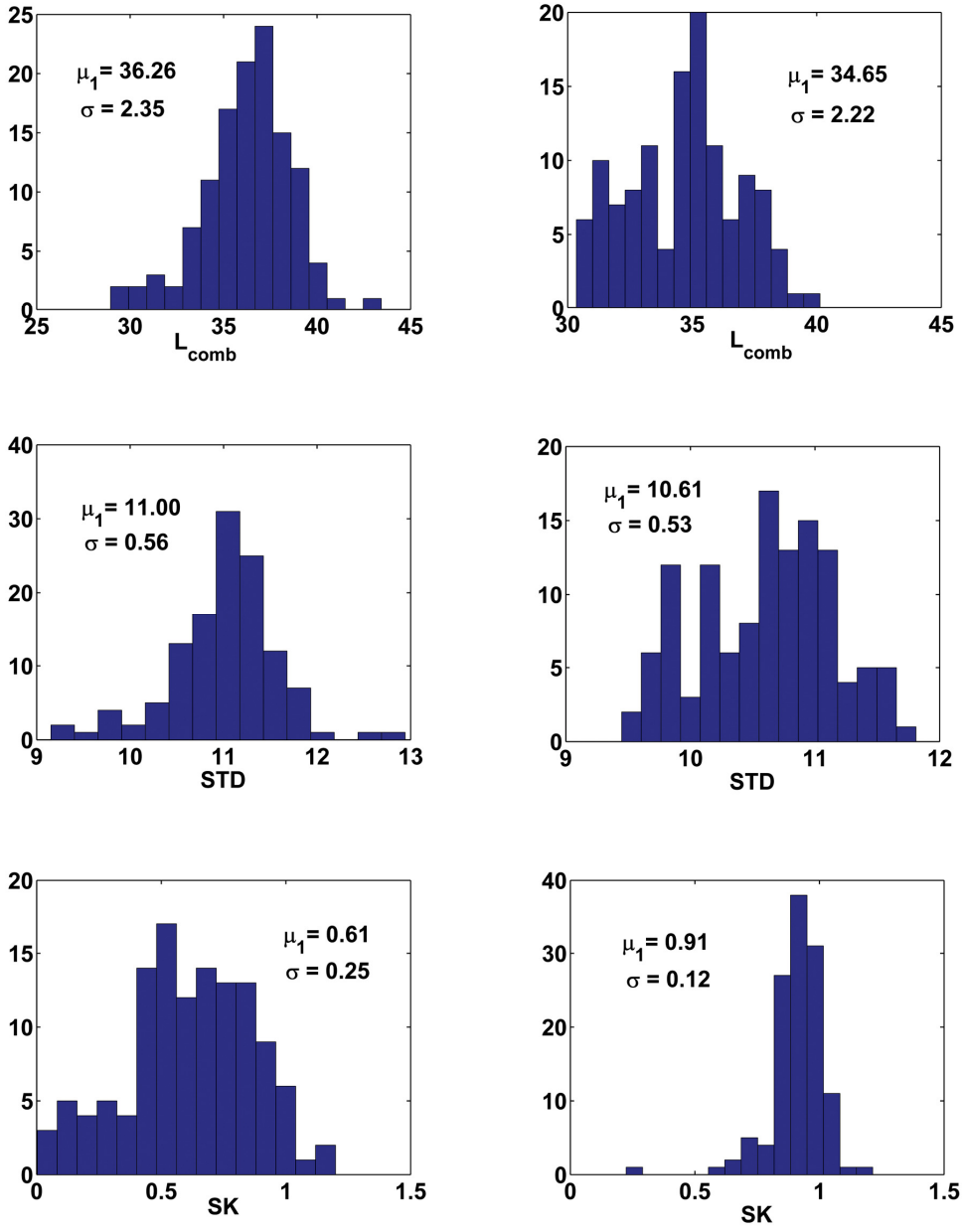

Figure 86. Case 3 histograms of $L_{comb,i}$ [cm], STD_i [cm], and SK_i [nodimensional]. Left column is subinterval 2 and right column in subinterval 3.

PART 4

REVIEW, CONCLUSIONS AND FUTURE WORK

CHAPTER 10 REVIEW AND CONCLUSIONS

The purpose of this thesis investigation was to demonstrate the feasibility of the PAT concept for aircraft afterburner combustion without flameholders. Specifically, the goal was to show that fuel injection upstream or within turbine stages together with a non-intrusive trigger mechanism near the afterburner inlet can establish compact, efficient and stable afterburner combustion without risk to the turbine stages. This goal was achieved using the AF and PAC experiments, Chemkin simulations, and a developed theoretical model.

The AF was used to demonstrate the feasibility of the PAT in an environment that simulated the temperature, velocity and O_2 content through a turbojet combustor, turbine stage and afterburner. First, it was used to demonstrate only the prime stage. Jet-A was injected into the bulk flow at various locations upstream of the TS with the intention of producing either no combustion at all or an autoignition combustion zone only downstream of the TS, in accordance with the PAT concept. Temperature, pressure and chemiluminescence measurements showed that Jet-A autoignition can occur within the AF at the operating range of the experiments. Injection close enough to the TS inlet resulted in autoignition only downstream of the TS, but injection too far upstream of the TS inlet resulted in autoignition upstream of the TS throat. The results of the AF prime stage experiments have the following implications for the prime stage in a turbine engine: (1) the ignition delay time of Jet-A injected within turbine stages is short enough to produce spontaneous combustion in the afterburner, but also short enough to pose a risk

to the turbine blades; (2) at a given operating point, there exists a range of injection locations within the turbine stages that results in safe and repeatable autoignition in the afterburner only; and (3) the Jet-A autoignition process creates a primed mixture at the afterburner inlet (i.e., a premixed, partially reacted mixture containing intermediate hydrocarbon species and radicals) that should be easier to ignite and control than an unreacted, non-premixed Jet-A mixture. Next, the AF was used to demonstrate the use of both the prime and trigger stages together. A H_2 injector was installed just downstream of the TS outlet to trigger the primed mixture combustion process. Experiments were conducted at various AF bulk flow operating conditions, Jet-A equivalence ratios, and H_2 flow rates. The results showed that the H_2 trigger can anchor the combustion zone, thus decreasing sensitivity to changing operating conditions. In addition, the H_2 trigger reduced the combustion zone length, reduced the fluctuations of the combustion zone length and position, and increased the AF combustion efficiency. Thus, the H_2 trigger performed all the desired effects of a trigger mechanism.

While the AF experiments demonstrated the feasibility of the PAT concept, more specific aspects of the concept were further explored with the developed theoretical model, the Chemkin simulations and the PAC experiments. The developed model was used to complement the prime stage investigation, while the Chemkin simulations and PAC experiments complemented the trigger stage investigation.

The purpose of the developed model was to help predict and interpret results obtained in the AF prime stage experiments. The model predicted the AF autoignition combustion zone location by simulating Jet-A evaporation, mixing and chemical reactions as a function of the injection location, spray characteristics (SMD), and AF

operating conditions. Its predictions were in reasonable agreement with the experimental results, especially in terms of the measured changes in the combustion zone location. The model predictions were also used to create the injection/ignition maps, which showed the predicted dependence of the autoignition location upon the injection location. The maps revealed the presence of an injection range upstream of the TS that produces a primed mixture at the TS outlet and an autoignition combustion zone at a relatively fixed location downstream of the TS, as desired for the PAT afterburner. The significance of this predicted injection range, termed Region III, is that it should also exist within the turbine stages of a turbojet engine, since the developed model simulates fuel priming in the AF and the AF, in turn, simulates a turbojet engine.

The developed model was also used to assess the prime stage feasibility at higher turbine engine bulk flow pressures, which were not achievable with the AF because of cost and time constraints. This effort considered the effects of both the high pressure magnitude and the rapid pressure drop across a turbine stage. For the most part, the model predicted that higher bulk flow pressure predominantly affects autoignition by reducing the chemical ignition delay time. The generated high pressure injection/ignition maps still contained a range of injection locations upstream of the TS that produces autoignition only downstream of the TS; i.e., Region III still appeared on the maps. Thus, the model predicted that fuel priming and autoignition without risk to the turbine blades is still feasible at higher operating pressures. The model also revealed that the large, rapid pressure drop across a turbine stage can produce fuel droplet flash-boiling, which could have a positive or negative effect on the PAT concept. If necessary, flash-boiling could be used to decrease an evaporation time that is otherwise too long for sufficient fuel

priming through the turbine stages. On the other hand, it has to be avoided if it decreases the ignition delay time to a point where significant heat release occurs within the turbine stages. The potential for flash-boiling depends on the magnitude of the pressure and pressure gradient, the injection location, the droplet size, and the droplet temperature history. Therefore, its effect needs to be assessed on a case-by-case basis. The injection/ignition maps can be used to identify injection locations that potentially lead to flash-boiling, which would appear in a new injection region on the map characterized by sharp upstream shifts of the reaction percent lines.

As stated above, the developed model was used to study the prime stage physics and to predict performance at operating conditions not achievable in the AF. Similarly, the Chemkin simulations were used to study the trigger stage chemistry and to analyze the POx gas trigger performance, which was not possible in the AF experiments. Specifically, the Chemkin simulations evaluated H_2 and POx trigger gas effects on Jet-A/vitiated-air autoignition using a closed homogeneous batch reactor model. The simulations were conducted for varying trigger gas amounts (PR_G or PR_{G,H_2}), Jet-A/vitiated-air equivalence ratios ($\phi_{surr.fuel}$) and vitiated-air compositions. The results showed that both the H_2 and the POx gas triggers can reduce the Jet-A/vitiated-air ignition delay time (t_{ign}). The H_2 trigger produced the greatest t_{ign} reduction, as expected; however, the POx triggers could be nearly as effective. For example, the $POx_{(3.325)}$ trigger produced almost the same scaled t_{ign} reduction ($[\Delta t]^*_{n.t.}$ reduction) as the H_2 trigger for equal PR_{G,H_2} values. To summarize, the results showed that $[\Delta t]^*_{n.t.}$ decreased with an increase in trigger gas PR_G, a decrease in $\phi_{surr.fuel}$ (at constant PR_G), and a decrease in

vitiated-air O_2 content (at constant PR_G). Notably, the results showed that increasing the trigger gas PR_G has a diminishing effect, producing only small $[\Delta t]^*_{n.t.}$ decreases near the maximum PR_G values (i.e., near stoichiometric combustion, $\phi_G \approx 1$).

The Chemkin results indicated that the trigger gas composition must be carefully selected. Besides a single $POx_{(1.45)}$ exception, the H_2 and POx gas triggers always decreased t_{ign}, whereas the Jet-A surrogate-fuel trigger always increased t_{ign}. Chemkin studies were conducted to explore why the H_2 and POx gas triggers are able to reduce t_{ign}. The properties thought to influence the effect of the trigger gas were: (1) the trigger-gas/vitiated-air ignition delay time, expressed as $t^*_{\Delta t,n.t.}$; (2) the adiabatic temperature of complete trigger-gas/Jet-A/vitiated-air combustion, expressed as $[\Delta T]^*_{n.t.,final}$; and (3) the rapid production of radicals from the H_2 component of the trigger gas. The Chemkin results indicated that the t_{ign} reduction strongly correlates with both $t^*_{\Delta t,n.t.}$ and $[\Delta T]^*_{n.t.,final}$. In fact, the results suggested that a trigger gas can reduce t_{ign} only if $t^*_{\Delta t,n.t.} < 1$ and $[\Delta T]^*_{n.t.,final} > 1$, which essentially places lower limits on the trigger gas reaction rate and energy density relative to Jet-A. These two conditions were consistent with all the data, including the surrogate-fuel trigger and the $POx_{(1.45)}$ exception. Since a single metric for quantifying the effect of radical was not defined, radical production was not included in the above criterion. However, radical production is likely one of the fundamental reasons for the effectiveness of the H_2 and POx gas triggers. The Chemkin simulations showed that when H_2 is added to the high temperature primed mixture it dissociates almost immediately to produce such radicals as H, OH, HO_2, and H_2O_2. These radicals

participate in chain-branching and chain-propagating reactions with the surrounding hydrocarbon species, thereby initiating or accelerating the hydrocarbon autoignition process.

The trigger stage investigation was also complemented by the PAC experiments. The original purpose of the PAC experiments was to address three major issues regarding the AF experimental results. The first was the accuracy of the combustion efficiency estimates that were only based upon O_2 sensor data. The PAC experiments showed that an O_2 sensor alone does not accurately estimate combustion efficiency. Thus, future AF experiments should also include a CO_2 sensor. The PAC results also showed that zero chemiluminescence intensity at the sampling tube inlet correlates with complete combustion. This was used to double-check the AF O_2 sensor measurements; if the O_2 sensor indicated complete combustion but the measured intensity was not zero at the sampling tube inlet, then there were likely still significant amounts of CO and unburned hydrocarbons in the gas sample. The second issue with the AF measurements was the contribution of background radiation to the measured intensity, which was a concern because it could potentially alter the values and trends of the computed combustion zone characteristics. The PAC spectrometer measurements showed that background radiation can be as high as ~60% of the measured intensity in the 430+/-5nm range. However, the ratio of CH* chemiluminescence to background radiation intensity was nearly constant along the test section length or increased linearly with a shallow slope (excluding data at the beginning and end of combustion zone, where intensity was very low). Since the intensity profiles are normalized before computing the combustion zone characteristics, the nearly constant background radiation fraction had only a small effect on the resulting

values and trends. Finally, the third issue with the AF measurements concerned the accuracy of the axial intensity polynomial curve fits. The PAC test section allowed measurements of continuous axial intensity profiles, unlike the segmented AF intensity profiles. Thus, the PAC experiments demonstrated the use of the combustion zone characteristics for quantifying the effects of the trigger without the introduced errors due to profile fits. The resulting familiarity with both the qualitative continuous intensity profile shapes and the quantitative combustion zone characteristics values helped define the AF polynomial profile fit procedure and check the AF combustion zone analysis results.

Besides helping interpret the AF results, the PAC experiments also contributed new information to the PAT feasibility investigation. First, the PAC demonstrated a simplified prime and trigger process (no evaporation, bulk flow temperature drop, or bulk flow acceleration from duct area change) at higher primary combustion ϕ and higher hydrocarbon/vitiated-air ϕ than could be achieved in the AF. At these conditions, the results showed that the H_2 trigger can still shift the combustion zone upstream and make it more compact. Moreover, the results near maximum PR_G confirmed the Chemkin predictions that increases in trigger gas flow eventually have diminishing effects on the hydrocarbon combustion process. Another contribution of the PAC experiments came from the OH* chemiluminescence measurements. These were used to distinguish the H_2 trigger gas combustion process from the hydrocarbon combustion process. The OH* chemiluminescence measurements showed that H_2 was consumed well before the end of the propane combustion zone, thus indicating that the H_2 trigger mostly influenced the onset of the propane combustion process. This explains why the H_2 trigger affected the

characteristics associated with the first half of the combustion zone (e.g., $X_{5\%}$ and X_{MAX}) more strongly than those associated with the latter half (e.g., $X_{95\%}$ and L_{comb}) in both the PAC and AF experiments.

Finally, it should be noted that the tools used in this investigation– the AF, the developed theoretical model, the Chemkin simulations and the PAC – provide a well-rounded process for investigating the PAT afterburner concept. The original intent was to study the PAT concept only with the AF; however, the AF was very costly and time consuming to operate and it also could not provide sufficient details about the physics of the prime and trigger process. Therefore, the theoretical model, the Chemkin simulations and the PAC were developed during the course of this investigation to provide more detailed knowledge and simplified experimental data. Now that those resources are available, they can be used in conjunction with the AF to investigate the PAT afterburner through the following recommended process:

1. Use *Chemkin to predict* the performance of candidate trigger gases.
2. Use the *PAC to test* and compare the candidate trigger gases.
3. Use the *developed model to predict* the location and trends of the autoignition combustion zone at the desired AF operating conditions and Jet-A injection locations.
4. Use the *AF experiments to test* the PAT afterburner feasibility with the above bulk flow operating points, Jet-A injection locations, and trigger gas.
5. Use the *AF results to improve* the model, thus increasing its accuracy for the next iteration.

CHAPTER 11 FUTURE WORK

This chapter describes four suggested research topics for further development of the PAT afterburner concept. The suggested topics are illustrated in Figure 87 through Figure 89.

The first suggested investigation concerns the Jet-A injector design coupled with a study of multi-phase flow through the turbine stages - corresponding to (1) in Figure 87. The airblast atomizer used in the AF would not be appropriate for fuel injection within turbine stages. Airblast atomizers would require a longer gap between turbine stages and would produce wakes that increase aerodynamic losses and reduce work extraction. Perhaps a better approach would be non-intrusive fuel injection through channels in the stator vanes. Whatever the choice, the appropriate fuel injection system must optimize fuel atomization, penetration and mixing, as well as production issues such as machinability, durability and cost. Of course, the injector must also facilitate fuel priming; i.e., result in sufficient evaporation, mixing and chemical reactions within the turbine stages without significant heat release. Thus, a detailed model of the multi-phase

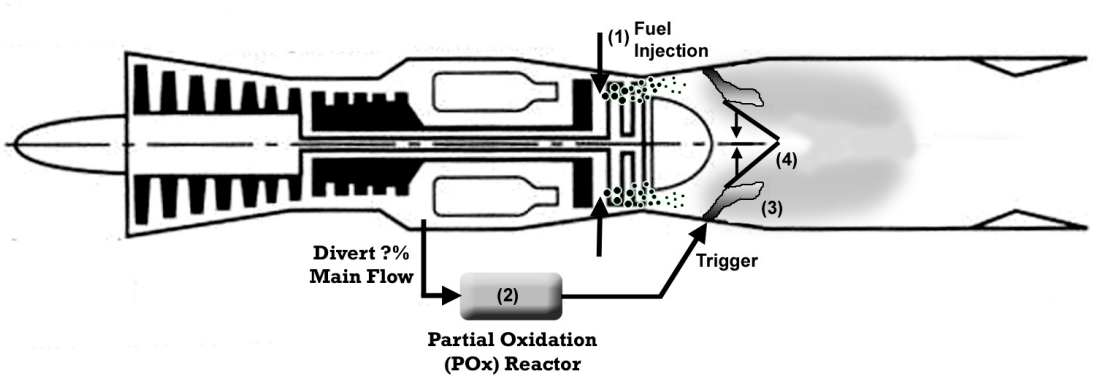

Figure 87. Locations of interest for future work: (1) method for fuel injection and study of multi-phase flow through the turbine stages; (2) the development of the POx reactor; (3) the trigger gas jet placement and penetration; (4) combustion zone spreading rate.

flow through the turbine stages should accompany the fuel injector design effort. The multi-phase flow model could consist of the droplet vaporization and convection model developed in this investigation with the following suggested updates: droplet diameter distribution, supercritical phase models, multi-component evaporation, and droplet break-up due to shear. Even with these improvements, the model would still function as a simple design tool. An experimental setup could be constructed to test the fuel injection methods and to calibrate the multi-phase flow model. For example, a potential experimental setup could consist of turbine stage cascades between quartz walls. Fuel injectors could be imbedded within the cascade vanes, and seeding and laser diagnostics could be used for flow and droplet visualization. Note that it would be important to test for flash-boiling. Thus, the facility should simulate the turbine engine pressure drop. The cost and complexity of this suggested high pressure and high temperature facility could be greatly reduced by replacing Jet-A with a higher volatility liquid. In this way, the bulk flow temperature could be scaled down to a point where wall cooling is not necessary. The measurements of spray characteristics, droplet evaporation, flash-boiling, and mixing could be used to calibrate the multi-phase flow model. Then, the anchored model could predict the injection system performance in a turbine engine by inputting Jet-A thermophysical properties and a realistic turbine stage bulk flow profile.

The next suggested topic for future investigation is the development of the POx reactor - corresponding to (2) in Figure 87. This thesis introduced the use of POx gas as a trigger for afterburner combustion, and the Chemkin simulations predicted that POx gas would be an effective trigger. Thus, the next step is to design a compact, lightweight POx reactor. The resulting POx gas could then be injected into the PAC or AF to demonstrate

its effect on hydrocarbon/vitiated-air autoignition. Figure 87 shows the envisioned placement of the POx reactor in a PAT turbojet engine. The inlet air is drawn from the compressor outlet. The advantage of using the compressor outlet air is that the elevated pressure and temperature accelerate the relatively slow partial oxidation reaction mechanism[9]. In addition, the high pressure air would facilitate flow control using simple metering orifices and would produce high velocity trigger gas jets for sufficient penetration into the afterburner core flow.

Another suggested topic is the study of the trigger gas jet placement, penetration and mixing - corresponding to (3) in Figure 87. The diameter of an afterburner duct relative to the envisioned trigger gas jet diameter is much larger than in the AF or PAC. Thus, multiple circumferentially-spaced trigger gas jets would likely be necessary in a PAT afterburner. Finite mixing rates and the distinction between PR_G and PR_L would be particularly relevant because of the large cross-sectional area. In fact, there would likely be large portions of the afterburner bulk flow that never directly interact with the trigger gas ($PR_L = 0$). Thus, a concurrent flame spreading study - corresponding to (4) in Figure 87 - would be needed to optimize the trigger jet configuration. Interestingly, the flame near the trigger gas jet would spread through a medium that is already reacting and potentially very close to complete autoignition. Thus, flame spreading would be coupled with the autoignition process. The trigger jet placement and flame spreading through a primed mixture could be studied using a small facility with the same layout as the PAC (primary combustor, propane injector, and quartz test section). However, the test section of this facility would have a rectangular cross-section with a high aspect ratio. Fuel

[9] As indicated by Chemkin perfectly stirred reactor simulations (results not shown).

would be injected into the vitiated-air through the short wall of the rectangular duct. In this way, the width (long-edge) of the duct relative to the trigger gas jet diameter would simulate the large afterburner duct radius.

The final suggested topic is a PAT turbofan feasibility investigation. Figure 88 shows a tentative schematic of a PAT turbofan and afterburner. In this configuration, only a small fraction of the fuel is injected into the turbine stages; the remaining fuel is injected into the bypass air. The primed fuel exiting the turbine stages would be triggered prior to mixing with the bypass-air. In this way, the heat release from the core flow autoignition process could ignite the bypass fuel/air mixture. If necessary, additional trigger gas jets downstream of the bypass-air inlet to the afterburner could be used to shorten and stabilize the bypass mixture combustion process. The AF with the modifications shown in Figure 89 could be used for the PAT turbofan feasibility investigation. A 'bypass-air' inlet could be cut into a diverging section sidewall, and Jet-A could be injected into the bypass-air just prior to mixing with the reacting 'core' flow. A second trigger could be installed just downstream of the bypass-air inlet to the AF, although it may not be needed. Note that flame arresters, such as an array of air-cooled fins, may be needed to prevent flashback into the bypass-air line. Also, a straight duct

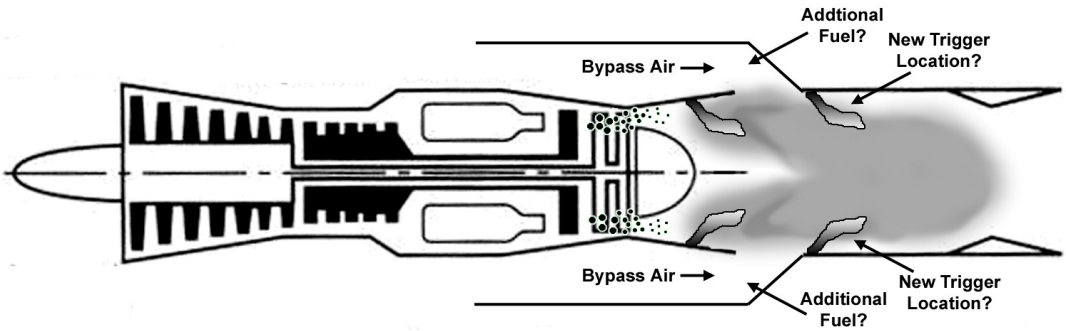

Figure 88. Schematic of PAT concept for turbofan afterburner showing some initial design considerations

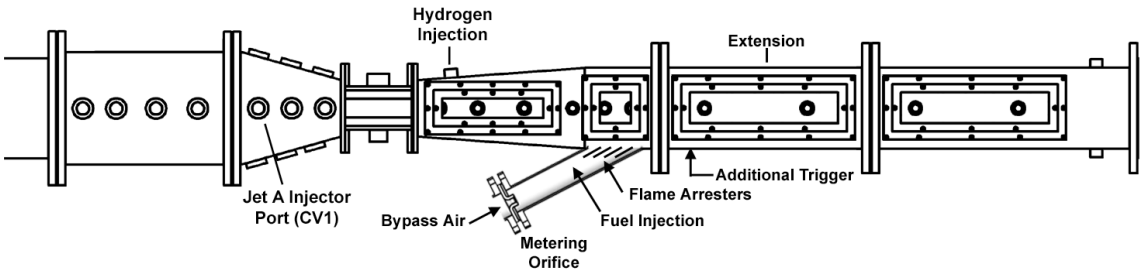

Figure 89. Proposed AF modifications for a PAT turbofan feasibility investigation: bypass-air supply with metering orifice, bypass Jet-A injection system, air-cooled flame arresters, straight duct extension, and an additional trigger.

extension with a quartz window would likely be necessary to accommodate a longer combustion zone.

APPENDIX A

FUEL AND MIXTURE THERMOPHYSICAL PROPERTIES

Table A-1 and Table A-2 list the liquid and gaseous fuel thermophysical properties used for the evaporation sub-model described in Section 4.1. The fuel vapor/vitiated-air mixture properties were computed using the properties in Table A-2 and the average temperature and fuel mole fraction defined in Equation (4.4) and Equation (4.5). First, the average fuel mole fraction, χ_F, was used to compute the vitiated-air mole fraction, equal to $1-\chi_F$. The vitiated-air mole fraction was then decomposed to O_2, N_2, H_2O and CO_2 mole fractions, the proportions of which are known from analysis of equilibrium combustion at the given methane/air ϕ used to generate the vitiated-air. Next, the species mole fractions are converted to mass fractions using molecular weights, where the molecular weight of Jet-A is approximated as $172.4\frac{g}{mol}$

Table A-1. Liquid fuel thermophysical properties and properties related to vaporization. T is temperature in Kelvin. Properties from [9] are curve-fits from tabulated data.

Property	Units	Fuel	Expression	Source
Specific Heat	$\frac{J}{kg\cdot K}$	Kerosene	$c_{liq}=1000*(0.0050872*(T-273)+1.877)$	[9]
Viscosity	$Pa\cdot s$	Kerosene	$\mu_{liq}=-6.0702e\text{-}15*T^5 + 1.405e\text{-}11*T^4 \ldots$ $-1.2944e\text{-}8*T^3 + 5.943e\text{-}6*T^2 \ldots$ $-1.3641e\text{-}3*T + 0.12612$	[9]
Surface Tension	$\frac{N}{m}$	Kerosene	$\sigma_{liq}=7.3894e-8*T^2-1.3992e-4*T \ldots$ $+ 0.061509$	[9]
Heat of Vaporization	$\frac{J}{kg}$	n-Decane	$\Delta h_{vap}=4184*9.453*(619\text{-}T)^{0.38}$	[7]
Vapor Pressure	Pa	n-Decane	$P_{vap}=101325*\exp(11.495-5141.36/T)$	[7, 11]

($C_{12.5}H_{22.4}$). Finally, the Jet-A/vitiated-air mixture properties are computed using the mass fractions, the thermophysical properties of O_2, N_2, H_2O and CO_2 given in [10], and the fuel vapor properties in Table A-2. For example, the mixture specific heat is calculated as follows:

$$c_{p,mix} = \sum Y_i \cdot c_{p,i} \tag{9.3}$$

where the subscript 'i' denotes each species in the mixture; Y_i is the species mass fraction; and $c_{p,i}$ is the species specific heat in $^{J}/_{kg-K}$. Note that each $c_{p,i}$ is computed at the average temperature. The mixture viscosity and thermal conductivity are calculated using the semiempirical formula of Wilke [30].

Table A-2. Fuel vapor thermophysical properties. T is temperature in Kelvin and P is pressure in Pascals. Properties from [9] are curve-fits from tabulated data.

Property	Units	Fuel	Expression	Source
Specific Heat	$\frac{J}{kg \cdot K}$	n-Decane	$T \le 700K$: $c_{p,vap} = 2.407e2 + 5.0996*T - 6.2902e-4*T^2 \ldots$ $-1.07e-6*T^3$ $T > 700K$: $c_{p,vap} = -1.3534e4 + 9.14879*T - 2.207e-1*T^2 \ldots$ $+2.91406e-4*T^3 - 2.15307e-7*T^4 \ldots$ $+8.386e-11*T^5 - 1.344e-14*T^6$	[10]
Thermal Conductivity	$\frac{W}{m \cdot K}$	Kerosene	$k_{vap} = (1.3783*(T-273)+1.5333)*10^{-4}$	[9]
Viscosity (1 bar)	$Pa \cdot s$	Kerosene	$\mu_{vap} = 3.6479e-8*T - 6.9157e-6$	[9]
Molecular Diffusivity	$\frac{m^2}{s}$	Decane /Air	$D_M = 5.46e-6*(T/300)^{1.583}*(101325/P)$	[7]

APPENDIX B

REFERENCE FOR CHEMKIN ANALYSIS

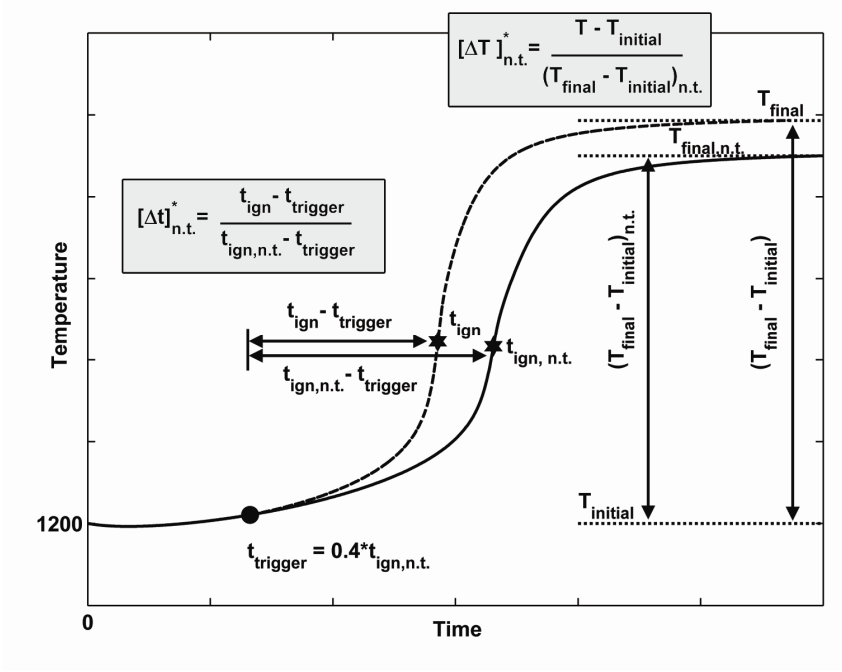

Figure B-1. Reference for the Chemkin analysis scaled parameters. The solid line is a case with no trigger and the dashed line is a case with a trigger.

Table B-1 Jet-A Surrogate-fuel/Trigger-Gas/Vitiated-air$_{(0.4)}$

Trigger Type	$\phi_{surr.fuel}$	PR_G	PR_{G,H_2}	t_{ign}, msec	T_{final}, K
None	0.15	x	x	1.72	1387
	0.35	x	x	1.66	1650
	0.75	x	x	1.78	2096
H_2	0.35	0.10	0.10	1.428	1693
		0.25	0.25	1.222	1760
		0.50	0.50	1.041	1860
		1.0	1.0	0.89	2041
		2.19	2.19	0.80	2340
	0.75	0.1	0.1	1.62	2158
		0.25	0.25	1.43	2241
		0.39	0.39	1.32	2295
$POx_{(3.325)}$	0.35	0.172	0.10	1.46	1716
		0.43	0.25	1.28	1811
		0.86	0.50	1.11	1952
		2.56	1.49	0.93	2257
	0.75	0.086	0.05	1.73	2138
		0.172	0.10	1.68	2179
		0.3	0.175	1.61	2228
		0.46	0.27	1.54	2264

Table B-1 continued

Trigger Type	$\phi_{surr.fuel}$	PR_G	PR_{G,H_2}	t_{ign}, msec	T_{final}, K
$POx_{(1.45)}$	0.35	0.23	0.10	1.48	1703
		0.57	0.25	1.32	1761
		1.625	0.71	1.12	1886
	0.75	0.065	0.029	1.82	2095
		0.16	0.07	1.84	2097
		0.29	0.127	1.87	2095
Surrogate Fuel	0.35	0.25	x	1.72	1759
		1	x	1.9	2044
		1.85	x	2.07	2260
	0.75	0.1	x	1.84	2156
		0.2	x	1.88	2210
		0.33	x	1.93	2262

Table B-2 Jet-A Surrogate-fuel/Trigger-Gas/Vitiated-air$_{(0.75)}$

Trigger Type	$\phi_{surr.fuel}$	PR_G	PR_{G,H_2}	t_{ign}, msec	T_{final}, K
None	0.15	x	x	3.03	1279
	0.35	x	x	3.74	1383
	0.75	x	x	5.43	1584
H_2	0.35	0.1	0.1	3.16	1401
		0.25	0.25	2.67	1427
		0.5	0.5	2.29	1473
		1	1	2.0	1559
		2.19	2.19	1.82	1735
	0.75	0.05	0.05	5.05	1597
		0.2	0.2	4.28	1648
		0.39	0.39	3.74	1698
$POx_{(3.325)}$	0.35	0.172	0.10	3.22	1412
		0.43	0.25	2.80	1457
		0.86	0.50	2.45	1525
		1.72	1.00	2.19	1649
		2.56	1.49	2.09	1718
	0.75	0.086	0.05	5.13	1607
		0.172	0.10	4.88	1634
		0.22	0.128	4.77	1648
		0.46	0.268	4.33	1699
$POx_{(1.45)}$	0.35	0.23	0.10	3.16	1415
		0.575	0.25	2.71	1462
		1.625	0.71	2.24	1569
	0.75	0.16	0.07	5.06	1613
		0.29	0.127	4.83	1636

Table B-3 Trigger gas/Vitiated-air Autoignition. Vitiated-air$_{(0.4)}$ with trigger gas added at the PR_G value relative to $\phi_{surr.fuel}$.

Trigger Type	$\phi_{surr.fuel}$	PR_G	t_{ign} , msec
H_2	0.75	0.1	0.843
		0.25	0.777
		0.39	0.758
$POx_{(3.325)}$	0.75	0.086	0.927
		0.172	0.852
		0.3	0.805
		0.46	0.787
$POx_{(1.45)}$	0.75	0.065	1.03
		0.16	0.890
		0.29	0.843

REFERENCES

[1] Lovett, J. A., Brogan, T. P., and Philippona, D. S, "Development Needs for Advanced Afterburner Designs," Proc. 40th Joint Propulsion Conference and Exhibit, Fort Lauderdale, FL, 2004, AIAA-2004-4192.

[2] Rabovitser, J., Nester, S., and Wohaldo, S., "Development of a Partial Oxidation Gas Turbine (POGT) for Innovative Gas Turbine Systems, Proceedings of the ASME Turbo Expo, Montréal, Canada, May 2007.

[3] Castaldi, M. et al., "Performance of Microlith Based Catalytic Reactors for an Isooctane Reforming System," SAE Technical Paper, No. 2003-01-1366, (2003c).

[4] Tong, G. C. M., Flynn, J., and Leclerc, C. A., "A Dual Catalyst Bed for the Autothermal Partial Oxidation of Methane to Synthesis Gas," Catalysis Letters, Vol. 102(3-4), Aug. 2005, pp 131-137.

[5] Eng, J. A., Leppard, W. R., and Sloane, T. M., "The Effect of POx on the Autoignition Chemistry of n-Heptane and Isooctane in an HCCI engine," SAE Technical Paper, No. 2002-01-2861, (2000c).

[6] Yang, W. and Kee, R., "The Effect of Monodispersed Water Mists on the Structure, Burning Velocity, and Extinction Behavior of Freely Propagating, Stoichiometric, Premixed, Methane-Air Flames," Combustion and Flame, Vol. 130(4), 2002, pp. 322-335.

[7] Abramzon, B. and Sirignano, W. A., "Droplet Vaporization Model for Spray Combustion Calculations," Int. J. Heat Mass Transfer, Vol. 32(9), 1989, pp. 1605-1618.

[8] Jasuja, A. K, "Atomization of Crude and Residual Fuel Oils," Transactions of the ASME, Vol. 101, 1979, pp. 250-258.

[9] Vargaftik, N., Vinogradov, Y., and Yargin, V., *Handbook of Physical Properties of Liquids and Gases*, 3rd ed., Begell House, New York, 1996.

[10] Turns, S. R, *An Introduction to Combustion*, 2nd ed., McGraw Hill, Boston, 1996.

[11] Reid, R. C., Prausnitz, J. M., and Poling, B. E., *The Properties of Gases and Liquids*, 4th ed., McGraw Hill, New York, 1987.

[12] Gokalp, I., Chauveau, C., Simon, O., and Chesneau, X., "Mass Transfer from Liquid Fuel Droplets in Turbulent Flow," Combustion and Flame, Vol. 89(3-4), 1992, pp. 286-298.

[13] Ducourneau, F, "Inflammation Spontanée de Mélanges Riches Air-Kérosène," Entropie, Vol. 59, 1969.

[14] Freeman, G. and Lefebvre, A. H., "Spontaneous Ignition Characteristics of Gaseous Hydrocarbon-Air Mixtures," Combustion and Flame, Vol. 58, 1984, pp. 153-162.

[15] Lefebvre, A., Freeman, W., and Cowell, L., "Spontaneous Ignition Characteristics of Hydrocarbon Fuel/Air Mixtures," NASA Technical Report 175064, 1986.

[16] Mullins, B. P., "Studies on the Spontaneous Ignition of Fuels Injected into a Hot Air Stream," Journal of the Institute of Petroleum, January, Vol. 33, 1947, pp. 211-253, 327-342.

[17] Mullins, B. P., "Combustion in Vitiated Atmospheres – parts I, II, III, and IV," Fuel, Vol. 28, 1949.

[18] Mullins, B. P., "Studies on the Spontaneous Ignition of Fuels Injected into a Hot Air Stream V – Ignition Delay Measurements on Hydrocarbons," Fuel, Vol. 32, 1953, pp. 363-379.

[19] Spadaccini, L. J. and Tevelde, J. A., "Autoignition Characteristics of Aircraft Type Fuels," NASA Technical Report 159886, 1980.

[20] Livengood, C. J. and Wu, C.P., "Correlation of Autoignition Phenomena in Internal Combustion Engines and Rapid Compression Machines," Fifth International Symposium on Combustion, University of Pittsburgh, Pittsburgh, Pennsylvania, 1955, pp. 347-356.

[21] Assanis, D. N., Filipi, Z. S., Fiveland, S. B., and Syrimis, M., "A Predictive Ignition Delay Correlation under Steady-State and Transient Operation of a Direct Injection Diesel Engine," Transactions of the ASME, Vol. 125, 2003, pp. 450-457.

[22] Colin, O., Pires da Cruz, A., and Jay, S., "Detailed Chemistry-based Auto-ignition Model Including Low Temperature Phenomena Applied to 3-D engine Calculations," Proc. Combustion Institute, Vol. 30, 2005, pp. 2649-2656.

[23] D. Kawano, H. Ishii, H. Suzuki, Y, Goto, M. Odaka and J. Senda, "Numerical Study on Flash-Boiling Spray of Multicomponent Fuel," Heat Transfer –Asian Research, Vol. 35(5), 2006, pp. 369-384.

[24] Vasu, S.S, Davidson, D. F., and R. K. Hanson, "Jet Fuel Ignition Delay Times: Shock Tube Experiments over Wide Conditions and Surrogate Model Predictions," Combustion and Flame, Vol. 152, 2008, pp. 125-143.

[25] A. Violi, et al., "Experimental Formulation and Kinetic Model for JP-8 Surrogate Mixtures," Combustion Science and Technology," Vol. 174 (11-12), 2002, 399-417.

[26] E. Ranzi, 2006, available at http://www.chem.polimi.it/CRECKModeling/kinetic.html, [Accessed: May 2008].

[27] Westbrook, C., "Chemical Kinetics of Hydrocarbon Ignition in Practical Combustion Systems," Proceedings of the Combustion Institute, Vol. 28, 2000.

[28] Zheng, J., Yang, W., Miller, D., L., and Cernansky, N., P., "A Skeletal Chemical Kinetic Model for the HCCI Combustion Process," SAE Technical Paper, No. 2002-01-0423, 2002.

[29] Nori, V. N., and Seitzman, J., "Chemiluminescence Measurements and Modeling in Syngas, Methane and Jet-A Fueled Combustors," 45th AIAA Meeting and Exhibit, Reno, Nevada, Jan. 2007.

[30] White, F. M., *Viscous Fluid Flow*, 2nd ed., McGraw Hill, 1991, p.34.